Graphene-based devices for terahertz and beyond

Original Citation:
Graphene-based devices for terahertz and beyond / Ullah, S.. - ELETTRONICO. - (2026).

Published version
DOI:

Publisher: Politecnico di Bari

Department of Electrical and Information Engineering
ELECTRICAL AND INFORMATION ENGINEERING
Ph.D. Program
SSD: ING-INF/02 – ELECTROMAGNETIC FIELDS

Final Dissertation

Graphene-Based Devices for Terhertz and Beyond

---

by
Sana Ullah

<u>Supervisors:</u>

Prof. Antonella D'Orazio

Dr. Giovanni Magno

Dr. Ilaira Marasco

Coordinator of Ph.D. Program:
Prof. Nicola Giaquinto

Course n°38, 01/04/2023–31/03/2026

Politecnico
di Bari

Department of Electrical and Information Engineering
ELECTRICAL AND INFORMATION ENGINEERING
Ph.D. Program
SSD: ING-INF/02 – ELECTROMAGNETIC FIELDS

Final Dissertation

Graphene-Based Devices for Terhertz and Beyond

---

by
Sana Ullah
Sana Ullah

Referees:

Dr. Artem Voroven

Dr. Jesus Hernan Mendoza-Castro

Supervisors:

Prof. Antonella D’Orazio
Antonella D'Orazio

Dr. Giovanni Magno
Giovanni Magno

Dr. Ilaria Marasco
Ilaria Marasco

Coordinator of Ph.D Program:
Prof. Nicola Giaquinto
Nicola Giaquinto

Course n°38, 01/04/2023–31/03/2026

Abstract

Reconfigurable electromagnetic and optical devices are important for nonlinear optical and next-generation communication systems. This thesis analyzes graphene-based tunable structures for the control of radiation patterns in terahertz antennas and for enhanced nonlinear optical generation in hybrid nonlinear metasurfaces. Three different graphene-enabled platforms are explored: electrostatically programmable antennas, magnetically biased reconfigurable antennas, and graphene-lithium niobate nonlinear metasurfaces.

First, a transparent disc-shaped programmable antenna working at sub-terahertz frequencies is proposed. The antenna consists of two orthogonal dipoles integrated with eight fan-blade-shaped graphene parasitic elements on a polyimide substrate. By adjusting the chemical potential of graphene, the current distribution across the radiating structure is modified, enabling programmable beam steering. Single, dual, and quad-beam radiation patterns can be generated by the antenna with discrete beam steering across the full 360 degree azimuthal plane. The proposed design obtains a maximum gain of 2 dBi for single-beam configuration, while maintaining good impedance matching with a minimum reflection coefficient of -36.4 dB at 200 GHz and a -10 dB bandwidth ranging from 187 GHz to 214 GHz.

The second part of the thesis introduces a graphene-based dipole antenna whose radiation characteristics are reconfigured through magnetic biasing. Unlike conventional electrical tuning methods, this mechanism exploits the anisotropic conductivity induced in graphene by applying in-plane and out-of-plane magnetic fields. A set of graphene parasitic elements placed near the dipole arms enables beam steering through magnetic-field-controlled current redistribution without the need for direct electrical contacts. The antenna is designed on a SiO_2 substrate and optimized via parametric studies to enhance impedance matching, realized gain, and radiation efficiency. Fourteen magnetic bias configurations are analyzed, each producing a distinct radiation pattern. The results demonstrate improved realized gain and pattern reconfigurability at 260 GHz, indicating the potential of magnetically controlled graphene antennas for compact terahertz communications systems.

Finally, this thesis investigates nonlinear optical processes in a hybrid graphene-lithium niobate metasurface designed for simultaneous second- and third-harmonic generation. The metasurface consists of graphene-$LiNbO_3$ pillars arranged on a

SiO_2 substrate and exploits the strong second-order nonlinearity of lithium niobate together with the third-order nonlinear responses of graphene and SiO_2. Guided-mode resonances supported by the periodic structure are identified through numerical simulations and analytical effective-index modeling. The results show that both second-harmonic generation (SHG) and third-harmonic generation (THG) efficiencies are enhanced at resonance conditions, with simultaneous enhancement occurring near the crossing of TE_0 and TM_1 guided modes.

Overall, the results presented in this thesis demonstrate the versatility of graphene for enabling tunable electromagnetic and nonlinear optical devices. The proposed antenna designs provide effective radiation pattern reconfigurability in the sub-terahertz regime, while the hybrid metasurface enables multi-resonant nonlinear optical generation via geometrical control of guided-mode resonances.

List of Publications

Journal Articles

1. **S. Ullah**, I. Marasco, A. D'Orazio, G. Magno, "Dual-Harmonic Generation in a Hybrid Graphene-Lithium Niobate Nonlinear Metasurface," *Optics Express*, Vol. 34, No. 11, May 2026, doi: 10.1364/OE.596715.
2. **S. Ullah**, I. Marasco, A. D'Orazio, G. Magno, "Graphene-based programmable dual dipole antenna with parasitic elements," *Optical and Quantum Electronics*, Vol. 57, No. 2, February 2025. doi: 10.1007/s11082-025-08050-1

Conference Papers

1. **S. Ullah**, I. Marasco, A. D'Orazio, G. Magno, "Transparent Reconfigurable Dipole Antenna for Sub-THz Beam Steering based on Graphene Twin Parasitic Sectors," *European Wireless 2024*, Brno, Czech Republic, pp. 169-174, 2024.
2. **S. Ullah**, I. Marasco, A. D'Orazio, G. Magno, "Transparent antenna with reconfigurable pattern based on programmable graphene parasitic elements," *2024 24th International Conference on Transparent Optical Networks (ICTON)*, pp. 10-14, July 2024.

DECLARATION

This thesis is entirely the candidate's own work, except where otherwise accredited. This thesis has not been submitted for an award in any other institution.

Author's signature: Sana Ullah

Sana Ullah

Supervisor's signature: Antonella D'Orazio

Prof. Antonella D'Orazio

Date:

2 July 2026

Acknowlegment

I would like to express my gratitude to Professor Antonella D'Orazio for her guidance and continuous support throughout my doctoral program. Her mentorship, encouragement, and commitment to fostering academic growth have been fundamental to the development of my research skills and professional maturity. I am deeply thankful for her trust and for the example of excellence she has consistently set.

I would also like to extend my heartfelt thanks to Dr. Giovanni Magno, whose support has been truly exceptional throughout this journey. His guidance in electromagnetic simulations, particularly in CST Studio Suite and COMSOL Multiphysics, was instrumental in shaping the core of this work. Beyond technical assistance, Dr. Magno provided constant encouragement, insightful feedback, and dedicated many hours to reviewing manuscripts and refining results. His deep involvement and unwavering support have left a profound mark on the quality and completion of this thesis. I am sincerely grateful for his mentorship and collaboration.

I also wish to thank Professor Marco Ornigotti from Tampere University for his supervision, valuable insights, and the opportunity to collaborate during my abroad period. His expertise and guidance have greatly enriched this work.

I also wish to thank Dr. Ilaria Marasco for her kind assistance and valuable contributions during different phases of this research. Finally, I am thankful to all my colleagues at the Nanophotonic and Electromagnetic Research Group for their friendship. Sharing both challenging and rewarding moments with them made my time in the laboratory a truly enriching experience.

Contents

List of Abbreviations

Abbreviation	**Full Form**
H	Horizontal Dipole
V	Vertical Dipole
P1, P2, ..., P8	Parasitic Element 1 to 8
H37	Horizontal dipole active + parasitic elements 3 and 7 ON
V2468	Vertical dipole active + parasitic elements 2, 4, 6, 8 ON
$\mathbf{B} \parallel \mathbf{x}$	Magnetic field parallel to x-axis (in-plane)
$\mathbf{B} \perp \mathbf{z}$	Magnetic field perpendicular to plane (out-of-plane)
μ_c	Chemical Potential (Fermi level)
τ	Relaxation Time
Γ	Scattering Rate ($\Gamma = \tau^{-1}$)
σ	Surface Conductivity
$\sigma_{\mathbf{intra}}$	Intraband Conductivity
$\sigma_{\mathbf{inter}}$	Interband Conductivity
E_F	Fermi Level
v_F	Fermi Velocity ($\approx 10^6$ m/s)
SPP	Surface Plasmon Polariton
CST	CST Studio Suite
COMSOL	COMSOL Multiphysics
FEM	Finite Element Method
PML	Perfectly Matched Layer
PEC	Perfect Electric Conductor
S_{11}	Reflection Coefficient
VBA	Visual Basic for Applications
SHG	Second-Harmonic Generation
THG	Third-Harmonic Generation
SFG	Sum-Frequency Generation
DFG	Difference-Frequency Generation
FWM	Four-Wave Mixing
GMR	Guided-Mode Resonance
BIC	Bound State in the Continuum

Continued on next page

Abbreviation	**Full Form**
$\mathbf{LiNbO_3}$	Lithium Niobate
$\chi^{(2)}$	Second-Order Susceptibility
$\chi^{(3)}$	Third-Order Susceptibility
FOM	Figure of Merit
CVD	Chemical Vapor Deposition
h-BN	Hexagonal Boron Nitride
$\mathbf{SiO_2}$	Silicon Dioxide
$\mathbf{Al_2O_3}$	Aluminum Oxide
$\mathbf{HfO_2}$	Hafnium Dioxide
LCP	Liquid Crystal Polymer
BCB	Benzocyclobutene
HR-Si	High-Resistivity Silicon
G	Gain (dBi)
η	Efficiency
HPBW	Half-Power Beamwidth
BW	Bandwidth
IBW	Impedance Bandwidth
FBW	Fractional Bandwidth
F/B	Front-to-Back Ratio
EBL	Electron-Beam Lithography
NIL	Nanoimprint Lithography
DUV	Deep Ultraviolet
FPGA	Field-Programmable Gate Array
V_g	Gate Voltage
$V_{\mathbf{CNP}}$	Charge Neutrality Point Voltage
THz	Terahertz (0.1–10 THz)
sub-THz	Sub-Terahertz (below 0.3 THz)
5G	Fifth Generation
6G	Sixth Generation
7G	Seventh Generation
IoT	Internet of Things
TE	Transverse Electric
TM	Transverse Magnetic
$\mathbf{TE_0}$	Fundamental TE mode
$\mathbf{TM_0}$	Fundamental TM mode
$\mathbf{TM_1}$	First higher-order TM mode
z-cut	Z-cut Lithium Niobate Crystal
$\mathbf{C_4}$	Four-fold Rotational Symmetry
GaAs	Gallium Arsenide
GaP	Gallium Phosphide

Continued on next page

Abbreviation	**Full Form**
AlGaAs	Aluminum Gallium Arsenide
$\mathbf{MoS_2}$	Molybdenum Disulfide
$\mathbf{WSe_2}$	Tungsten Diselenide
TMD	Transition Metal Dichalcogenide
Ni	Nickel
Cu	Copper
Au	Gold
Ti	Titanium
λ_0	Free-space wavelength
$\lambda_{\mathbf{SPP}}$	Surface plasmon polariton wavelength
ε_0	Vacuum permittivity
ε_r	Relative permittivity
$\hbar$	Reduced Planck constant
k_B	Boltzmann constant
e	Electron charge
h	Planck constant

Chapter 1

Introduction

The rapid evolution of wireless communication technologies, from fifth generation (5G) to the envisioned sixth generation (6G) and beyond, is driving an ever-growing demand for devices capable of supporting ultra-high data rates, massive connectivity, low latency, and adaptive communication links. With the push towards higher carrier frequencies, the terahertz (THz) spectrum (0.1-10 THz) has emerged as a key candidate to enable future communication systems, sensing platforms, and imaging technologies. The THz band offers a wide, underutilized spectrum that can support multi-gigabits per second data transmission, ultra-dense network architectures, and advanced functionalities such as secure short-range links, high resolution sensing and spectroscopy [1–3].

However, the shift into THz domain presents significant challenges in device design, particularly for antennas and metasurfaces, which serve as the fundamental interface between free-space electromagnetic waves and electronic system. Traditional metallic antennas and passive metasurfaces exhibit fixed operating characteristics, such as radiation patterns, frequency, and polarization, making them inadequate for emerging applications that require dynamic adaptability, multifunctionality, and tunability. As modern communication systems grow increasingly complex, there is a critical need for antenna and metasurface platforms capable of dynamically reconfiguring their electromagnetic response in real time. Such reconfigurable solutions enable multiple functionalities such as frequency tuning, polarization control and beam steering without the need for multiple discrete devices, offering a more efficient and compact approach to advanced communications.

1.1 Motivation for Reconfigurable Antennas and Metasurfaces

Conventional antennas are typically designed to operate at a fixed frequency and with predefined radiation patterns. While this was sufficient for earlier communication systems, the demand of dynamic frequency allocation, adaptive beam steering, polarization control, and multifunctional operation in 5G/6G networks render fixed-function devices obsolete. Reconfigurable antennas and metasurfaces offer a transformative solution by enabling real-time control over key electromagnetic properties such as frequency, polarization state, radiation direction, and even nonlinear response [4–6].

The key motivation for developing reconfigurable devices lies in their ability to:

1. **Enhance spectral efficiency:** Adapt to dynamic frequency bands and spectrum-sharing scenarios [7, 8].
2. **Reduce hardware complexity:** Enable multiple functionalities in a single platform [9, 10].
3. **Improve communication reliability:** Provide adaptive beamforming and radiation pattern control [11, 12].
4. **Enable multifunctional systems:** Integrate linear and nonlinear functionalities for sensing, communication, and signal processing [13, 14].

Moreover, reconfigurable metasurfaces (engineered surfaces with subwavelength elements) extend this adaptability to the manipulation of electromagnetic wavefronts, enabling functionalities such as beam steering, focusing, harmonic generation, and wavefront shaping in compact, planar devices [15–17]. These capabilities are particularly valuable in the THz regime, where fabrication constraints and device miniaturization are major challenges [18, 19].

1.2 Role of Graphene in THz Devices

Among the materials explored for next generation reconfigurable platforms, graphene has emerged as a promising material due to its tunable surface conductivity and plasmonic response [20, 21]. As a two-dimensional material composed of a single layer of carbon atoms arranged in a hexagonal lattice, graphene exhibits the following properties:

1. **Tunable surface conductivity:** Its Fermi level can be dynamically modulated using electrostatic gating or chemical doping, enabling real-time control of frequency response [22–24].

2. **Strong plasmonic confinement:** Graphene supports highly confined surface plasmon polaritons (SPPs) in the THz and mid-infrared regimes, enabling miniaturization and field confinement [25–27].

3. **Ultrafast carrier dynamics:** It enables rapid switching, suitable for dynamic beam steering and frequency tuning [28, 29].

4. **Integration versatility:** Graphene can be combined with nonlinear or magneto-optical materials to achieve hybrid functionalities [30–32].

These properties of graphene, such as tunable surface conductivity, plasmonic response, and optical transparency, enable the design of the graphene dipole antenna with parasitic elements presented in this thesis [33, 34]. Exploiting these properties, the proposed antenna achieves pattern reconfigurability across the 360-degree azimuthal plane and can be deposited on a polyimide substrate, highlighting compact, tunable, and multifunctional operation in the sub-THz regime [35].

1.3 Research Objectives and Scope

The primary objective of this Ph.D. thesis is to design, analyze, and demonstrate graphene-based reconfigurable antennas and nonlinear metasurfaces capable of operating in the THz regime and beyond. This research exploits graphene's properties, such as high carrier mobility, tunable plasmonic response, and compatibility with planar and flexible substrates, to realize devices with enhanced functionality and versatility. In particular, these properties enable the design of antennas with pattern reconfigurability across the 360-degree azimuthal plane and metasurfaces capable of nonlinear frequency conversion and multifunctional operation, directly linking graphene's material properties to the contributions and outcomes of this thesis.

The key objectives of this work are:

1. Design of a transparent pattern-reconfigurable graphene dipole antenna using electrostatic biasing for dynamic radiation control.

2. Design of a magnetically biased graphene antenna that leverages magneto-plasmonic effects for beam steering and enhanced radiation patterns.

3. Design of a hybrid nonlinear metasurface based on graphene-lithium niobate for second harmonic generation (SHG) and third-harmonic generation (THG), enabling multifunctional frequency conversion in a compact platform.

By combining the tunable plasmonic response of graphene with the strong nonlinear coefficients of lithium niobate, the proposed design addresses the current lack of reconfigurable, multifunctional nonlinear metasurfaces, providing a pathway toward compact and efficient frequency conversion devices for sensing and communication systems [30–32].

1.4 Research Significance and Novelty

The novelty of this thesis lies in the unified implementation of multiple reconfigurability approaches-electrostatic biasing, magnetic biasing, and nonlinearity-within a single graphene-based platform. Unlike prior studies, which typically investigate these approaches in isolation, this thesis highlights their combined effect in THz antennas and metasurfaces, enabling simultaneous control over radiation patterns and frequency conversion. This integrated approach provides a level of multifunctionality and dynamic tunability that has not been previously reported, offering a distinct advancement over existing designs in the field. To the best of my knowledge, this is the first work to combine electrostatic biasing, magnetic biasing, and nonlinear approaches within a single platform. This integration advances the state of the art by enabling simultaneous control of radiation in antennas and frequency conversion in metasurfaces.

1. **Electrostatic reconfigurability:** Real-time control of antenna patterns and frequency response.
2. **Nonlinear metasurface functionality:** Efficient frequency conversion and harmonic generation.
3. **Magnetic tuning:** Directional control and dynamic beam steering without altering the device geometry.

1.5 Thesis Organization

The remainder of the thesis is structured as follows:

- **Chapter 2** - Design of a Programmable Graphene Dipole Antenna Using Electrostatic Biasing: Presents the design methodology, simulation results, and performance analysis of the first proposed antenna.
- **Chapter 3** - Pattern Reconfigurability of Graphene Dipole Antennas via Magnetic Biasing: Discusses the design, theory, and reconfiguration of magnetically biased in-plane and out-of-plane graphene parasitic elements.
- **Chapter 4** - Design of a Hybrid Graphene-Lithium Niobate Nonlinear Metasurface for Dual-Harmonic Generation: Presents the design and analysis of a hybrid nonlinear metasurface that enables SHG and THG.

- **Chapter 5** - Conclusions and Future Work: Summarizes the key findings and outlines possible directions for future research.

In summary, this thesis is motivated by the need for reconfigurable, tunable, and multifunctional THz and beyond-THz devices to support next-generation communication systems and sensing devices. By harnessing the extraordinary properties of graphene and integrating them with electrostatic, nonlinear, and magneto-optical mechanisms, this research aims to advance the state of the art in antenna and metasurface design. The outcomes of this work are expected to contribute to the development of flexible, high-performance THz platforms, paving the way for future applications in 6G communications, spectroscopy, and beyond.

Chapter 2

Design of a Programmable Graphene Dipole Antenna Using Electrostatic Biasing

2.1 Introduction

In our modern information-driven society, highly developed electromagnetic antennas operating in the micro- and millimeter-wave frequency bands have become indispensable elements [36,37]. They assume a pivotal role across a broad spectrum of applications, including multimedia broadcasting, mobile and satellite communications, radar systems, environmental monitoring, and medical technology [38–45]. This diverse array of applications has driven substantial research and technological progress in this field over the past few decades. Nevertheless, the rapid growth of the information-driven society continually presents a set of demanding and occasionally conflicting technological demands. These challenges are particularly pronounced for antennas operating in Terahertz (THz) and sub-THz frequency ranges, where performance is limited by several factors, including conductor and dielectric losses, reduced radiation efficiency, and fabrication tolerances at subwavelength scales. In addition, the realization of high-gain and high-directive radiation patterns are constrained by the compact size of the devices, while impedance matching and integration with active components become increasingly difficult at higher frequencies. Furthermore, beam steering, reconfigurability, and multifunctionality in compact antenna platforms introduce additional design complexity, especially under stringent constraints in power consumption and spectral efficiency.

One apparent solution to address these requirements involves elevating the operating frequency of existing antennas, effectively tapping into the terahertz (THz) spectrum, characterized by electromagnetic waves with frequencies ranging from 0.1 to 10 THz [46–49]. The THz spectrum presents unique opportunities for cutting-edge applications. These applications encompass the attainment of wireless communications with data transmission rates spanning from hundreds of gigabits to terabits per second, the development of high-speed compact processing systems, the capability to discern specific chemical or biological processes, ultra-high-resolution real-time material inspection, screening, non-invasive material identification via spectroscopy, exploration of cosmic background radiation, and the detection of gases on Earth and in other planetary atmospheres, among a multitude of other potential use cases [50–53]. Despite recent progress, the practical realization of terahertz applications remains constrained by fundamental limitations in source, detectors, and antennas. Electronic devices are restricted by carrier transit-time effects and parasitic losses, while photonic approaches suffer from low photon energies and inefficient emission and detection. These challenges, along with material losses and low device efficiencies, defined the so-called "THz gap", a technology difficult region between electronics and photonics.

In a closely related context, graphene, recognized as a two-dimensional carbon structure, has recently ignited extensive and interdisciplinary research initiatives due to its extraordinary electromagnetic, mechanical, electrical, and thermal attributes [20, 54–62]. Graphene enables the propagation of surface Plasmon polaritons (SPPs), which can achieve substantial wave confinement, exhibit low loss, and possess the remarkable quality of adjustability through electrical or magnetic manipulation, as well as chemical doping. Significantly, as this plasmonic response materializes within the terahertz and infrared frequency ranges, graphene has rapidly emerged as a highly promising foundation for terahertz transceivers and optoelectronic systems. While there are possibilities of supporting SPPs through composite structures in the terahertz domain, graphene remains unique as the sole pristine material capable of delivering such a plasmonic response [63]. This distinctive attribute paves the way for exciting and unforeseen avenues in wave control and radiation within this frequency spectrum. Graphene's unique properties have enabled the development of compact and adaptable antennas that operate at terahertz frequencies. These antennas, including resonant, leaky-wave, and reflectarray types, offer exceptional radiation efficiency and versatile functions [64–69]. Unlike traditional metallic antennas, they resonate at much lower frequencies and take full advantage of graphene's conductivity for reconfiguration [70]. Additionally, graphene plasmonics can potentially serve as the building blocks for various transceiver components, such as switches, phase-shifters, filters, and modulators. It's worth noting that graphene can exhibit non-reciprocal propagation and significant Faraday rotation when exposed to magnetostatic fields [71]. However, the use of bulky magnets in this context contradicts the goal of achieving miniaturization with graphene plasmonics.

These breakthroughs rely on the spatial and temporal modulation of graphene's conductivity, allowing us to disrupt the fundamental principle of time-reversal symmetry (reciprocity) without the need for ferromagnetic materials or magneto-optical effects. By integrating these components and functionalities into a single, compact device, enhanced performance and extended capabilities in terahertz technology can be achieved [72]. This progress could open the door to terahertz communication and sensing systems that are compatible with silicon technology, delivering unprecedented levels of performance and capabilities.

It's noteworthy that, to date, most graphene-based antennas and devices operating in the terahertz (THz) and sub-THz frequency ranges remain largely at the level of theoretical proposals and design concepts, with their electromagnetic behavior largely predicted through simulations rather than experimental validations. However, it's essential to emphasize that recent experimental endeavors have unequivocally validated the existence of confined and tunable Surface Plasmon Polaritons (SPPs) in graphene [73, 74]. This physical phenomenon serves as the fundamental basis for all the antennas and components discussed in this context. Earlier experiments had encountered significant limitations, as they dealt with graphene of subpar quality, rendering it practically unsuitable for any electrodynamic application beyond its role as a tunable resistor. However, recent advances in large area chemical vapor deposition (CVD) graphene growth and transfer techniques have yielded high-quality monolayer graphene with tunable conductivity and low loss, making it suitable for reconfigurable antennas and metasurfaces at sub-THz frequencies. This substantially hindered the practicality of much of the research conducted. Nonetheless, recent years have seen significant progress in this area, driven by widespread global initiatives focused on refining fabrication methods. Remarkably, there have been tremendous advancements in enhancing the mobility of graphene structures, particularly when they are inserted between layers of hexagonal boron nitride [75–77]. These advancements have far exceeded the quality standards required for all the antennas and devices discussed in the existing literature.

More recently, despite the complexities associated with fabrication and measurement techniques, experimental validations have been successfully conducted for certain exciting terahertz (THz) detectors and modulators [78–80]. These experimental results have surpassed prior state-of-the-art achievements and have exhibited exceptional alignment with numerical predictions. The pioneering experimental research conducted so far has merely scratched the surface of the vast potential of terahertz (THz) plasmonics using graphene and other two-dimensional materials like black phosphorus, 2D dichalcogenides, and oxides [81–83]. This underscores the fact that this exciting field is still in its early stages, and the future of graphene and 2D materials in antenna research appears to be even more promising than many initially envisioned during its nascent phases.

To overcome these limitations, this chapter proposes a programmable graphene dipole antenna with eight parasitic elements. Unlike conventional antennas, the proposed design leverages 2D graphene's tunable surface conductivity and structural symmetry to achieve dynamic 360-degree beam steering, addressing the key challenges of mutual coupling, pattern reconfigurability, and system complexity in the sub-THz wireless systems.

2.2 Historical background of Graphene

In 2010, the Nobel Prize in physics honored pioneering research in the field of graphene [54], a two-dimensional honeycomb lattice of carbon atoms and serves as the fundamental building block for other carbon-based nanomaterials, including one-dimensional (1D) carbon nanotubes and zero-dimensional (0D) fullerenes, as illustrated in Fig. 2.1(a). The interatomic distance between neighboring carbon atoms in the graphene lattice is approximately 0.142 nm. Furthermore, the atomic arrangement at the graphene edges, which may adopt either zigzag or armchair configurations as shown in Fig. 2.1(b), significantly influences its electronic properties [84, 85], particularly in nanoscale structures.

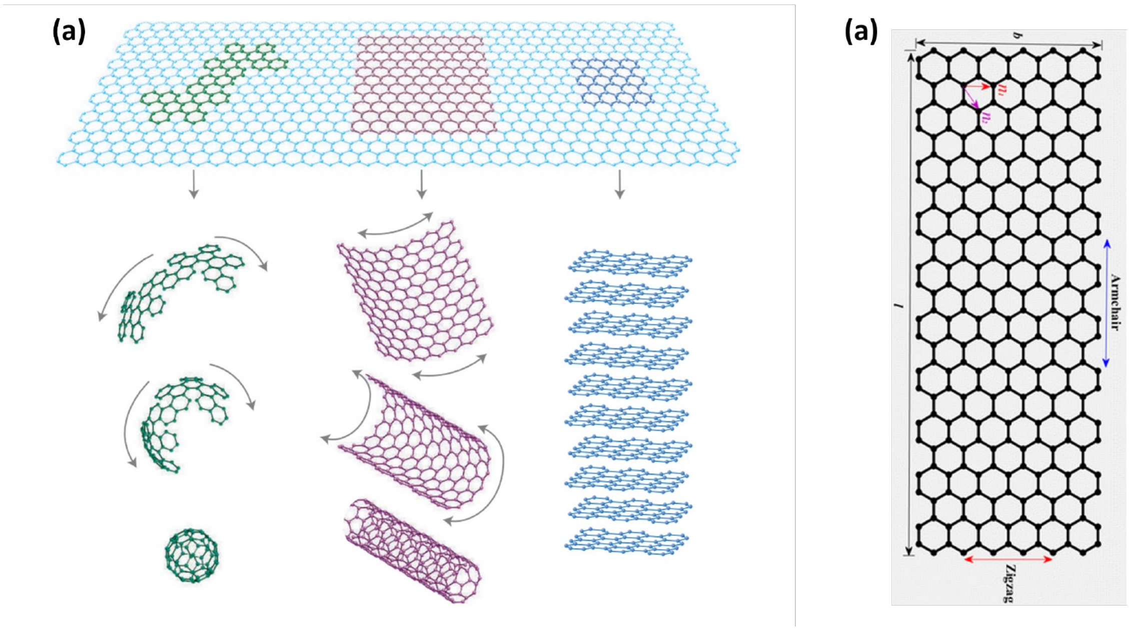

Figure 2.1: Lattice structure of graphene. (a) Carbon nanostructures derived from graphene, including fullerene, carbon nanotubes, and graphite [54]. (b) Edge configurations of graphene showing the two principal carbon atom arrangements: zigzag and armchair structures [84].

A single graphene sheet possesses an extremely small thickness of approximately 0.35 nm. When multiple graphene layers are stacked together, the resulting material forms graphite. Generally, structures containing more than ten graphene layers are classified as thin graphite films rather than graphene materials. In graphene, carbon atoms exhibit sp^2 hybridization, forming strong covalent σ-bonds within the plane, while electrons in the out-of-plane p-orbitals create weaker π-bonds. These delocalized π-electrons can move freely across the graphene sheet, contributing to its remarkable electronic behavior.

The unique lattice configuration of graphene gives rise to exceptional physical properties. The strong σ-bonds provide outstanding mechanical strength and high tensile durability, whereas the two-dimensional atomic arrangement enables high sensitivity to adsorbed or desorbed gas molecules. Additionally, graphene exhibits excellent thermal conductivity due to the robust covalent bonding between carbon atoms and distinctive optical properties that permit the visualization of a single atomic layer [86]. The electrical characteristics of graphene are primarily governed by the vertically oriented π-bonds, while its mechanical stability is mainly associated with the in-plane σ-bonds [84].

Graphene also exhibits an extraordinary electronic band structure. Specifically, the conduction and valence bands intersect at the Dirac point, resulting in a zero-bandgap semiconductor, as depicted in Fig. 2.2. Consequently, charge carriers in graphene behave as massless Dirac fermions with a linear energy–momentum dispersion relation [87]. At the charge neutrality point, the minimum conductivity of graphene is frequency independent and can be expressed as

$$\sigma_{\min} = \frac{4e^2}{h} \tag{2.1}$$

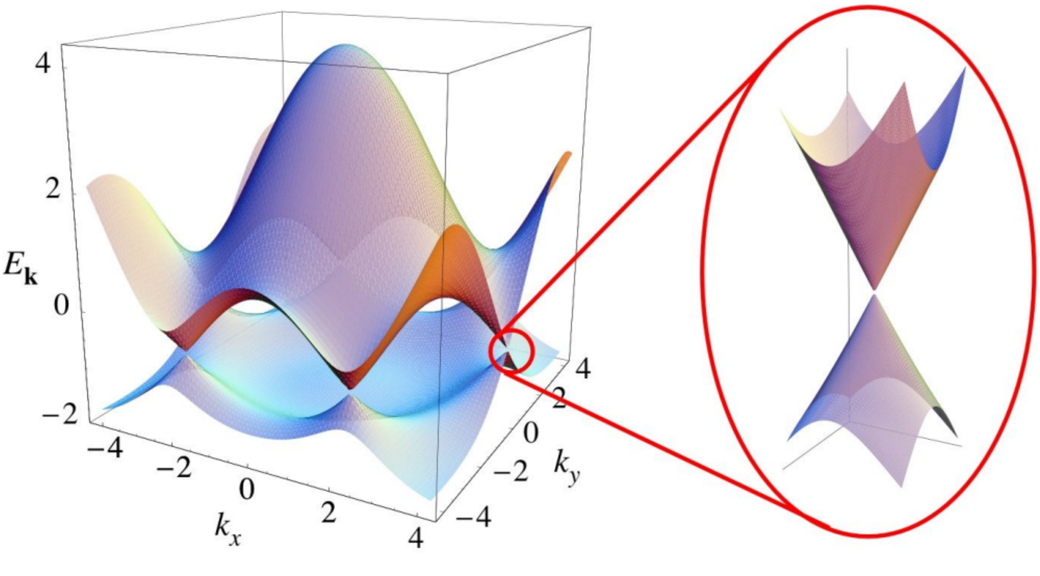

Figure 2.2: Electronic band structure of graphene illustrating the valence and conduction bands intersecting at the Dirac point, exhibiting a linear dispersion relation and a zero bandgap characteristic [88]

where e denotes the electron charge and h represents Planck's constant. However, the optical and electrical properties of graphene are strongly influenced by doping. For doped graphene, the conductivity depends on the operating frequency, Fermi level, and carrier relaxation time, and can be described using the Kubo formalism [26, 89, 90] as

$$\sigma(\omega) = -\frac{ie^2(\omega + i\tau^{-1})}{\pi\hbar^2}\left[\frac{1}{(\omega + i\tau^{-1})^2}\int_0^\infty \left(\frac{\partial f_d(E)}{\partial E} - \frac{\partial f_d(-E)}{\partial E}\right) E\,dE - \int_0^\infty \frac{f_d(-E) - f_d(E)}{(\omega + i\tau^{-1})^2 - 4(E/\hbar)^2}\,dE\right] \tag{2.2}$$

where f_d is the Fermi–Dirac distribution function, k_B is the Boltzmann constant, T is the temperature, $\hbar$ is the reduced Planck constant, ω is the angular frequency, E_F is the Fermi level, and τ denotes the carrier relaxation time [89]. A detailed derivation is provided in Annex A of this thesis.

The carrier scattering frequency is inversely related to the relaxation time, which for graphene can be expressed as

$$\tau = \frac{\mu E_F}{e v_F^2} \tag{2.3}$$

where μ is the carrier mobility and $v_F \approx 10^6$ m/s is the Fermi velocity.

The total conductivity of graphene comprises both interband and intraband contributions. In the terahertz (THz) frequency regime, the interband contribution becomes negligible, allowing the conductivity to be accurately approximated by the intraband term alone. Figure 2.3 illustrates the THz conductivity characteristics of graphene for different material parameters.

From the conductivity plots in Fig. 2.3, the influence of the Fermi level and relaxation time on graphene conductivity becomes evident. The real and imaginary components of conductivity exhibit distinct behaviors. At lower frequencies, graphene predominantly behaves as a resistive material, where the real component of conductivity, $\text{Re}\{\sigma\}$, is significantly larger than the imaginary component, $\text{Im}\{\sigma\}$. As the frequency increases, the real part decreases while the imaginary part increases until the condition $\text{Re}\{\sigma\} = \text{Im}\{\sigma\}$ is reached. Beyond this transition frequency, graphene exhibits predominantly reactive behavior, characterized by $\text{Im}\{\sigma\}$ exceeding $\text{Re}\{\sigma\}$. Although the imaginary component also decreases at higher frequencies, its reduction occurs more gradually compared to the real component.

The key requirement for a 2D sheet to support surface plasmon polaritons is that the imaginary part of its surface conductivity must be negative, i.e. $\text{Im}(\sigma) < 0$, which corresponds to an inductive surface reactance. At sub-THz frequencies, graphene's intraband (Drude) conductivity dominates, and its imaginary part is

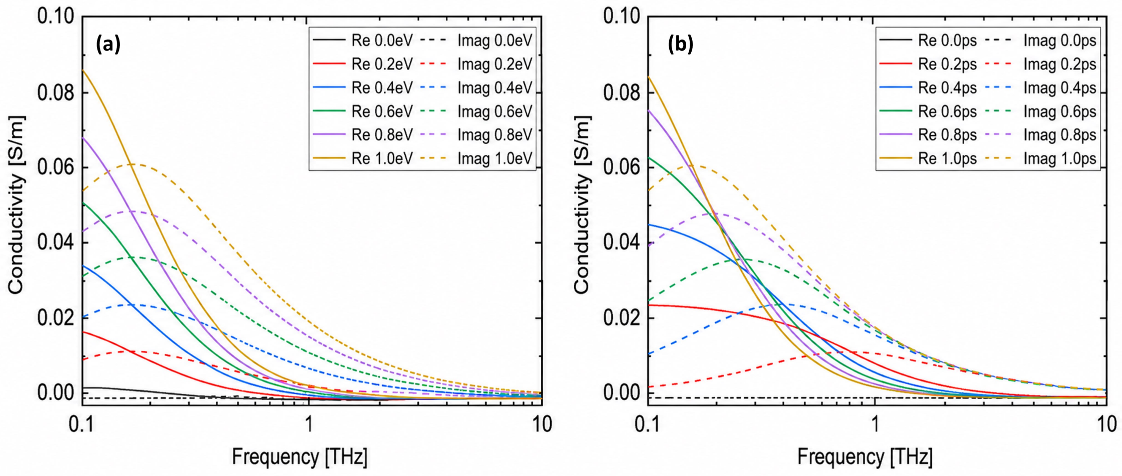

Figure 2.3: Calculated conductivity of a monolayer graphene sheet in the THz frequency range. (a) Conductivity comparison for graphene with a relaxation time of 1.2 ps at different chemical potentials. (b) Conductivity comparison for graphene with a chemical potential of 1.2 eV under different relaxation times.

given by

$$\mathrm{Im}(\sigma_{\text{intra}}) = -\frac{e^2\mu_c}{\pi\hbar^2}\cdot\frac{\omega}{\omega^2+\tau^{-2}} \; < \; 0.$$

This negative imaginary part arises from the inductive Drude-like response and enables tightly confined SPP modes with $\lambda_{\text{SPP}} \ll \lambda_0$. In contrast, conventional metals (e.g., copper, gold) have a positive imaginary part of conductivity at sub-THz frequencies, and therefore they do not support confined SPPs in this frequency range. Metals support SPPs only at optical frequencies, where their real permittivity becomes negative. Thus, the ability of graphene to support SPPs at sub-THz and THz frequencies stems from the negative imaginary part of its intraband conductivity, not merely from its tunability.

For a constant relaxation time, increasing the Fermi level enhances both the real and imaginary conductivity components throughout the THz frequency range. Conversely, increasing the relaxation time shifts the frequency at which $\mathrm{Re}\{\sigma\} = \mathrm{Im}\{\sigma\}$ toward lower frequencies. When the relaxation time is relatively small, graphene conductivity remains mainly resistive over a wider frequency range.

The relaxation time is strongly associated with the quality of graphene and depends on lattice imperfections and defects within the carbon arrangement. In contrast, the Fermi level can be tuned either chemically or electrically since it is directly related to the carrier concentration according to [90]

$$E_F = \hbar v_F \sqrt{\pi n} \tag{2.4}$$

where n represents the carrier density. Depending on the type of carriers, electrons or holes, the Fermi level shifts toward the conduction or valence band, respectively, as illustrated in Fig. 2.4. For plasmonic graphene THz antennas, precise control over graphene conductivity and carrier concentration is of critical importance. Unlike conventional semiconductors, substitutional p-type or n-type doping by replacing carbon atoms within the graphene lattice is not preferred because it increases carrier scattering and alters the intrinsic chemical properties of graphene due to its fully exposed two-dimensional structure [92]. Consequently, graphene doping is commonly achieved either through chemical adsorption of atoms or molecules on its surface or via external electrostatic gating [91].

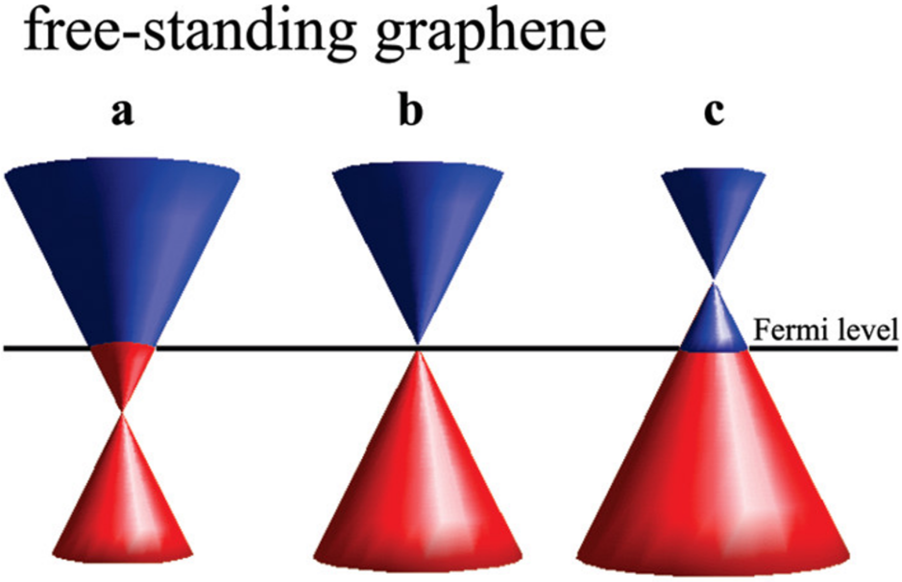

Figure 2.4: Electronic band structures of graphene under different doping conditions: (a) n-type graphene, (b) pristine graphene, and (c) p-type graphene [91]

Chemical doping of graphene is often difficult to control because adsorbed molecules interacting through van der Waals or London forces can alter the electronic structure and reduce carrier mobility [93]. Effective n-type or p-type doping depends strongly on the selection of suitable dopant molecules. In particular, the relative positions of the highest occupied molecular orbital (HOMO) and lowest unoccupied molecular orbital (LUMO) determine the direction of charge transfer [94]. Moreover, even the substrate supporting the graphene layer can induce unintentional chemical doping. Electrostatic doping through gate biasing is the most widely adopted technique for graphene tuning. In this approach, an applied gate voltage induces either positive or negative charge carriers within the graphene sheet. A major advantage of electrostatic doping is its reversibility, since the original doping state can be restored once the bias voltage is removed. Furthermore, the doping level can be dynamically controlled by adjusting the applied voltage.

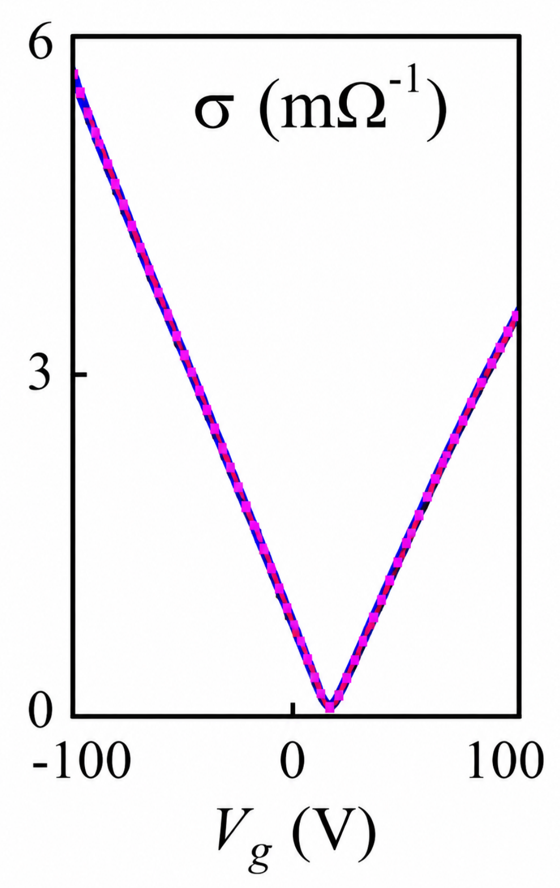

Figure 2.5: Ambipolar electric field effect observed in single-layer graphene [20]

The first experimental demonstration of the electric field effect in graphene [20], shown in Fig. 2.5, utilized a graphene sheet deposited on a silicon dioxide/silicon (SiO_2/Si) substrate with a top-gate bias configuration.

Experimental observations revealed three distinct doping regions in graphene. Two regions were dominated exclusively by either electrons or holes, while the third represented a transition regime where one carrier type gradually replaced the other. Additionally, graphene maintained a finite conductivity even in the absence of an external electric field, and its conductivity could not be completely suppressed. This residual conductivity was attributed to unintentional chemical doping caused by water molecules adsorbed from the surrounding environment.

The carrier concentration induced by electrostatic gating can be determined from

$$n = \frac{\varepsilon_0 \varepsilon_r V_g}{t_d e} \tag{2.5}$$

where ε_r is the dielectric constant, V_g is the applied gate voltage, and t_d denotes the dielectric thickness. Accordingly, the Fermi level induced by gate bias can be expressed as

$$E_F = \hbar v_F \sqrt{\frac{\pi \varepsilon_0 \varepsilon_r (V_g - V_0)}{t_d e}} \tag{2.6}$$

where V_0 accounts for the initial environmental and substrate-induced doping effects.

The graphene carrier mobility can also be extracted from the transfer characteristics shown in Fig. 2.5 [95]. In the electrostatic bias configuration illustrated in Fig. 2.6(a), graphene functions as the conductive channel of a field-effect transistor (FET), connecting the source and drain terminals while a gate voltage is applied between the source and the back gate. Carrier mobility can be determined using several techniques, including the direct transconductance method, fitting method, and transfer length method.

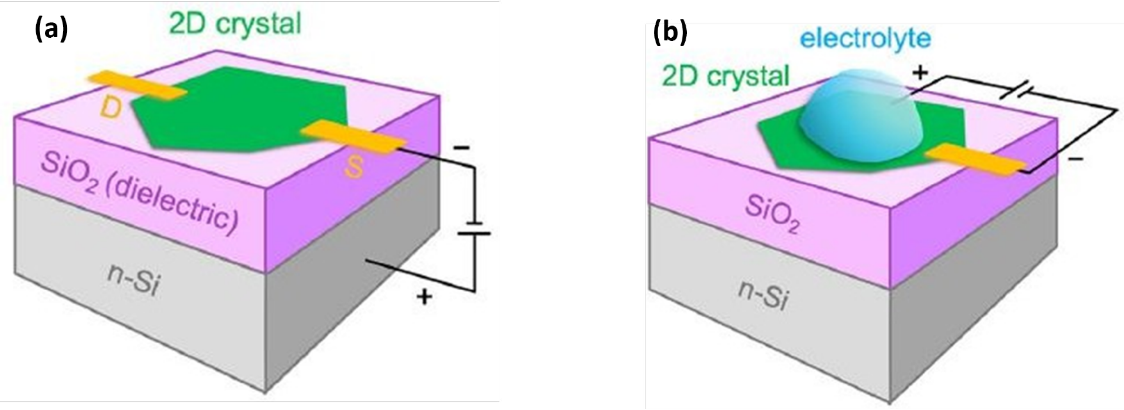

Figure 2.6: Comparison of dielectric and electrolyte gate tuning techniques [96]. (a) Dielectric back-gating configuration: the applied voltage is established between the bottom electrode (n-doped silicon) and the top electrode, which is connected to the two-dimensional material through a SiO_2 dielectric layer. (b) Electrolyte top-gating configuration: the applied voltage is established between the ionically conductive electrolyte and the two-dimensional crystal.

In the direct transconductance method, the mobility is calculated from the gate-voltage-dependent transconductance as

$$\mu = \frac{g_m L_g}{W_g V_{ds} C_g} \tag{2.7}$$

where L_g and W_g denote the graphene channel length and width, respectively, V_{ds} is the drain–source voltage, C_g is the dielectric capacitance, and g_m is the transconductance obtained from the slope of the transfer curve in Fig. 2.5. However, this method typically underestimates the mobility because it neglects the contact resistance between graphene and metallic electrodes.

In the fitting method, carrier mobility, contact resistance, and residual carrier concentration are treated as fitting parameters to model the total device resistance according to

$$R_{\text{total}} = R_c + \frac{L_g}{W_g \mu n (V_g - V_0)} \tag{2.8}$$

where R_c represents the contact resistance and n is the gate-dependent carrier concentration. Nevertheless, this method may overestimate the mobility because it assumes a constant mobility independent of carrier density.

The transfer length method is generally regarded as the most accurate technique for determining graphene carrier mobility. This approach utilizes multiple devices with varying channel lengths to accurately extract the contact resistance as a function of gate voltage.

More recently, electrolyte-gated tuning techniques have emerged as highly efficient alternatives for modifying the chemical potential of two-dimensional materials [96, 97]. In conventional dielectric-gated systems, a gate electrode applies an electric field across a dielectric layer to tune the graphene chemical potential, as illustrated in Fig. 2.6(a). In contrast, electrolyte gating employs an electrolyte solution as the gating medium, as depicted in Fig. 2.6(b), enabling significantly enhanced electrostatic modulation efficiency.

The primary advantage of employing an electrolyte as a gate material lies in the formation of an electrical double layer of mobile ions at the interface between the two-dimensional material and the electrolyte. This ultra-thin ionic layer produces an interface capacitance significantly larger than that achieved using conventional dielectric gating techniques. Consequently, electrolyte gating enables substantially higher carrier concentrations under an applied bias compared to dielectric-based tuning methods.

For graphene tuned through electrolyte gating, the carrier concentration depends on the applied gate voltage, the quantum capacitance of graphene, and the gate capacitance, which is determined by the electrolyte thickness and permittivity. The relationship between the applied gate voltage and the graphene Fermi level can be expressed as

$$V_g = \frac{E_{F0}}{e} + \frac{E_F}{e} + \phi' \tag{2.9}$$

where V_g is the applied gate voltage, E_{F0} represents the initial Fermi level of graphene, E_F is the Fermi level achieved under bias, and ϕ' denotes the electrostatic potential difference between graphene and the electrolyte gate.

The Fermi level is given by

$$E_F = \mathrm{sgn}(n)\hbar v_F \sqrt{\pi n} \tag{2.10}$$

where n is the carrier concentration, $\hbar$ is the reduced Planck constant, and v_F is the Fermi velocity.

The electrostatic potential difference ϕ' can be written as

$$\phi' = \frac{ne}{C_{g2L}} \tag{2.11}$$

where C_{g2L} is the electrical double-layer capacitance of the electrolyte. This capacitance can be expressed as

$$C_{g2L} = \frac{\varepsilon_0 \varepsilon_r}{\lambda_D} \tag{2.12}$$

where ε_r denotes the dielectric constant of the electrolyte and λ_D represents the Debye length, corresponding to the thickness of the electrical double layer formed at the interface.

Moreover, the limited charge-screening capability of graphene at Fermi energies exceeding the thermal energy must also be considered. This effect is described by the quantum capacitance C_q, which is defined as

$$C_q = \frac{2e^2 E_F}{\pi(\hbar v_F)^2} \tag{2.13}$$

Accordingly, the electrolyte-gated tuning of the graphene Fermi level can be described as

$$V_g = \frac{E_{F0}}{e} + \frac{E_F}{e} + \phi' = \mathrm{sgn}(E_F)\frac{\pi(\hbar v_F)^2}{2e^3}\left(C_q + \frac{C_q^2}{2C_{g2L}}\right) \tag{2.14}$$

The exceptional electrical properties of graphene make it highly attractive for a wide range of electronic and electromagnetic applications. In the terahertz (THz) frequency regime, graphene-based antennas offer significant miniaturization capabilities due to the plasmonic behavior of graphene. Furthermore, the tunability of graphene conductivity enables the realization of reconfigurable antennas operating over multiple frequency bands, as discussed in subsequent sections.

2.2.1 Surface Plasmon Polaritons in Graphene

In contrast to conventional metals, graphene exhibits fundamentally different plasmonic behavior. Owing to its atomically thin structure, graphene enables significantly stronger confinement of surface plasmon polaritons (SPPs) at the material interface. Furthermore, the charge carriers in graphene behave as massless Dirac fermions, resulting in considerably longer plasmon propagation lengths. Another important advantage of graphene is the possibility of dynamically tuning the carrier concentration, which directly enables control of the SPP wavelength and propagation characteristics.

Considering an infinite graphene sheet located at the interface between two dielectric media with permittivities ε_t and ε_b, corresponding to the top and bottom materials respectively (Fig. 2.7), the solution of Maxwell's equations reveals that, unlike conventional metals, graphene can support both transverse electric (TE) and transverse magnetic (TM) plasmonic modes under the collisionless approximation and at zero temperature [90]. As the temperature and carrier density increase, the TM mode becomes dominant within the terahertz (THz) frequency range, whereas in conventional metals, SPPs typically exist only at optical frequencies.

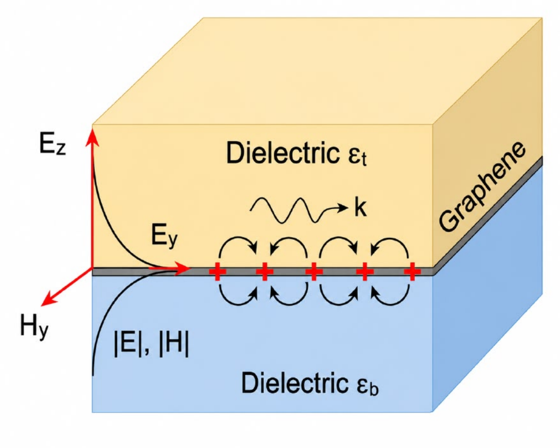

Figure 2.7: Schematic of surface plasmon polaritons (SPPs) propagating along a graphene sheet at the interface between two dielectric media. The SPP wave travels in the x-direction, with the electromagnetic field strongly confined to the graphene interface [98].

For graphene, the TM plasmonic mode can be described by

$$\frac{\varepsilon_t}{\sqrt{k_{\mathrm{SPP}}^2 - \varepsilon_t \omega^2/c^2}} + \frac{\varepsilon_b}{\sqrt{k_{\mathrm{SPP}}^2 - \varepsilon_b \omega^2/c^2}} + \frac{i\sigma}{\omega \varepsilon_0} = 0 \tag{2.15}$$

where σ represents the graphene conductivity.

For doped graphene deposited on a dielectric substrate ($\varepsilon_b \neq 1$) with air as the superstrate ($\varepsilon_t = 1$), and considering only the intraband contribution to the graphene conductivity in Eq. (2.15) can be simplified as [26, 90, 98–100]

$$k_{\mathrm{SPP}} = \frac{\pi \hbar^2 \varepsilon_0 (\varepsilon_b + 1)\omega(\omega + i/\tau)}{e^2 E_F} \tag{2.16}$$

The graphene surface plasmon polariton is strongly dependent on the graphene chemical potential. By modifying the carrier concentration, and consequently the Fermi level, the propagation properties of graphene SPPs can be dynamically tuned. This tunability represents a major advantage over traditional metallic plasmonic

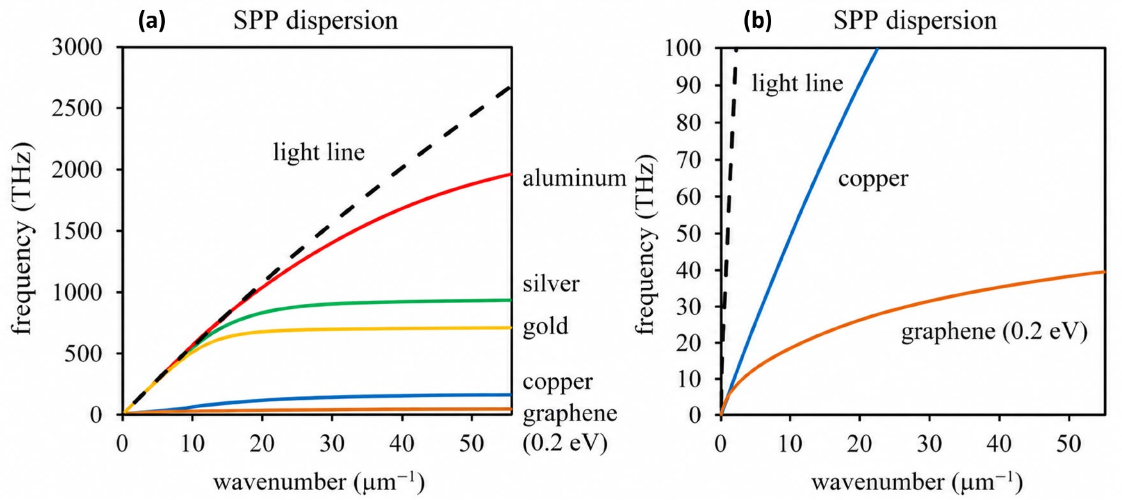

Figure 2.8: SPP dispersion relations for different noble metals and graphene. (a) Dispersion characteristics showing that the SPP modes of noble metals deviate from the light line only at frequencies above approximately 500 THz. (b) Rescaled dispersion plot highlighting that graphene with a chemical potential of 0.2 eV supports SPP modes within the lower THz frequency range [89].

structures. Figure 2.8 presents a comparison between the dispersion relation of graphene with a chemical potential of 0.2 eV and those of several conventional metals. In metallic materials, the SPP dispersion relation deviates from the light line only at frequencies exceeding approximately 500 THz. In contrast, graphene exhibits this deviation at frequencies below 10 THz, demonstrating its suitability for low-frequency plasmonic applications.

The unique characteristics of SPPs at metal–dielectric interfaces, including strong field confinement and subwavelength propagation, have enabled numerous applications in the infrared and optical frequency ranges. However, for THz applications, graphene emerges as an exceptionally promising plasmonic material because graphene-supported SPPs naturally exist within this frequency band. Additionally, graphene provides superior tunability and dynamic control of plasmonic properties compared to conventional metallic structures.

2.3 Conductivity of Graphene

The surface conductivity of graphene governs its electromagnetic response and can be derived from the Kubo formalism. The general expression, valid across a wide frequency range, is given by [26, 89, 101, 102]:

$$\sigma(\omega) = -\frac{ie^2(\omega + i\tau^{-1})}{\pi\hbar^2}\left[\frac{1}{(\omega + i\tau^{-1})^2}\int_0^\infty \left(\frac{\partial f_d(E)}{\partial E} - \frac{\partial f_d(-E)}{\partial E}\right) E\, dE \right. \\ \left. - \int_0^\infty \frac{f_d(-E) - f_d(E)}{(\omega + i\tau^{-1})^2 - 4(E/\hbar)^2}\, dE\right] \tag{2.17}$$

where $f_d(E) = \left(e^{(E-\mu_c)/(k_B T)} + 1\right)^{-1}$ is the Fermi–Dirac distribution, μ_c is the chemical potential, k_B is Boltzmann's constant, T is the temperature, $\hbar$ is the reduced Planck constant, ω is the angular frequency, and τ is the carrier relaxation time.

The total conductivity consists of two distinct contributions: intraband and interband.

2.3.1 Intraband Conductivity

The intraband term arises from electronic transitions near the Fermi level. It can be evaluated analytically, yielding:

$$\sigma_{\text{intra}}(\omega) = \frac{2k_B T e^2}{\pi\hbar^2} \ln\left(2\cosh\left(\frac{\mu_c}{2k_B T}\right)\right) \frac{i}{\omega + i/\tau} \tag{2.18}$$

This expression accounts for finite temperature effects and is valid across a broad frequency range.

2.3.2 Interband Conductivity

The interband term corresponds to electron transitions between the valence and conduction bands. Under the assumption $T \to 0$ and $\hbar\omega \geq \mu_c$, it simplifies to:

$$\sigma_{\text{inter}}(\omega) = \frac{ie^2}{4\pi\hbar} \ln\left[\frac{2\mu_c + (\omega + i/\tau)\hbar}{2\mu_c - (\omega + i/\tau)\hbar}\right] \tag{2.19}$$

2.3.3 Total Conductivity

The total surface conductivity of graphene is the sum of the intraband and interband contributions:

$$\sigma_{\text{total}}(\omega) = \sigma_{\text{intra}}(\omega) + \sigma_{\text{inter}}(\omega) \tag{2.20}$$

2.3.4 Drude Model for Sub-THz Frequencies

In the sub-terahertz (sub-THz) and terahertz (THz) frequency regimes, the interband contribution becomes negligible because the photon energy $\hbar\omega$ is much smaller than the chemical potential μ_c for typical doping levels ($\mu_c > 0.1$ eV). Consequently, the total conductivity is dominated by the intraband term. Moreover, at room temperature and for $\mu_c \gg k_B T$, the logarithmic term in Eq. (2.18) simplifies, and the conductivity reduces to the well-known Drude-like expression:

$$\sigma_{\text{Drude}}(\omega) = \frac{ie^2\mu_c}{\pi\hbar^2(\omega + i\tau^{-1})} \tag{2.21}$$

This model captures the essential physics of graphene at sub-THz frequencies: a Drude-type response with a real part representing resistive losses and an imaginary part representing inductive reactance (negative imaginary part), which enables the propagation of tightly confined surface plasmon polaritons.

For all antenna simulations in this chapter, the Drude model (Eq. 2.21) is used, as the intraband contribution dominates and the interband contribution is negligible in the sub-THz regime.

2.4 Reconfigurability Mechanism: Analytical Model and Biasing Design

The reconfigurability of the proposed antenna is achieved by electrically controlling the surface conductivity of each graphene parasitic element. This section provides an analytical description, a practical biasing design, and an analysis of the voltage range required to tune the chemical potential.

2.4.1 Analytical Relationship Between Voltage and Chemical Potential

The graphene sheet is separated from a metal gate electrode by a thin dielectric layer (e.g., Al_2O_3, HfO_2, or the polyimide substrate itself). Applying a gate voltage V_g induces charge carriers in graphene, shifting its Fermi level (chemical potential) μ_c. The relationship follows a parallel-plate capacitor model:

$$n = \frac{\varepsilon_0\varepsilon_r}{e\,t_d}(V_g - V_{\text{CNP}}) \tag{2.22}$$

where n is the induced carrier density (m^{-2}), ε_0 is the vacuum permittivity, ε_r is the relative permittivity of the dielectric, t_d is the dielectric thickness (m), $e = 1.602 \times 10^{-19}$ C is the electron charge, and V_{CNP} is the charge neutrality point voltage (typically a few volts due to residual doping).

The Fermi level μ_c is related to n by:

$$\mu_c = \hbar v_F \sqrt{\pi n} \tag{2.23}$$

Combining Eqs. (2.22) and (2.23):

$$\mu_c = \hbar v_F \sqrt{\frac{\pi \varepsilon_0 \varepsilon_r}{e\, t_d} (V_g - V_{\mathrm{CNP}})} \tag{2.24}$$

This equation shows that $\mu_c \propto \sqrt{V_g}$ for $V_g > V_{\mathrm{CNP}}$.

2.4.2 Practical Biasing Design

A convenient approach for our topology is the coplanar side-gate scheme [71, 103], which uses thin electrodes placed around the graphene element. As demonstrated in [104], a side-gating scheme can induce a chemical potential of about 0.9 eV with a gate voltage of about 2–3 V. A typical implementation consists of:

The practical biasing design consists of the following components:

a) Graphene parasitic element: Patterned on the polyimide substrate.

b) Dielectric layer: A thin layer (e.g., 10–20 nm of Al_2O_3, HfO_2, or SiO_2) deposited between the graphene and the gate electrode.

c) Metal gate electrode: Made of Au or Ti/Au, placed underneath the dielectric and connected to a DC bias line.

d) Electrical contacts: These are not strictly needed for parasitic elements (they are capacitively coupled), but a common back-gate can be used to bias all elements simultaneously or independently via patterned gates.

For independent control of the eight parasitic sectors, each sector is equipped with its own gate electrode. A ground plane is placed below all gates to complete the capacitor structure. The biasing voltage is applied through high-resistance DC feed lines that do not interfere with the RF performance.

2.4.3 Voltage Range and Chemical Potential Achievable

Typical experimental values for CVD graphene on Al_2O_3 or h-BN dielectrics are:

From Eq. (2.24) and the table: For a 10 nm Al_2O_3 dielectric ($\varepsilon_r \approx 7$), a modest voltage of 5–10 V yields $\mu_c \approx$ 0.4–0.56 eV, which is experimentally feasible and provides strong conductivity modulation.

The maximum experimentally reported μ_c for graphene is approximately 0.6–0.9 eV (depending on the gating scheme) [105]. In this work, $\mu_c = 1$ eV is chosen for the ON state in simulations as it represents a suitable compromise, ensuring sufficiently high graphene conductivity for efficient radiation while remaining within

Table 2.1: Relationship between gate voltage and Fermi level for a typical dielectric ($\varepsilon_r = 7$, $t_d = 10$ nm)

$V_g - V_{\text{CNP}}$ (V)	Carrier density n (m^{-2})	μ_c (eV)
1	4.8×10^{16}	0.18
2	9.6×10^{16}	0.25
5	2.4×10^{17}	0.40
10	4.8×10^{17}	0.56
20	9.6×10^{17}	0.79
30	1.44×10^{18}	0.97

a practically achievable range for applied bias voltages. The OFF state is achieved at $V_g = V_{\text{CNP}}$ (typically 0–3 V), where $\mu_c \approx 0$ eV and conductivity is minimal.

Thus, the required bias voltages for this work are in the range of 0-15 V, which is practical for integration with CMOS control circuits.

2.4.4 Impact on Conductivity and Antenna Performance

The gate voltage modulates the intraband conductivity (Eq. 2.21) through μ_c. For $\mu_c = 0$ eV (OFF), the conductivity is near the minimum value $\sigma_{\text{min}} \approx \sigma_0 = e^2/(4\hbar) \approx 60$ μS (but often higher due to residual doping). For $\mu_c = 0.5$ eV (ON), the conductivity increases significantly, enabling strong electromagnetic coupling with the driven dipole. This change effectively switches the parasitic element between a "reflector-like" (OFF) and "director-like" (ON) state, allowing programmable beam steering.

In simulations, we use $\mu_c = 0$ eV and 1 eV to clearly demonstrate the switching concept. For experimental realization, $\mu_c = 0$ eV (or near-zero) and $\mu_c = 0.5$ eV would be used, with corresponding gate voltages of approximately 0 V and 5–10 V, respectively.

In graphene antennas, reconfigurability is achieved by tuning the chemical potential μ_c via electrostatic biasing or chemical doping, which in turn enables pattern reconfiguration of parasitic elements. Note: In this thesis, μ_c and Fermi level are used interchangeably, as their difference is negligible at room temperature when $\mu_c \gg k_B T$.

By applying a positive voltage bias, the chemical potential μ_c increases (positive values, electron doping), which increases the conductivity and enables the parasitic elements to couple electromagnetically with the driven dipole – this corresponds to the ON state. Negative μ_c values (hole doping) produce the same conductivity magnitude due to the symmetry of the Kubo formula; therefore, a negative bias can also be used to achieve the ON state. In this work, we focus on positive μ_c for simplicity.

2.4.5 Implementation of Coding Patterns

Each of the eight fan-shaped parasitic sectors is equipped with an independent gate electrode (see the practical biasing design above). To switch a sector ON, a positive gate voltage $V_g > V_{\mathrm{CNP}}$ is applied, raising its chemical potential to $\mu_c \approx 0.5$–1 eV and making it highly conductive. To switch it OFF, the gate is set to $V_g = V_{\mathrm{CNP}}$ (typically 0–3 V), keeping $\mu_c \approx 0$ eV so the sector remains nearly transparent.

For example, the coding pattern V2468 means: excite the vertical dipole (V) and apply the ON-state bias voltage to parasitic sectors 2, 4, 6, and 8 while keeping sectors 1,3,5,7 at the OFF bias. This is achieved by independently controlling the eight gate lines using a digital controller (e.g., an FPGA). The same principle applies to any coding pattern: the letter (V or H) selects which dipole is fed, and the numbers indicate which sectors receive the ON bias.

2.5 Why Yagi-Uda Architecture

The proposed antenna adopts a Yagi-Uda-inspired configuration consisting of a driven dipoles and multiple parasitic elements. This section explains the reasons for choosing this architecture and provides essential details of its operation.

2.5.1 Advantages of Yagi-Uda in Sub-THz Regime

The Yagi-Uda design was selected for the following reasons:

a) High directivity and gain: A conventional Yagi-Uda antenna achieves moderate to high gain using only a single active element and several passive directors/reflectors. At sub-THz frequencies, where amplifier power is limited, passive gain enhancement is highly beneficial.

b) Reconfigurability via parasitic elements: By controlling the conductivity of each parasitic element (ON/OFF states), we can dynamically change the radiation pattern without modifying the driven element. This enables electronic beam steering across 360°.

c) Simplicity and low loss: Unlike phased arrays that require complex feeding networks and multiple active elements (introducing losses at sub-THz), the Yagi-Uda approach uses only one driven dipole. This minimizes conductor and dielectric losses.

d) Compatibility with graphene: Graphene's tunable conductivity is ideal for switching parasitic elements between reflective (OFF, low conductivity) and directive (ON, high conductivity) states. The plasmonic field confinement in graphene also allows compact element spacing.

e) Transparency: The Yagi-Uda structure can be made entirely of graphene on a transparent substrate (polyimide), preserving optical transparency, a key requirement for future smart surfaces and windows.

In a conventional metallic Yagi-Uda design, the lengths and spacings are fixed, so the beam direction is fixed. In our graphene-based design, each parasitic element can be electronically switched between a reflecting state (OFF, $\mu_c \approx 0$) and a directing state (ON, $\mu_c > 0$). By selectively activating certain parasitic sectors, we can create an equivalent Yagi-Uda array pointing in any desired direction along the azimuthal plane. This programmable behavior allows 360° beam steering without any mechanical movement.

2.6 Design Considerations for Sub-THz Operation

At the target frequency of 200 GHz (free-space wavelength $\lambda_0 \approx 1.5$ mm), the effective wavelength in graphene is significantly shorter due to plasmonic slowing. Therefore, the physical dimensions of the elements are much smaller than $\lambda_0/2$, enabling a compact form factor (overall diameter ≈ 1.36 mm). The mutual coupling distances ($R_i = 240\,\mu\text{m}$, $R_o = 610\,\mu\text{m}$) are carefully chosen to ensure that the parasitic elements lie within the reactive near-field region ($r < \lambda/2\pi \approx 240\,\mu\text{m}$ for strong coupling) while maintaining stable impedance matching.

In summary, the Yagi-Uda architecture combined with graphene's tunable conductivity provides an optimal balance of gain, reconfigurability, compactness, and transparency, making it the preferred choice for this thesis.

2.7 Graphene Antenna Design

The approach for the proposed graphene dipole antenna follows a threefold design strategy aimed at obtaining transparency, reconfiguring conductivity, and dynamic beam control within a compact sub-THz structure. First, transparency is realized by employing graphene as a radiating element and polyimide as a substrate, minimizing obstruction while maintaining electromagnetic performance. Second, the surface conductivity of parasitic elements is reconfigured by modulating the chemical potential of graphene. Third, pattern reconfigurability is enabled by the symmetric arrangement of parasitic elements around the orthogonal dipole. These three design strategies ensure that the antenna can operate efficiently at 200 GHz while maintaining structural simplicity and functional adaptivity.

As shown in Figure 2.9, the proposed antenna is conceived as a planar, disc-shaped structure designed to preserve perfect geometrical symmetry, which is essential for achieving predictable, uniform, and stable radiation characteristics across all operating states. The overall design approach is based on three core pillars: transparency, reconfigurability, and beam control. Each of these principles contributes to the antenna's ability to operate efficiently in the sub-terahertz (sub-THz) frequency range while maintaining structural simplicity and functional adaptivity. Transparency is achieved through the exclusive use of a polyimide substrate combined with graphene as the only conductive material. This combination ensures that the antenna remains highly transparent in the visible spectrum (with over 99.4% transmittance) while exhibiting tunable electronic and electromagnetic properties in the THz regime. Specifically, the surface conductivity and complex permittivity of graphene can be dynamically controlled by adjusting its chemical potential via an applied bias voltage. The polyimide substrate serves as both a mechanical support and dielectric medium. Polyimide was selected after careful consideration of its electrical, mechanical, and optical characteristics, $\varepsilon_r = 3.5$, offers an excellent trade-off between field confinement and surface wave suppression. A higher dielectric constant would increase near-field confinement but could lead to undesired substrate modes, while a lower ε_r would reduce the antenna's effective size and coupling. The loss tangent $\tan\delta$ of 0.0027 ensures that dielectric losses remain minimal even at sub-THz frequencies, where both conductor and dielectric losses

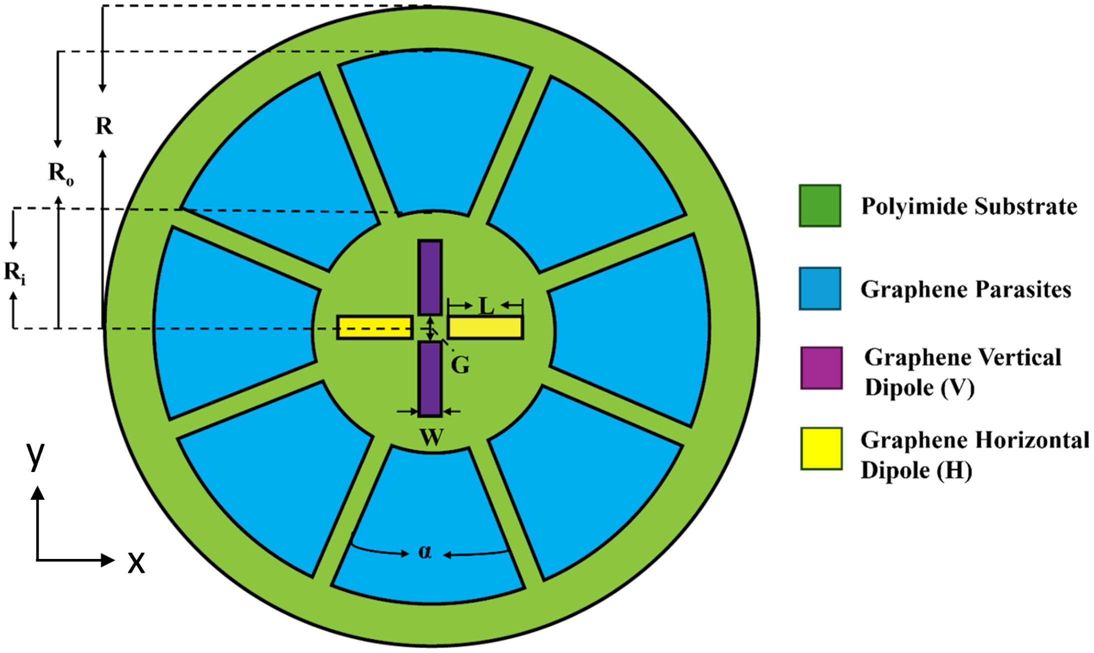

Figure 2.9: Schematic top view of the proposed graphene-based programmable dual-dipole antenna. The structure consists of two orthogonal center-fed graphene dipoles surrounded by eight fan-shaped graphene parasitic sectors, all on a circular polyimide substrate (green). Key dimensions: dipole arm length L = 155 μm, width W = 27 μm, feed gap G = 25 μm; substrate thickness T = 150 μm, substrate radius R = 680 μm; parasitic inner radius $R_i = 240$ μm, outer radius $R_o = 610$ μm, angular width $\alpha = 40°$. The Cartesian coordinate axes (x, y) are shown for reference. Each parasitic sector can be independently biased (ON/OFF) by tuning its chemical potential.

tend to dominate [106].

Alternative substrate materials for sub-THz antennas were also evaluated, including liquid crystal polymer (LCP) [107], benzocyclobutene (BCB) [108], high-resistivity silicon (HR-Si) [109], and fused silica (quartz) [110]. While LCP and BCB offer slightly lower dielectric loss, they are less transparent in the visible spectrum and require more complex fabrication. Rigid substrates such as HR-Si and quartz provide excellent dimensional stability but lack mechanical flexibility and optical transparency (>90% transmittance only in thin layers). Polyimide is preferred because it uniquely combines high optical transparency (>99%), mechanical flexibility, low dielectric loss ($\tan\delta \approx 0.0027$), good thermal stability (up to 300°C), and ease of integration with large-area CVD graphene transfer processes [109, 110]. These attributes are essential for the targeted applications in smart windows, flexible electronics, and transparent 6G communication surfaces.

The substrate thickness (T_s) was optimized to 150 μm to simultaneously ensure mechanical robustness, ease of fabrication, and impedance matching over the desired bandwidth. Furthermore, the substrate exhibits a breakdown voltage exceeding 500 V/μm, allowing it to withstand voltages over 75 kV across its thickness.

To estimate the required biasing voltage, a typical gate configuration employing a 10 nm Al_2O_3 dielectric layer with a relative permittivity of $\varepsilon_r = 7$ is considered. Using the relation

$$\mu_c = \hbar v_F \sqrt{\frac{\pi \varepsilon_0 \varepsilon_r (V_g - V_{\text{CNP}})}{e t_d}} \tag{2.25}$$

a chemical potential of $\mu_c = 0.5$ eV, corresponding to an experimentally achievable ON-state condition, requires a gate voltage of approximately $V_g - V_{\text{CNP}} \approx 5.6$ V. Similarly, for the theoretical upper limit of $\mu_c = 1$ eV, the required biasing voltage increases to approximately 22.4 V. These voltages remain several orders of magnitude lower than the dielectric breakdown voltage of 75 kV, thereby ensuring stable and reliable electrical operation during the reconfiguration process.

2.7.1 Driven Elements and Parametric Analysis

At the center of the substrate are two orthogonal, center-fed graphene dipoles, forming the primary radiating structure. These dipoles are oriented along x- and y-axis, respectively, to achieve dual linear polarization. The intersection at the geometric center ensures symmetry and enables independent or combined excitation. Each dipole was initially designed with a total length corresponding to half of the free-space wavelength $\lambda/2$, following the classical resonance condition for metallic dipoles. However, this relation doesn't directly hold for graphene-based antennas at sub-THz frequencies due to the plasmonic nature of graphene, which supports highly confined surface plasmon polaritons (SPPs). The effective plasmonic wavelength (λ_{plasma}) is much smaller than λ_0, causing a shift in the resonance. Therefore, the dipole length was parametrically optimized through full-wave simulations to precisely match the desired resonance in the sub-THz regime, as shown in Figure 2.10.

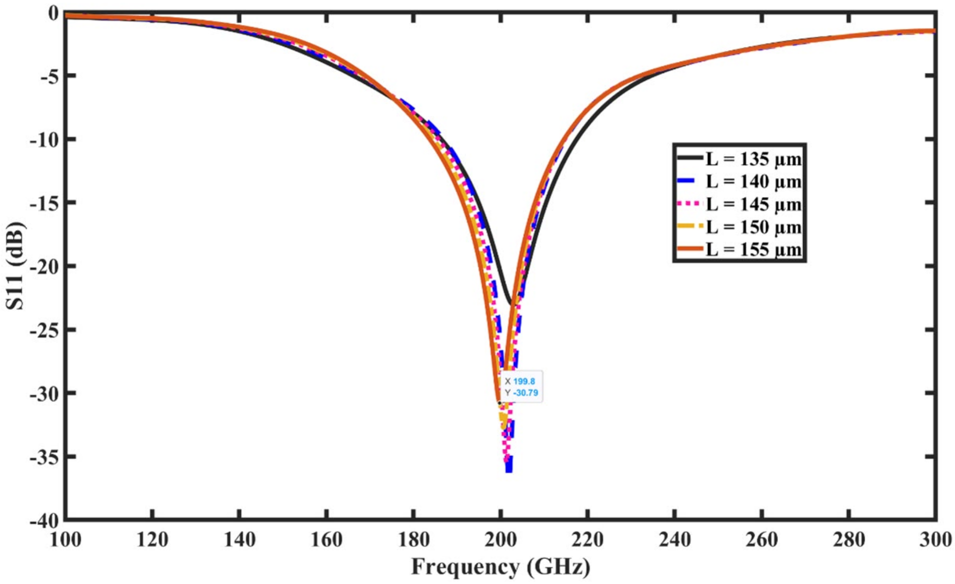

Figure 2.10: S11 as a function of frequency by varying the length from 135-155 µm to achieve optimal performance

2.7.2 Parasitic Elements and their Optimization

Eight parasitic elements are uniformly distributed around the graphene orthogonal dipoles, surrounding the antenna circumference. These parasitic elements are concentrically arranged to maintain the antenna's rotational symmetry while providing directional control and frequency tunability. Each parasitic element can be electrically activated or deactivated by adjusting its graphene Fermi level through applied bias voltage.

2.7.3 Systematic Parametric Analysis Overview

To systematically evaluate the antenna performance, the following geometric parameters were analyzed. For each sweep, all other parameters were kept at their optimized default values (see Table 2.2). The sweep ranges and step sizes are summarized in Table 2.3.

Table 2.2: Default fixed parameters used during parametric sweeps

Parameter	**Description**	**Default value**
L	Dipole arm length	155 μm
W	Dipole arm width	27 μm
G	Dipole feed gap	25 μm
T_s	Substrate thickness	150 μm
R_i	Parasitic inner radius	240 μm
R_o	Parasitic outer radius	610 μm
α	Parasitic angular width	40°
μ_c^{ON}	Chemical potential (ON state)	1 eV
μ_c^{OFF}	Chemical potential (OFF state)	0 eV

Table 2.3: Swept parameters and their ranges

Swept parameter	**Range**	**Step size**
Dipole length L	135 – 155 μm	5 μm
Angular width α	10° – 60°	10°
Inner radius R_i	220 – 260 μm	10 μm
Outer radius R_o	600 – 680 μm	10 μm

A critical aspect of the antenna development process involved parametric optimization of key geometric parameters to achieve optimal impedance, stable resonance behavior, and efficient coupling between the driven and parasitic elements. Since the antenna performance at sub-terahertz frequencies is highly sensitive to small dimensional variations, each structural parameter was carefully studied through full-wave electromagnetic simulations. The optimization focused primarily on the angular width of the parasitic element (α), the inner and outer radii R_i and R_o of the parasitic ring, and the key physical dimensions of the dipole.

2.7.4 Effect of Parasitic Angular Width α

The angular width α of each parasitic element defines the portion of the circular ring occupied by conductive graphene and therefore directly influences the electromagnetic coupling between the parasitic elements and the central dipole. To quantify this effect, α was swept from 10° to 60°, and the corresponding input reflection coefficient (S_{11}) was analyzed as shown in Figure 2.11. The results indicate that α has a pronounced impact on impedance matching, particularly on the depth and sharpness of the S_{11} resonance. When α is too small (below 20°), the parasitic elements occupy a limited angular area, leading to weak electromagnetic coupling and reduced ability to modify the near-field distribution around the dipole. Consequently, the return loss degrades, and the antenna exhibits poor matching. Conversely, for very wide sectors (above 50°), excessive coupling occurs, introducing

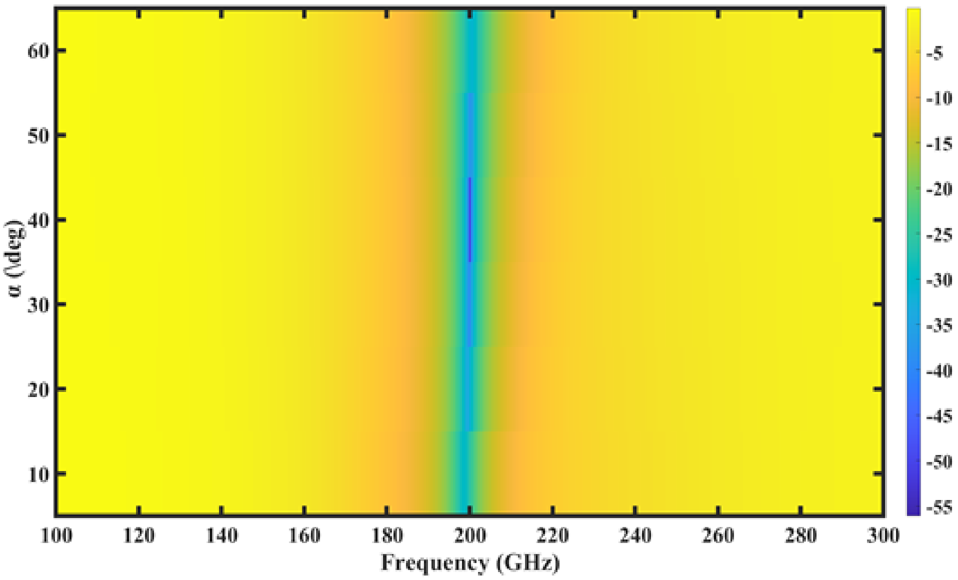

Figure 2.11: Color map representation of S_{11} as a function of frequency and angular width α of the parasitic element. Sweep range: 10° to 60°; other parameters fixed at default values (Table 2.2).

mutual interference between adjacent parasitic segments and leading to detuning effects.

An optimal condition was found at $\alpha = 40°$, where the parasitic elements attain the ideal electrical length and coupling strength relative to the central dipole. Figure 2.12 presents the S_{11} spectra for all swept α values, with the $\alpha = 40°$ curve highlighted. At this configuration, the antenna achieves the deepest S_{11} at the target operating frequency of 200 GHz, confirming strong resonance and efficient impedance matching. The resonant frequency remained stable, shifting only slightly between 198 GHz and 200 GHz across the sweep. This small shift is caused by the changing reactive loading on the driven dipole as it α varies: a larger α increases the effective capacitance and inductance coupled from the parasitic sectors, slightly lowering the resonant frequency. Conversely, a smaller α reduces this loading, raising the frequency. The effect is minor because the driven dipole primarily determines the resonance, while the parasitic angular width fine-tunes the coupling strength.

2.7.5 Effect of Inner Radius R_i

The radial positioning of the parasitic elements plays a pivotal role in defining the strength and phase of mutual coupling with the driven dipoles. The inner radius R_i determines how close the parasitic elements are placed relative to the radiating

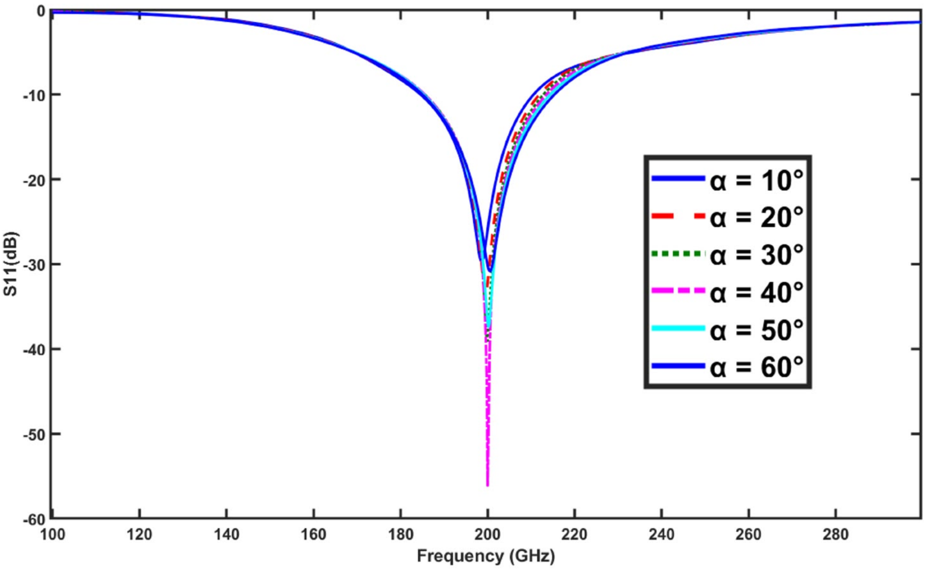

Figure 2.12: Simulated S_{11} (dB) as a function of frequency for the optimal parasitic angular width $\alpha = 40°$. The minimum S_{11} is -57 dB at 200 GHz, and the -10 dB bandwidth spans 187–214 GHz

dipoles, while the outer radius R_o controls the overall electrical aperture of the antenna. Physically, the coupling between the driven dipole and parasitic elements is governed by the distance relative to the operating wavelength. At the sub-THz frequencies, the reactive near-field region extends approximately to $\lambda/2\pi \approx 240\,\mu$m at 200 GHz, making precise radial positioning critical for controlling whether the interaction is reactive or radiative.

A parametric sweep of R_i from 220 μm to 260 μm was conducted, as illustrated in Figure 2.13. When R_i is too small (200 μm), the parasitic elements lie very close to the dipole, causing strong reactive coupling that heavily detunes the resonant frequency and disrupts impedance matching. This over-coupling leads to energy storage in the near field rather than efficient radiation. This behavior occurs because the parasitic elements reside within the reactive near-field region ($r < \lambda/2\pi$), where the electromagnetic fields are predominantly non-radiating and store reactive energy. In the sub-THz regime, each parasitic element acts as an additional reactive load that alters the input impedance of the driven dipole, effectively shifting the resonant frequency and reducing radiation efficiency.

Conversely, as R_i increases beyond approximately 255 µm, the coupling gradually weakens. At $R_i = 260$ µm, the S_{11} response becomes nearly indistinguishable from that of a dipole without parasitic elements (all-OFF state), indicating that the parasitic elements no longer significantly contribute to beam steering. However, the transition is gradual rather than abrupt; therefore, the optimal value

$R_i = 240$ µm was selected as it provides a balanced coupling strength sufficient for reconfigurability while preserving stable resonance. At such distances, the mutual coupling between the dipole and parasitic elements decays as $1/r^3$ in the near-field region, causing the induced currents on the parasitic elements to become negligible. Consequently, the parasitic elements become electromagnetically invisible to the driven dipole, rendering them ineffective for beam steering. The optimal value was determined to be $R_i = 240\,\mu$m, which achieves a balanced coupling strength, sufficient to influence the near field distribution while preserving stable resonance and impedance performance. At this spacing, the antenna maintains its designed resonance around 190–200 GHz with consistent return loss characteristics.

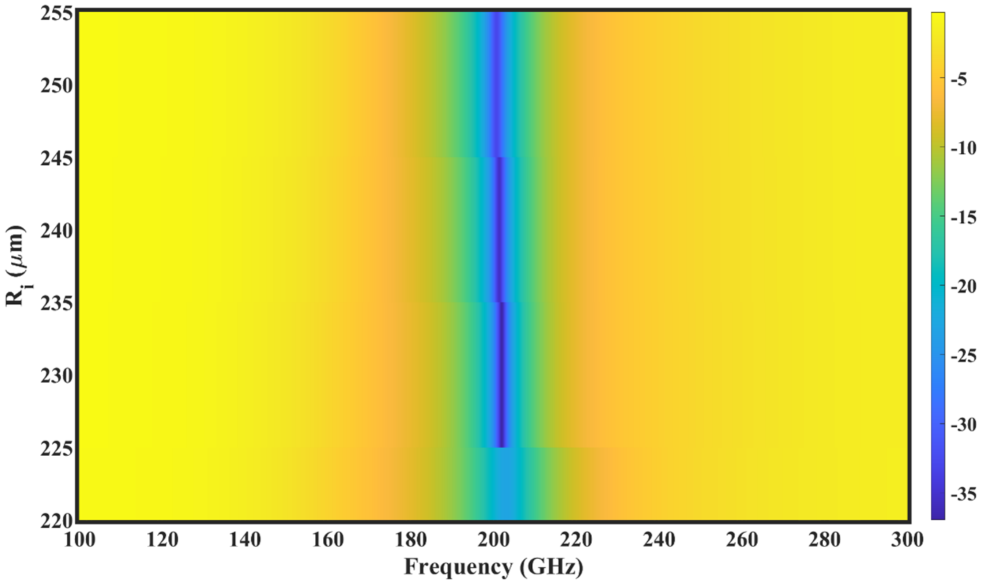

Figure 2.13: Color map representation of S_{11} as a function of frequency and inner radius R_i of the parasitic element. Sweep range: 220–260 μm; other parameters fixed at default values (Table 2.2).

2.7.6 Effect of Outer Radius R_o

Similarly, the outer radius R_o was varied between 600 μm and 680 μm to study its effect on the overall electromagnetic behavior, as shown in Figure 2.14. Increasing R_o effectively enlarges the electrical aperture of the structure, extending the radiation surface and altering the phase distribution of surface currents. For smaller R_o values, the parasitic elements are confined too close to the center, reducing the beam directivity and narrowing beamwidth.

Between approximately 605 μm and 635 μm, a pronounced degradation in impedance matching (higher S_{11}) is observed. This occurs because the electrical

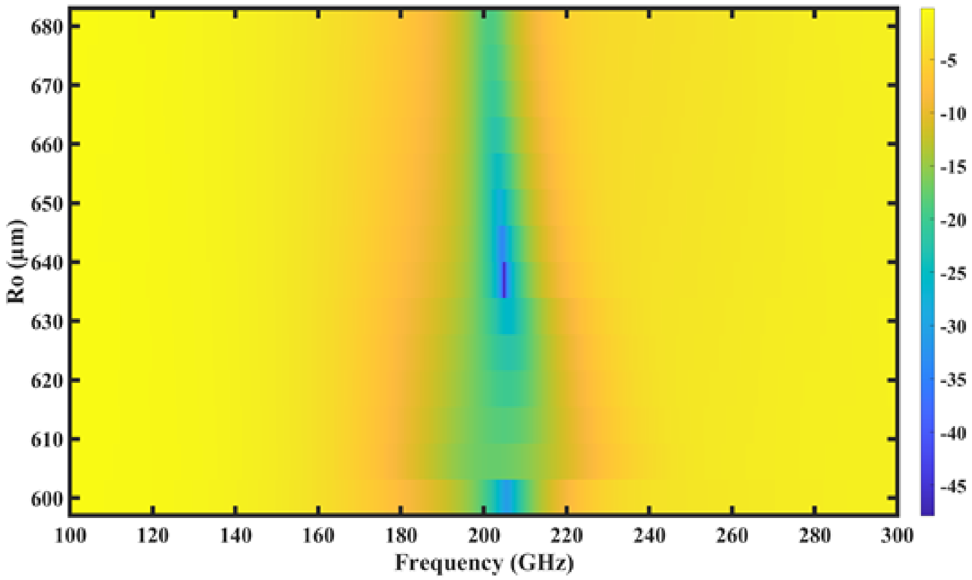

Figure 2.14: Color map representation of S_{11} as a function of frequency and outer radius R_o of the parasitic element. Sweep range: 600–680 μm; other parameters fixed at default values (Table 2.2).

distance from the driven dipole to the parasitic ring causes a partial phase reversal of the coupled fields. In this range, the induced currents on the parasitic elements interfere destructively with the direct radiation, effectively increasing the reflected power at the feed. Once R_o exceeds 635 μm, the coupling becomes sufficiently weak that the parasitic elements no longer significantly affect the input impedance, and matching improves again.

The results revealed that $R_o = 610\,\mu$m provides the most favorable trade-off between impedance matching and radiation performance. At this configuration, the antenna exhibits excellent S_{11} performance (less than -36 dB) and precise resonance at 200 GHz, aligning perfectly with the target design frequency. Increasing R_o beyond this value offers no significant improvement and may introduce spurious coupling effects between adjacent parasites.

2.7.7 Summary of Parametric Effects

The parametric analysis indicates several trade-offs: R_i balances coupling strength against impedance stability and R_o trades off electrical aperture against isolation between parasitic elements. The angular width α balances beam control against mutual coupling. Substrate thickness T trades off mechanical robustness against dielectric loss. Feed gap G balances impedance matching against fabrication tolerance.

These trade-offs collectively define the optimized parameters in Table 2.4.

Table 2.4: Optimized parameters of the proposed graphene-based dipole antenna

Parameter	**Description**	**Optimized Value**
L	Dipole arm length	155 μm
W	Dipole arm width	27 μm
G	Dipole feed gap	25 μm
T	Substrate thickness	150 μm
R	Substrate radius	680 μm
R_i	Parasitic inner radius	240 μm
R_o	Parasitic outer radius	610 μm
α	Parasitic angular width	40°

The parametric optimization was performed sequentially (evolutionary) rather than in parallel. Initially, the driven dipole dimensions (L, W, G) were optimized with all parasitic elements in the OFF state. Subsequently, the parasitic sector geometry (α, R_i, R_o) was optimized one parameter at a time while keeping all other parameters at their current best values. For each sweep, the parameter of interest was varied over a predefined range, and all other geometric parameters were fixed at the previously optimized values (see Table 2.2). This sequential approach ensures that the effect of each parameter can be isolated and understood independently.

2.8 Effects of Relaxation Time and Temperature

Relaxation time strongly influences the impedance matching and resonance depth of the antenna, as observed from the S_{11} characteristics, shown in Figure 2.15. As τ increases from 0.5 ps to 1.4 ps, the resonance dip becomes significantly deeper, reaching nearly -30 dB around 200 GHz. This behavior highlights improved conductivity and reduced carrier scattering losses, which enhance plasmonic confinement and coupling efficiency. Consequently, higher τ values result in better impedance matching and stronger resonance behavior, whereas lower τ values produce weaker resonance and higher reflection losses. Furthermore, it is explicitly observed that increasing the temperature from 273 K to 330 K does not produce any noticeable change in the S_{11} characteristics, demonstrating that the proposed antenna maintains stable impedance matching and resonance behavior over the considered temperature range.

Importantly, as shown in Figure 2.16, the impedance matching remains stable across different reconfigurable coding states of the parasitic elements. Although slight shifts in the resonance frequency (from 196 GHz to 203 GHz) occur due to variations in the effective electrical length, the antenna consistently maintains its wide -10 dB bandwidth. This behavior confirms the robustness of the design, ensuring that the reconfiguration for beam steering or frequency tuning does not compromise matching or efficiency.

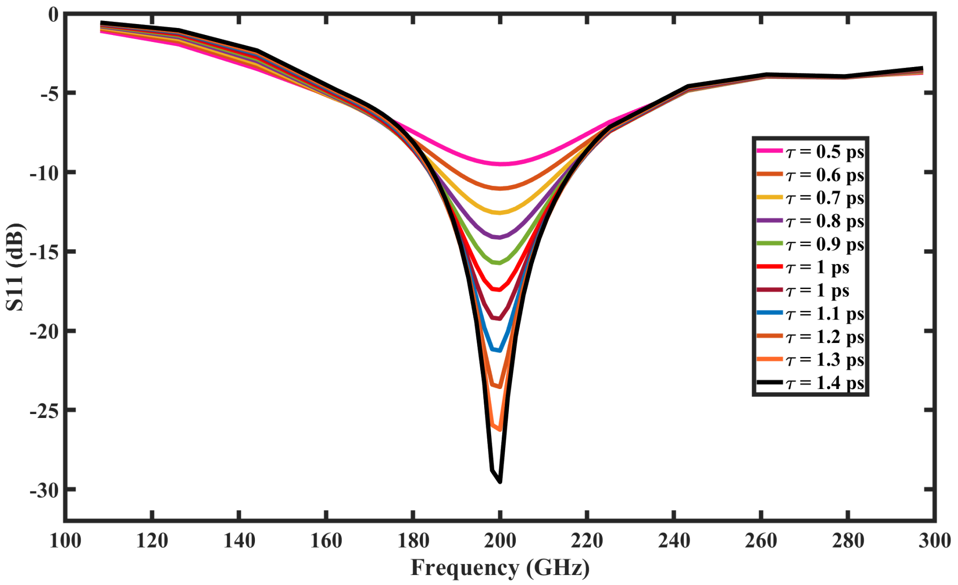

Figure 2.15: Simulated S_{11} (dB) as a function of frequency for different relaxation times τ (0.5–1.4 ps). As τ increases, the resonance dip becomes deeper (reaching nearly -30 dB at 200 GHz) due to reduced carrier scattering and enhanced conductivity, leading to improved impedance matching.

The overall design philosophy of the proposed antenna is centered on three synergistic attributes: Transparency, reconfigurability, and beam control. The transparency of the structure is achieved through the intrinsic optical properties of both graphene and polyimide, which together ensure more than 99% transmittance in the visible spectrum without degrading the antenna's electrical performance in the sub-THz regime. Reconfigurability is realized by exploiting the tunable surface conductivity of graphene, which can be precisely adjusted through electrostatic gating. By varying the applied bias voltage, the Fermi level of graphene changes, enabling dynamic control over the resonance frequency, impedance, and radiation characteristics of the antenna. Beam control, on the other hand, is accomplished through electromagnetic coupling between the active radiating dipoles and the surrounding parasitic elements. Selectively activating or deactivating these parasitic components modifies the phase distribution of the radiated fields, allowing the antenna to steer its main beam or reshape its radiation pattern electronically without any mechanical movement. Together, these features make the proposed design a highly versatile and adaptive platform suitable for next-generation transparent, tunable, and beam-steerable sub-THz communication systems.

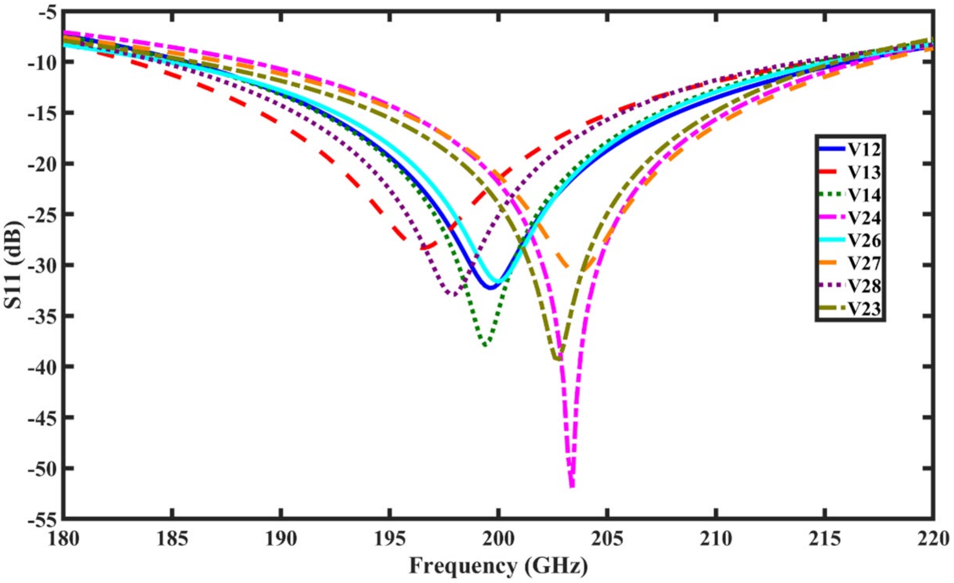

Figure 2.16: S_{11} for eight different coding patterns

2.8.1 Surface Current Distribution

To gain deeper insight into the radiation mechanism and the role of programmable parasitic elements, a detailed analysis of the surface current distribution was conducted. This study provides a direct visualization of how the excitation of specific graphene regions, either the driven dipoles or the parasitic elements, governs the formation and steering of the far field radiation pattern. The simulations were carried out at the resonant frequency of 200 GHz, under different biasing and coding configurations of the parasitic elements. The corresponding results are illustrated in Figure 2.17, which presents the surface current magnitude maps for two representative cases.

In Figure 2.17a, the horizontal (H) graphene dipole is actively excited, while the vertical (V) dipole remains unexcited, thus serving as a passive element. The parasitic array is programmed according to the H37 coding pattern, which parasitic elements 3 and 7 are switched to the On-state with a chemical potential ($\mu_c = 1\,\text{eV}$), while all other parasitic elements remain in the OFF-state ($\mu_c = 0\,\text{eV}$).

The simulated surface current distribution reveals that the driven H-dipole supports strong oscillating currents along its length, concentrated near the feed gap, where charge accumulation occurs due to the alternating electric field. Simultaneously, the On-state parasitic sectors (3 and 7) exhibit intense induced current densities, indicating strong electromagnetic coupling with the driven dipole. These elements effectively act as secondary radiators, re-radiating the coupled energy in a specific direction determined by their spatial placement and phase relationship with the driven dipole currents.

In contrast, the OFF-state parasitic elements appear almost current-free in the plot (dark blue region), confirming that the low surface conductivity of graphene at $\mu_c = 0\,\text{eV}$ effectively isolates these regions electromagnetically. The overall surface current distribution, therefore, becomes asymmetric, with energy concentrated predominantly along the H-dipole axis and extended toward the active parasitic sectors 3 and 7. This asymmetric current distribution directly manifests as a directional radiation pattern, where the beam is tilted toward the side containing the activated parasites. The induced surface currents on these ON state elements constructively interfere with the fields radiated by the driven dipole, reinforcing radiation in their direction while slightly suppressing it elsewhere. This behavior is consistent with the Yagi-Uda antenna principle, where directors and refactors shape the radiation by controlled coupling. In this context, the programmable parasitic elements act as electronically tunable directors, enabling beam steering without any mechanical movement.

In the second configuration, all parasitic elements are switched to the OFF state ($\mu_c = 0\,\text{eV}$), effectively rendering them non-conductive at 200 GHz. Under these conditions, only the driven horizontal dipole carries substantial current. The current distribution along the dipole exhibits a typical standing-wave pattern, with current maxima near the feed and nulls at the ends, consistent with the behavior of a half-wave plasmonic dipole as shown in Figure 2.17b. The parasitic elements, having near-zero conductivity, do not support any significant induced currents. As a result, they appear completely dark blue in the surface current magnitude plot, indicating negligible electromagnetic interaction with the driven dipole. In this configuration, the antenna behaves as a simple dipole radiator, producing a broad, nearly symmetrical radiation pattern centered along the dipole axis. The absence

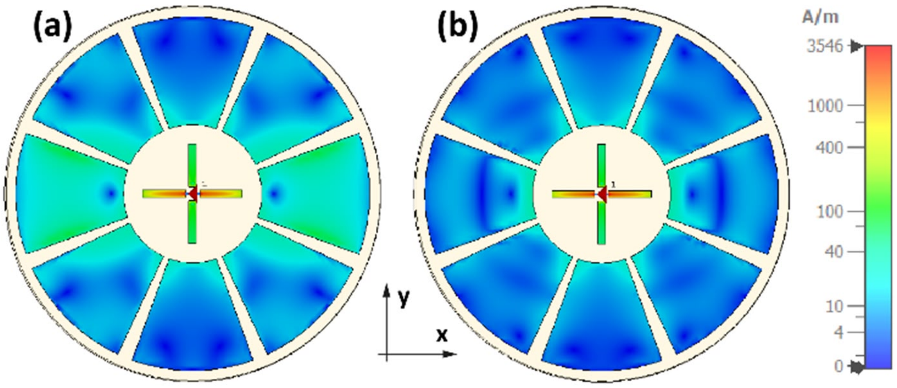

Figure 2.17: Surface current distribution at 200 GHz. (a) Coding pattern H37: horizontal dipole excited, parasitic sectors 3 and 7 are in the ON state (µc = 1 eV, high conductivity, bright yellow/red), while all other parasitic sectors (1,2,4,5,6,8) are in the OFF state (µc = 0 eV, low conductivity, dark blue). (b) All parasitic elements in the OFF state (µc = 0 eV); only the horizontal dipole is active. The color bar indicates current magnitude (A/m).

of significant parasitic coupling results in maximum radiation in the broadside direction and minimal beam distortion.

Comparing this state with H37 configuration clearly illustrates the programmable nature of the antenna. While the all-OFF state produces a symmetric and broad radiation pattern, the selective activation of specific parasitic elements (e.g., in H37) introduces controlled asymmetry in the surface current distribution, which in turn shapes and steers the radiation beam.

2.8.2 Physical Interpretation and Design Implications

The surface current analysis validates the electromagnetic coupling mechanism underlying the antenna's reconfigurability. When a parasitic element transitions from the OFF state ($\mu_c = 0$ eV) to the ON state ($\mu_c = 1$ eV), its surface conductivity (σ_g) increases by several orders of magnitude. This change transforms the element from a nearly transparent region into an effective plasmonic resonator capable of sustaining induced currents. The relative phase and amplitude of these induced currents with respect to the driven dipole determine whether a given parasitic element behaves as a director (in-phase coupling, forward radiation enhancement) or a reflector (out-of-phase coupling, backward radiation enhancement).

In conventional Yagi-Uda theory, a parasitic element acts as a director when its induced current lags the driven element current by less than 90° (approximately in-phase), and as a reflector when the lag exceeds 90° (out-of-phase). In our design, the transition from OFF to ON state changes the complex conductivity of graphene, which shifts the phase of the induced current. This phase shift is governed by the Drude model (Eq. 2.21) and the reactive near-field coupling distance, enabling electronic switching between director and reflector modes.

Thus, by selectively controlling which parasitic elements are activated, the designer can dynamically tailor the current distribution across the antenna surface, leading to precise control over the radiation pattern. This capability forms the foundation for the antenna's programmable beam steering features, which are further elaborated in the section on radiation characteristics.

2.9 Realized Gain and Efficiency Analysis

The performance of any radiating structure can be fully characterized not only by its impedance matching and current distribution but also by its ability to efficiently direct radiated power toward desired spatial directions. For the proposed graphene-based programmable dual-dipole antenna, this capability is quantified through two key metrics: the realized gain and total radiation efficiency. These parameters jointly describe how effectively the antenna transforms input power into useful radiated energy, considering both intrinsic material losses and impedance mismatch effects.

The radiated gain (G_r) represents the product of the antenna's directivity (D) and radiation efficiency (η_{rad}), while also incorporating losses due to impedance mismatch. It is expressed as [111]:

$$G_r = D \times \eta_{\text{rad}} \times \left(1 - |\Gamma|^2\right) \tag{2.26}$$

where Γ is the reflection coefficient at the feed port.

In simpler terms, the realized gain measures how much of the input power is effectively radiated in each direction after accounting for both mismatch and material losses. Figure 2.18 illustrates the simulated realized gain for several representative two-ON-state coding patterns across the operating frequency band (187-214 GHz). Within this band, the antenna demonstrates a maximum realized gain ranging from approximately -2.3 dBi to 2.3 dBi, depending on the specific coding pattern applied to the parasitic elements. This variation is inconsistent with expectations for a sub-THz antenna employing graphene, a material that offers tunability and exhibits higher intrinsic surface resistance than metals. The observed values are therefore quite promising, particularly considering the antenna's compact, transparent, and reconfigurable nature.

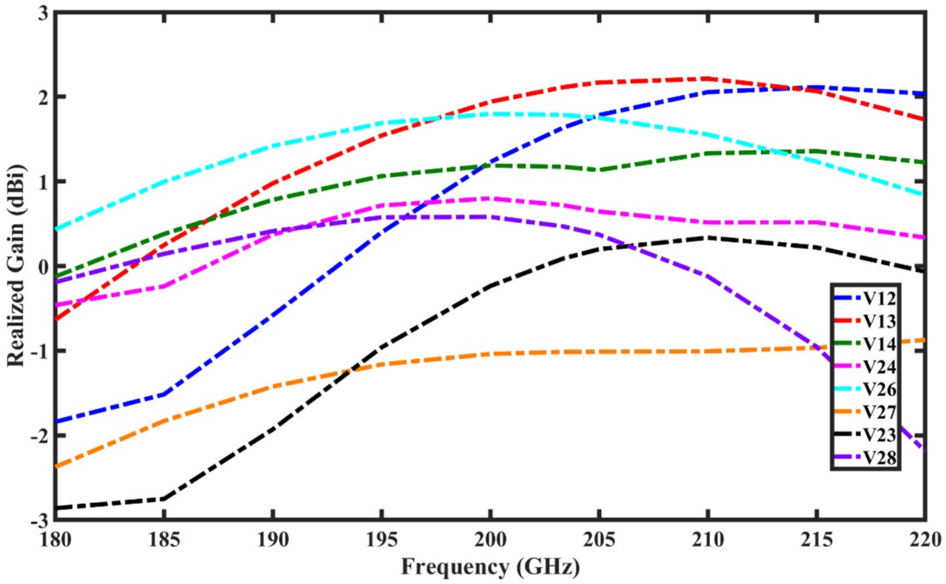

Figure 2.18: Realized gain of the proposed antenna for eight different coding patterns

A closer inspection of the results reveals that the realized gain remains remarkably stable across the frequency range. Between 190 GHz and 210 GHz, the gain variation for any given pattern does not exceed 0.4 dBi, which signifies a high degree of frequency stability and consistent radiation performance. This stability is primarily attributed to the optimized dipole geometry and balanced coupling achieved through the parametric design process, which maintains impedance integrity even when the parasitic elements are reconfigured.

The magnitude of realized gain is inherently dependent on the specific coding pattern applied to the parasitic elements (see Table IV and Fig. 2.18), as each configuration modifies the spatial distribution of surface currents and , consequently, the antenna's effective aperture. When the coding pattern creates a single dominant radiation mode, the antenna exhibits the highest realized gain, reaching approximately 2.0-2.3 dBi. This occurs because the radiated energy is concentrated into one primary direction, maximizing power density and directivity. In contrast, configurations that intentionally split the radiated energy into two or four beams, to achieve spatial diversity or multi-user coverage, naturally display lower peak gain per beam since the total radiated power is distributed across multiple directions. For example, dual beam configurations exhibit typical gain around 1.3 dBi, while quad-beam configurations show gain of approximately 0.7 dBi per beam. These results confirm that the antenna's programmable parasitic network effectively governs the radiation pattern shape, allowing a trade-off between beam multiplicity and directional control. Such behavior is characteristic of reconfigurable Yagi-Uda-type structures, where the number and arrangement of active elements control the radiation focusing and beam direction.

The total efficiency (η_t) of the antenna is defined as the ratio of the total radiated power (P_{rad}) to the input power (P_{in}) at the feed port:

$$\eta_t = \frac{P_{\text{rad}}}{P_{\text{in}}} \tag{2.27}$$

This parameter encompasses all forms of losses, including ohmic losses in the graphene sheet, dielectric losses in the substrate, and impedance mismatch losses, thereby providing a realistic measure of how effectively the antenna converts supplied power into radiation.

As shown in Figure 2.19, the antenna achieves total efficiencies exceeding 27% across the entire operational bandwidth, with a peak efficiency surpassing 45% near 200 GHz. This level of performance is noteworthy considering the inherent resistive losses in graphene, especially when the material is biased into the OFF state (low chemical potential $\mu_c = 0$ eV). The relatively high efficiency is attributed to several design factors, including optimized dipole geometry, controlled coupling, and a high-quality substrate. The tuning of dipole length, width, and feed gap ensures minimal reflection and efficient power transfer to the radiating surface. The strategic placement of parasitic elements enhances constructive interference without introducing excessive reactive loading. The use of low-loss polyimide ($\tan\delta = 0.0027$) minimizes dielectric dissipation at sub-THz frequencies. Collectively, these attributes allow the antenna to radiate a significant fraction of the input power, despite the limitations of graphene's conductivity relative to traditional metallic conductors.

The combined analysis of realized gain and total efficiency demonstrates that the proposed graphene-based antenna achieves a balanced trade-off between reconfigurability and radiative performance. While the realized gain is modest compared to conventional metallic antennas, it remains impressively stable and highly tunable, which is a crucial requirement for adaptive sub-THz communication and sensing systems. The results also underscore the effectiveness of graphene's dynamic bias control, which enables not only frequency tuning but also radiation pattern reconfiguration without severe degradation in efficiency. This characteristic is particularly beneficial for 6G and terahertz applications, where compact, low-power, and electronically steerable antennas are essential for in-chip or transparent system integration.

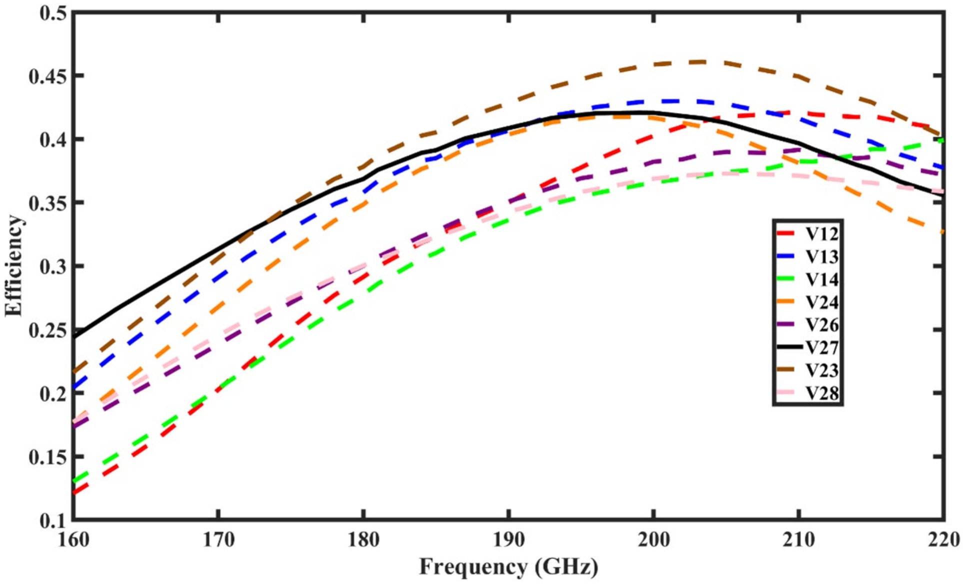

Figure 2.19: Efficiency of the proposed graphene-based antenna for eight different coding patterns

2.10 Radiation Pattern Reconfigurability

One of the most remarkable capabilities of the proposed graphene-based programmable dual-dipole antenna is its ability to dynamically reconfigure its radiation pattern through the controlled activation of selected parasitic elements. By applying specific coding patterns, which define the ON/OFF state of each parasitic element, the antenna can produce a wide range of far-field radiation characteristics, including single-beam, tilted-beam, dual-beam, and multibeam configurations. This electronic control is achieved without any mechanical motion, relying entirely on modulation of graphene's chemical potential (μ_c) to alter the surface conductivity and thereby adjust electromagnetic coupling.

The reconfiguration approach is based on electrical biasing of graphene's surface conductivity, which is described analytically by Eqs. (2.17) and (2.18). In the sub-THz regime, graphene's surface conductivity follows the Kubo formulation, where the intraband contribution dominates. By applying a voltage bias, the chemical potential increases, which in turn increases the conductivity and enables the parasitic elements to couple electromagnetically with the driven dipole (ON state). Conversely, when no bias is applied, the chemical potential approaches zero, the conductivity drops, and the parasitic element becomes electromagnetically transparent (OFF state). Thus, by selectively biasing individual parasitic elements according to a predefined coding pattern, the near-field current distribution is modified, allowing dynamic control of the far-field radiation pattern. In the following, coding patterns are denoted by a letter (V for vertical dipole active, H for horizontal dipole active) followed by the indices of the parasitic elements that are switched ON. For example, V3 means the vertical dipole is excited and parasitic element number 3 is in the ON state (all others OFF).

Figure 2.20 illustrates the simulated azimuthal radiation patterns (in the $\theta = 90°$ plane) for several representative coding configurations, focusing first on single-beam patterns and then on asymmetric two-state patterns that produce beam tilting or dual-beam behavior. The generation of a single, highly directional main lobe can be achieved by activating only one parasitic element in conjunction with one of the orthogonal dipoles. A representative case is the V3 coding pattern (Figure 20a), in which the vertical (V) dipole serves as the driven element while parasitic element 5 positioned along the negative y-axis, is switched to the on state ($\mu_c =$

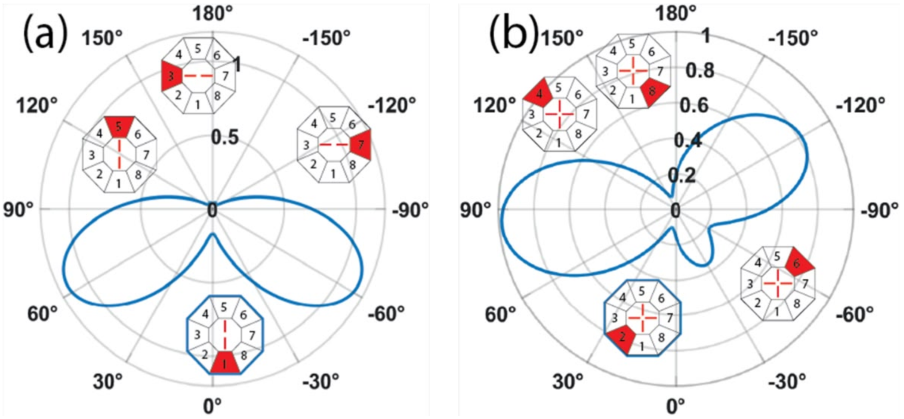

Figure 2.20: Azimuthal radiation patterns for coding patterns involving the horizontal dipole. (a) Patterns for odd-numbered parasitic element activations: H1, H3, H5, H7. (b) Patterns for even-numbered parasitic element activations: H2, H4, H6, H8. The patterns illustrate the 90° rotational symmetry and beam reconfigurability of the antenna.

1 eV). All other parasitic elements remain in the off state ($\mu_c = 0\,\text{eV}$), thus being electromagnetically transparent.

In this configuration, the activated parasitic element 5 acts as a plasmonic director, coupling strongly with the nearby vertical dipole and reinforcing radiation toward its direction. As a result, the antenna produces a single main beam radiation lobe oriented at $\phi = -90^\circ$, corresponding to the direction of the active parasitic element. The simulated half-power beamwidth (HPBW) of this beam is approximately 79.2°, indicating moderate beam focusing, while the peak realized gain reaches 1.44 dBi, consistent with efficient radiation enhancement in the intended direction.

This behavior validates the fundamental Yagi-Uda-inspired mechanism governing the antenna's reconfigurability: when a parasitic element is activated (high conductivity), it becomes an effective re-radiator that modifies the phase front of the electromagnetic field, steering the main lobe toward its location. Due to the C4 rotational symmetry of the antenna geometry, this behavior is replicable through 90° rotations of the active configuration. For instance, activating V5, H7, or H3, which corresponds to elements located at successive 90° intervals, produces the same single-lobe radiation pattern, but rotated by 90°, 180°, and 270° in the azimuth plane, respectively. Consequently, the antenna supports four discrete beam orientations (0°, 90°, 180°, and 270°), offering full quadrantal coverage. This symmetry-driven reconfigurability demonstrates the antenna's potential for beam selection and switching, which can be realized instantaneously through electrical control of the parasitic bias voltage. Such a feature is especially valuable in sub-THz communication systems requiring adaptive link alignment, directional beam scanning, or user tracking. While single-parasitic activation leads to clearly directed beams, activating two parasitic elements simultaneously allows more complex and tunable radiation patterns to emerge, including dual-lobe and tilted single-beam configurations.

A representative example is the H3 coding pattern (Figure 2.20a), in which parasitic sectors 3 and 7 are switched ON while the horizontal dipole is excited. The electromagnetic interference between the fields re-radiated from these two active parasitic elements creates a distinctive radiation pattern featuring two main lobes oriented symmetrically at $\phi = \pm 63^\circ$ with respect to the dipole axis. This configuration effectively divides the radiated power between the two directions, forming a dual-beam radiation pattern. Such dual-beam states are particularly useful for spatial diversity applications or simultaneous multi-link communication, where coverage of two spatial regions is desired without physically reorienting the antenna.

Another important configuration, V2 (Figure 2.20b), demonstrates a case of asymmetric two parasitic activations, leading to a tilted single-beam radiation pattern. Here, the non-symmetric positioning of the active parasitic elements breaks the fourfold symmetry of the structure, resulting in a directionally shifted main lobe. The reduced symmetry (approaching a D4-like configuration) allows for finer beam control, where small changes in ON/OFF coding of parasitic elements cause measurable and repeatable angular shifts in the beam direction.

The same principle applies to other equivalent coding patterns (V4, V6, V8) and their horizontal dipole counterparts (H1–H8), which produce mirrored or rotated versions of these beam shapes, collectively covering eight distinct azimuthal directions. Thus, through appropriate combinations of active parasitic elements, the antenna can steer its main lobe in discrete angular steps, achieving full 360° coverage in the azimuthal plane. Radiation patterns that are symmetric about a single axis exhibit similar characteristics, as illustrated in Figure 2.21a, b, and c. Specifically, Figure 2.21a depicts the pattern generated by V3 coding configurations, which produces a single main lobe directed toward $\phi = -90°$. The corresponding coding pattern is marked by a blue outline, while other plots show equivalent encodings that yield the same patterns when rotated or mirrored about the center or the x- and y-axis. Dual-beam operation is achieved when two parasitic elements are activated in a symmetrical or quasi-symmetrical arrangement around the driven dipole, as illustrated in Figure 2.22(a)–(e). The coding pattern V26 (Figure 2.22a) represents one such configuration, in which parasitic sectors 2 and 6 are switched to the ON state while the vertical dipole acts as the active radiator. In this mode, the surface currents induced on the ON-state elements generate two strong secondary radiation sources located symmetrically with respect to the main dipole axis. As a result, far-field interference produces two distinct and well-defined main lobes oriented at $\phi = 30°$ and $\phi = -150°$, respectively. These lobes are separated by 180°, reflecting the spatial symmetry of the activated parasitic elements. Since the radiated power is equally divided between the two lobes, the realized gain per beam is slightly reduced, reaching approximately -0.28 dBi. Nevertheless, this configuration clearly demonstrates the antenna's capability to support dual-directional

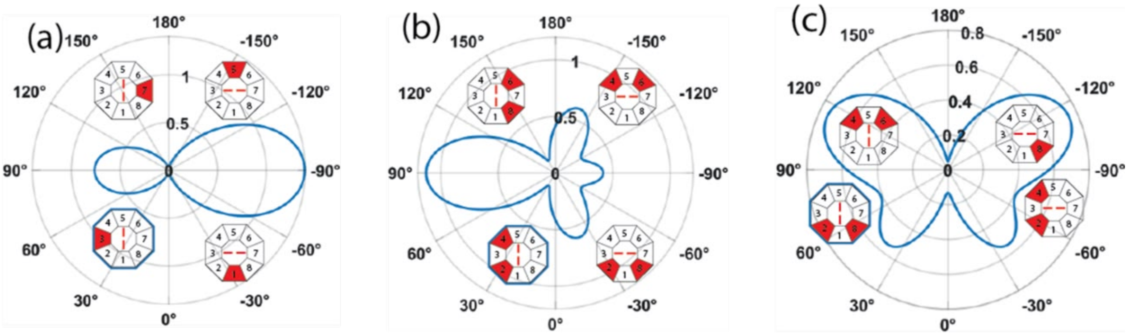

Figure 2.21: Single and dual beam configuration under different coding patterns (a) Radiation pattern for coding sequence H1 and H5, which are 90° rotationally symmetric to V3 and V5, respectively, (b) Radiation pattern for coding sequence H46 and H28, which are 90° rotationally symmetric to V68 and V24, respectively, and (c) Dual beam radiation pattern H48 and H24 which are 90° reflected to V28 and V46, respectively.

radiation, which is particularly attractive for bidirectional sub-THz communication links and spatially diverse sensing applications.

A similar dual-beam operation with enhanced gain is obtained using the V37 coding pattern, as shown in Figures 2.23(b) and (c). In this case, parasitic elements 1 and 3 are activated while the vertical dipole remains the driven element. The interaction between the electromagnetic fields radiated by these two parasitic elements gives rise to two main lobes centered at $\phi = \pm 69.2°$, symmetrically positioned about the dipole axis. Owing to the favorable phase relationship and stronger mutual coupling between the activated parasitic elements, the peak realized gain per lobe increases to 1.63 dBi. This improvement indicates more efficient power transfer and stronger constructive interference, resulting in higher-gain beams while preserving wide angular separation. These results highlight the programmable flexibility of the proposed antenna, where simple reconfiguration of the parasitic coding state enables precise control over beam orientation and separation.

Extending this concept further, the antenna can be programmed to simultaneously generate four distinct main beams covering multiple azimuthal sectors. This operating mode is demonstrated by the V2468 coding pattern (Figure 2.23d), in which every alternate parasitic element—specifically elements 2, 4, 6, and 8—is switched to the ON state, while the remaining elements remain OFF. This symmetric activation scheme establishes a C_4 symmetry in the surface current distribution around the antenna center. Each ON-state parasitic element behaves as a secondary radiator positioned at 90° intervals, leading to the formation of four identical radiation lobes uniformly distributed in the azimuth plane. The resulting far-field pattern exhibits four main lobes directed at $\phi = \pm 37.2°$ and $\phi = \pm 142.8°$, with each lobe exhibiting nearly identical amplitude and phase characteristics. Since the total radiated power is distributed among four distinct directions, the realized gain per beam is reduced to approximately -0.87 dBi. Despite the lower gain per lobe, this configuration provides broad azimuthal coverage without requiring mechanical scanning, making it particularly advantageous for multi-user communication scenarios, cellular sector coverage, and short-range radar or imaging systems in which simultaneous illumination of multiple directions is required.

The formation of such multi-beam radiation patterns can be physically interpreted through the vector superposition of the fields re-radiated by each parasitic element. When four parasitic elements are symmetrically activated, their individual radiation contributions interfere constructively along specific azimuthal directions while destructively canceling in others, naturally giving rise to multiple evenly spaced beams. Since the effective phase and amplitude of each parasitic element can be electronically controlled by tuning the graphene chemical potential (μ_c), the resulting radiation pattern is fully programmable and reversible. The capability to generate single-, dual-, and quad-beam radiation modes from the same planar structure highlights the versatility of the proposed antenna architecture [112]. In

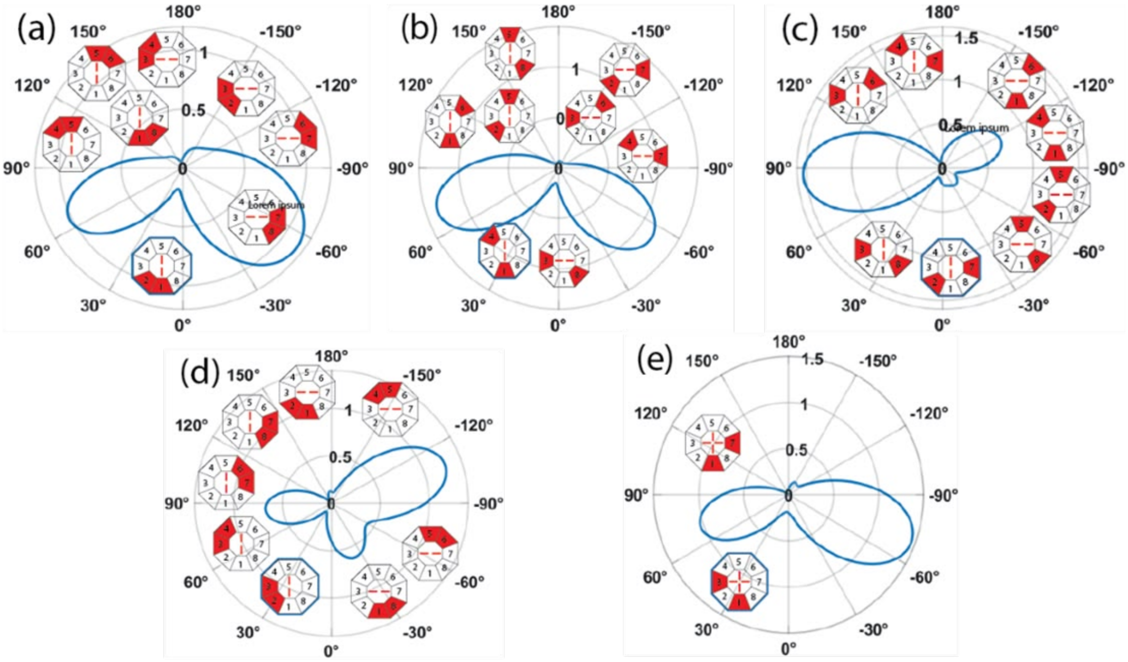

Figure 2.22: Radiation patterns showing 90° rotational symmetry for different coding patterns with 2-ON states in both vertical and horizontal dipoles from a-e.

contrast to conventional phased-array systems, which rely on complex feeding networks and bulky phase shifters, the proposed design achieves beam synthesis solely through near-field coupling control enabled by graphene's tunable conductivity. The absence of additional biasing lines or lumped components significantly reduces parasitic losses and fabrication complexity. Moreover, the multi-beam functionality is highly attractive for next-generation sub-THz wireless systems, where dynamic directional coverage is essential for maintaining high data rates, enabling spatial multiplexing, and supporting adaptive link formation.

The effective phase and amplitude of the currents induced on each parasitic element are controlled by tuning the graphene chemical potential μ_c. This is because the complex surface conductivity of graphene (Eq. 2.21) determines both the magnitude and the phase of the induced current. Increasing μ_c (ON state) raises the conductivity magnitude and shifts the phase of the induced current relative to the driven dipole. By adjusting μ_c (e.g., from 0 to 0.5 eV), one can continuously vary the induced current's amplitude and phase, enabling precise control over the constructive or destructive interference that shapes the far-field pattern. This tunability makes the radiation pattern fully programmable and reversible.

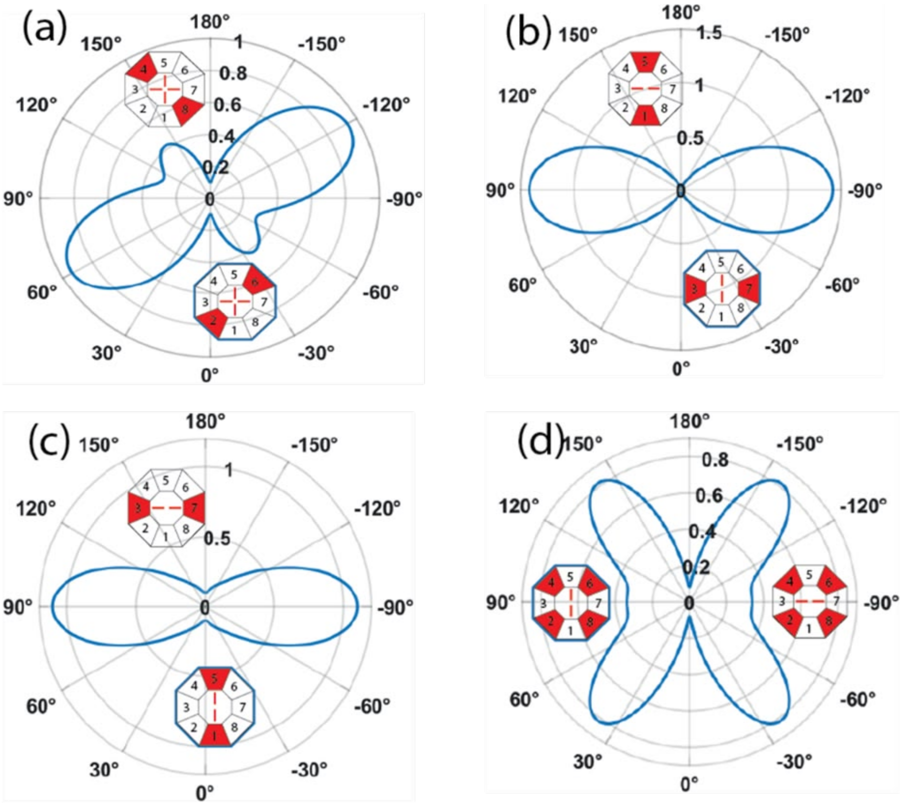

Figure 2.23: 90° Rotational symmetry of two ON states (a) V48 and H26 (b) H15 and V37, (c) V15 and H37 and (d) H2468 and V2468

2.10.1 Exploiting Symmetry for 360° Beam Steering

The inherent C$_4$ rotational symmetry of the proposed dual-dipole antenna provides an efficient mechanism for achieving full 360° beam steering using a minimal set of coding patterns. Owing to the geometrical symmetry of the antenna and its surrounding parasitic elements, radiation characteristics generated within one azimuthal quadrant can be replicated in the remaining quadrants through simple mathematical transformations of the excitation codes. These symmetry operations are defined as follows.

A 90° clockwise rotation is obtained by switching the active dipole from horizontal (H) to vertical (V), or vice versa, while simultaneously increasing each element index in the coding sequence by 2 (modulo 8). For example, the coding pattern H15 is transformed into V37 under a 90° clockwise rotation. A reflection with respect to the x-axis preserves the active dipole orientation but interchanges the parasitic element indices according to (1,2) $\leftrightarrow$ (8,7) and (3,4) $\leftrightarrow$ (6,5), while elements 1 and 5 remain invariant. Similarly, reflection about the y-axis maintains the same active dipole while exchanging (8,1) $\leftrightarrow$ (2,3) and (7,6) $\leftrightarrow$ (4,5).

By exploiting these symmetry operations, all possible beam orientations can be generated from a limited number of primitive encoding states. As illustrated in Figure 2.24, the base codes H15, H35, H345, V17, and V37 are sufficient to systematically reconstruct the entire azimuthal beam space through rotations and reflections. This symmetry-based strategy significantly reduces the number of required control states, thereby lowering computational overhead and simplifying the bias control circuitry used to modulate the graphene chemical potential.

When successive 90° rotational operations are applied to these base codes, identical beam steering behavior is reproduced in each quadrant, enabling full 360° azimuthal coverage, as conceptually shown in Figure 2.25. These results confirm that the antenna performs true beam steering rather than mere pattern reconfiguration, allowing directional radiation in discrete, programmable angular steps. Furthermore, the angular resolution and total number of achievable beam directions can be increased by employing a larger number of parasitic elements or by introducing multi-state (analog) control of the graphene chemical potential. Such scalability makes the proposed architecture well suited for future sub-THz adaptive and reconfigurable communication systems.

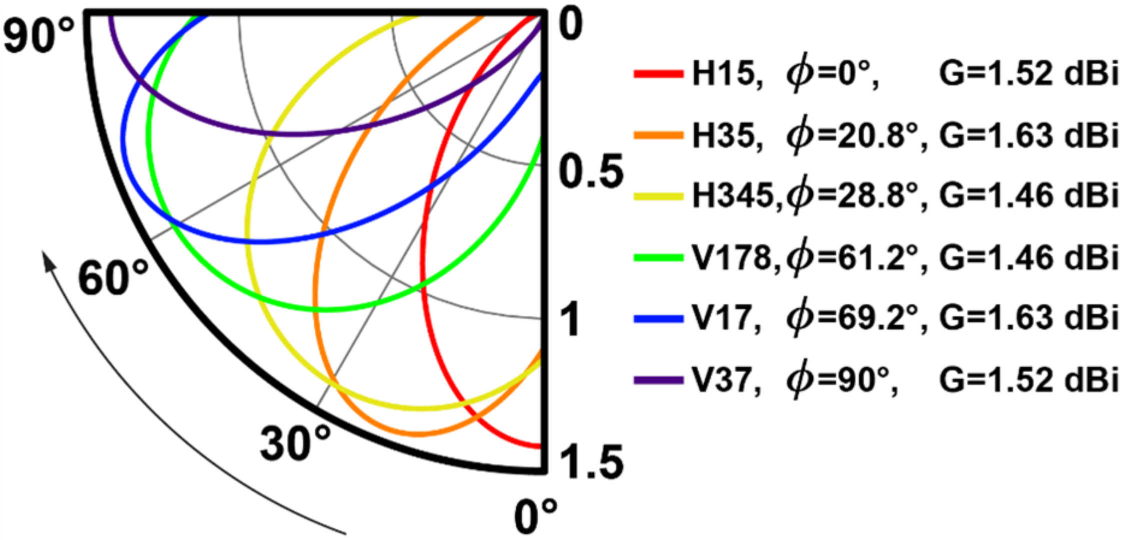

Figure 2.24: Azimuthal plane radiation patterns ($\theta = 90°$) for codings H15, H35, H345, V178, V17, and V37

2.10.2 Radiation Pattern in the Elevation plane

Although the primary reconfiguration objective of the antenna is azimuthal beam control, the performance in the elevation plane is equally significant for understanding overall radiation behavior. Figure 2.26 presents the elevation-plane cuts ($\phi = 90°$) for the three primitive encodings, H15, H35, and H345.

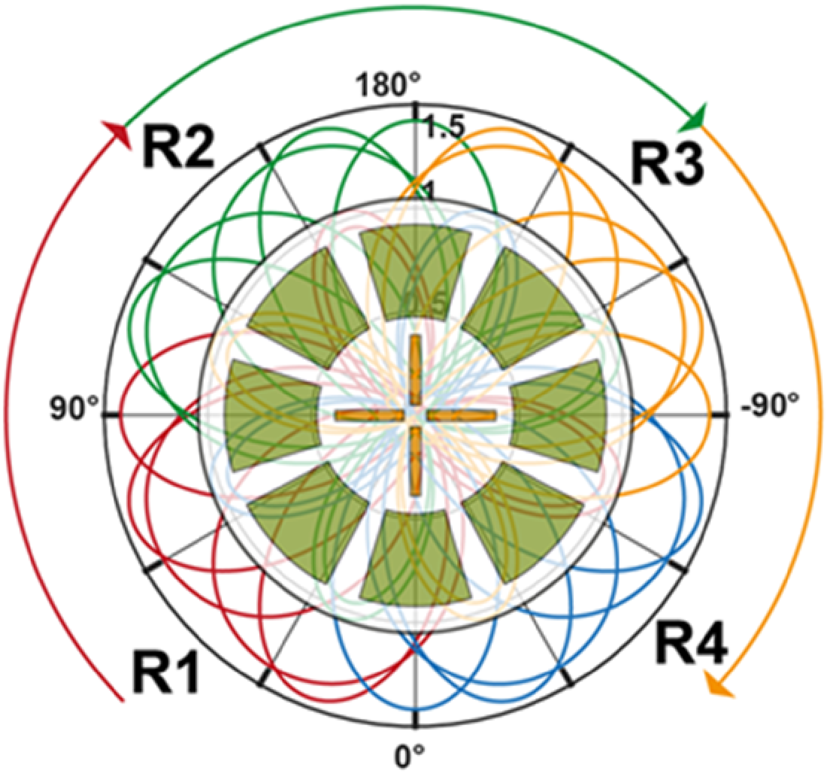

Figure 2.25: Pattern reconfigurability achieved from 0° to 360°

The resulting patterns exhibit a well-defined broadside maximum at ($\theta = 90°$), consistent with typical planer antenna characteristic. A slight downward tilt of the main lobe is observed, attributed to refraction within the polyimide substrate, which effectively bends the radiated field toward the dielectric medium. The similarity of elevation-plane responses among different codes confirms that beam reconfiguration primarily influences the azimuthal field distribution, leaving the elevation characteristics largely unaffected.

Additionally, the half-power beamwidth (HPBW) in the elevation plane is broader compared to the azimuthal plane. This behavior stems from the antenna's thin, disc-like geometry, which offers limited aperture height and this lower vertical directivity. The broader elevation lobe, however, ensures stable radiation performance even under slight mechanical misalignments, which is beneficial for mobile sub-THz applications.

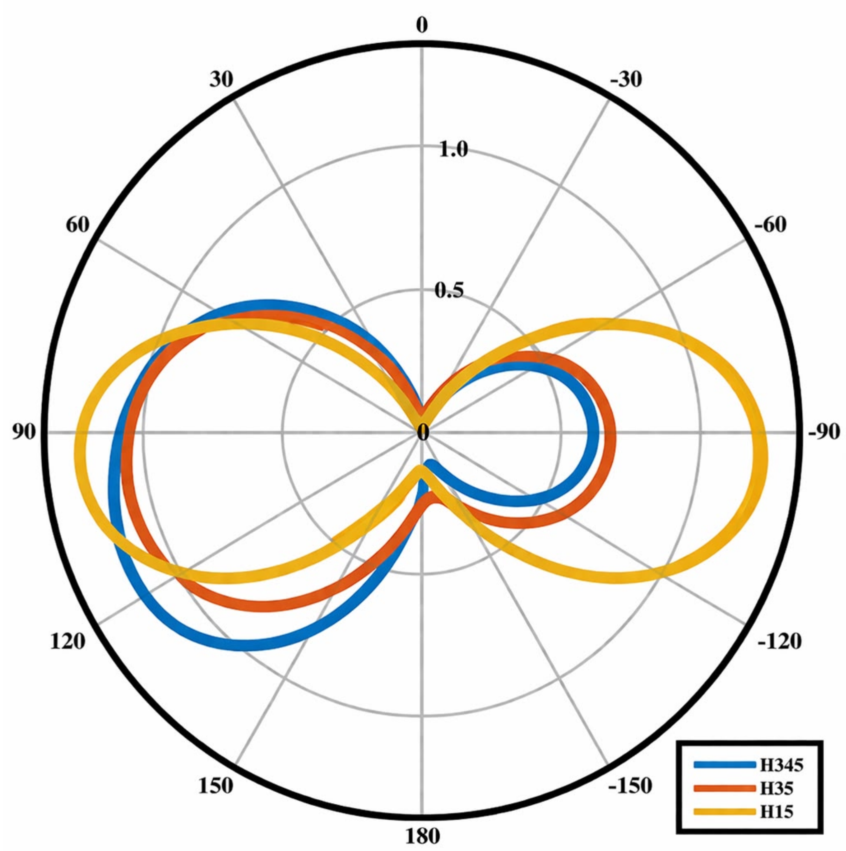

Figure 2.26: Radiation pattern of the coding patterns H345, H35, and H15 at ($\phi = 90°$) in the elevation plane

2.11 Analysis of Radiation Pattern Characteristics and Performance Benchmarking

The performance benchmarking in this chapter relies on key radiation metrics such as realized gain, impedance bandwidth, beam steering capability, and angular beamwidth. These parameters are used to systematically evaluate the effectiveness of various coding patterns in controlling the radiation characteristics of the proposed antenna.

The comprehensive radiation performance of the proposed graphene-based dual-dipole antenna has been summarized in Table 2.5, which lists the main beam direction (ϕ), realized gain (G), and beamwidth ($\Delta\phi$) for several representative coding patterns. The data clearly indicates that by carefully selecting the ON/OFF configuration of the graphene parasitic elements, the antenna can generate a wide range of directional radiation patterns, covering multiple azimuthal angles with controllable gain and beamwidth. Each coding pattern corresponds to a specific combination of active parasitic elements, which modifies the current distribution on the antenna surface and consequently the phase front of the radiated fields.

Importantly, despite these variations in coding configuration, the antenna impedance bandwidth and spectral stability of the antenna remain consistent, demonstrating that beam reconfiguration can be achieved without compromising matching performance or radiation efficiency. The angular position of the main lobe and its gain can be accurately predicted from the chosen code, validating the deterministic nature of the proposed beam steering method.

Table 2.5: Beam characteristics for various coding patterns: angular direction of the main lobe ϕ, corresponding maximum gain G (dBi), angular beamwidth $\Delta\phi$, and additional directions of the main lobe that can be achieved under symmetric codes ϕ_s.

Code	ϕ [°]	ϕ_s [°]	**G [dBi]**	$\Delta\phi$ [°]
V_1	±63.2	$\pm26.8, \pm116.8, \pm153.2$	0.56	64.7
V_2	85	$\pm5, -85, \pm95, \pm175$	-0.07	75.8
V_3	-90	0, 90, 180	1.44	79.2
V_{12}	-52.8	$\pm37.5, 52.8, \pm127.2, \pm142.8$	0.59	82.3
V_{14}	70.2	$\pm19.8, -70.2, \pm109.8, \pm160.2$	1.08	59.6
V_{27}	86.7	$\pm3.3, -86.7, \pm93.3, \pm176.7$	1.86	66.0
V_{23}	-109.3	$\pm19.3, 70.7, \pm109.3, \pm160.7$	0.89	63.9
V_{13}	-69.2	$\pm20.8, 69.2, \pm110.8, \pm159.2$	1.63	65.9
V_{24}	90	0, -90, 180	0.51	65.5
V_{28}	±114	$\pm26.8, \pm116.8, \pm153.2$	-1.26	129.5
V_{26}	61.1	$\pm28.9, -61.1, -118.9, \pm151.1$	-0.28	67.0
V_{37}	-118.9	0, 180	1.52	64.1
V_{15}	±90	0, 180	0.43	58.8
V_{2468}	$\pm37.2, \pm142.8$	$\pm52.8, \pm127.2$	-0.87	48.8

2.11.1 Benchmarking Against State-of-the-Art Sub-THz Antennas

A comprehensive performance analysis, presented in Table 2.6, benchmarks the proposed design against existing state-of-the-art antennas operating in the subterahertz frequency regime. The comparison includes various architectures such as leaky-wave antennas, phased arrays, dielectric resonator antennas (DRAs) and graphene-based devices reported in the literature. From the analysis, it is evident that while several of these antennas demonstrate impressive, realized gains and limited angular steering capabilities (typically between ±20° and ±80°), none of the previously reported designs achieve continuous or discrete 360° beam coverage in the azimuthal plane within this frequency range. Most traditional THz antennas rely on either mechanical rotation or complex phase shifting networks to achieve steering, both of which introduce latency, increase fabrication complexity, and reduce optical transparency.

In contrast, the proposed design attains 360° beam steering using purely electronic reconfiguration of graphene's chemical potential . This is achieved through the application of simple coding transformations based on the antenna's inherent C_4 symmetry, as discussed earlier. Although the maximum realized gain (2 dBi) is lower than that of certain fixed-beam or lens-assisted antennas, this is an expected and acceptable trade-off for achieving complete azimuthal coverage and electronic programmability. Generally, a gain-verses-steering-angle trade-off exists in antenna design: wider steering capabilities trend to distribute radiated power across a broader angular range, resulting in a reduction in peak gain.

One of the key advantages of the proposed graphene-based structure lies in its dynamic programmability. The ON/OFF state of each parasitic element can be independently controlled using Field-Programmable Gate Arrays (FPGAs), which serve as digital controllers to apply precise bias voltages to each graphene sector. This electronic control enables real-time beam reconfiguration, allowing the antenna to adapt its radiation direction instantaneously in response to varying channel conditions, user positions, or communication requirements. The versatility of the antenna can be further enhanced by investigating more complex coding schemes. While the current study primarily focuses on configurations with two active (ON) parasitic elements, future work will explore encoding with multiple ON states (Three, four, or more). Such configurations can potentially yield multi-beam radiation patterns, improved beam shaping, and enhance coverage efficiency.

Additionally, the mutual coupling and interference effects between the horizontal and vertical dipoles will be studied under simultaneous excitation conditions. The superposition of their radiation fields could introduce additional degrees of freedom, enabling hybrid beam patterns, polarization reconfiguration, and finer beam control. This line of research may ultimately extend the functionality of the antenna beyond discrete beam steering to include adaptive beam synthesis for multi-user and multi-band terahertz communication systems.

To the best of our knowledge, no prior antenna operating in the sub-THz or THz range has demonstrated full 360° beam steering in the azimuthal plane within a single, transparent, planar structure. Most steerable designs (e.g., leaky-wave antennas, phased arrays, dielectric resonator antennas) achieve scanning ranges of ±20° to ±80°, as shown in Table V. A few works have achieved 360° steering using mechanisms such as rotating a feed in front of a Luneburg lens [118] or employing a reconfigurable transmitarray with PIN diodes [119], but these designs are not transparent and involve moving parts or complex biasing networks. The proposed design is the first to achieve full 360° electronic steering in a transparent, graphene-based platform.

Table 2.6: Comparison of reported antennas operating at high frequency mm-wave and sub-THz bands.

Ref.	**Antenna type**	**Freq. (GHz)**	**Gain (dBi)**	**Steering tech.**	**Angle (°)**
[113]	LWA	360–400	4.5	FS	80
[114]	Phased array	300	2.3	OE	50
[115]	Phased array	318–370	4	Electrical	128/53
[116]	DRA single	340	5.9	Fixed	Fixed
[117]	Graphene dipole	300	10.6	Photodiodes	0–20
[118]	Yagi–Uda	300	17	Lens array	±73
This Ph.D. thesis	Graphene dual dipole	200	2	Graphene	0–360

2.11.2 Power Consumption Analysis and 6G/7G Requirements

The total power consumption of the proposed antenna includes two components: (i) the RF power delivered to the driven dipole, and (ii) the DC biasing power for the graphene parasitic elements. The total efficiency (Figure 2.19) reaches a maximum of 45% at 200 GHz, meaning that 45% of the input RF power is radiated, while 55% is dissipated as ohmic losses in graphene and dielectric losses in the substrate. This efficiency is competitive with other graphene-based antennas at sub-THz frequencies (see Table 4.2) and is acceptable for short-range 6G applications where compactness and reconfigurability outweigh raw efficiency. The biasing power is given by $P_{\text{bias}} = N_{\text{ON}} \cdot V_g \cdot I_{\text{leak}}$, where N_{ON} is the number of parasitic sectors switched ON, $V_g \approx$ 5–10 V is the gate voltage, and I_{leak} is the gate leakage current (typically < 1 nA for high-quality dielectrics). Thus, $P_{\text{bias}} \approx 8 \times 10 \times 10^{-9} = 0.08$ μW, negligible compared to the RF power (typically in the mW range). Therefore, the antenna's power consumption is dominated by the RF input power, not the biasing network.

Table 2.6 compares gain and steering angle but not power consumption. Extending the comparison: most sub-THz antennas in the literature (leaky-wave, phased arrays, dielectric resonator antennas) require either high DC bias currents (e.g., PIN diodes, varactors) or complex feeding networks that introduce additional losses.

Future wireless generations (6G and 7G) demand ultra-low-power devices to support massive IoT, battery-less sensors, and dense cell deployments [120, 121]. The proposed antenna, with its negligible DC biasing power and moderate RF efficiency, aligns with these requirements. However, further efficiency improvements (e.g., via substrate engineering or multi-layer graphene) are needed to compete with metallic antennas for long-range links.

2.12 Conclusion

The research presented in this chapter focused on the design and numerical evaluation of a programmable transparent antenna intended for operation in the subterahertz (sub-THz) frequency regime. The proposed structure consists of two orthogonally oriented graphene dipoles integrated on a polyimide substrate, surrounded by eight fan-shaped graphene parasitic elements. Unlike conventional phased arrays, the proposed design combines structural symmetry, optical transparency, and electrical tunability to achieve full 360-degree azimuthal beam control using a limited set of primitive coding states, reducing system complexity while maintaining accurate beam orientation.

By modulating the chemical potential of graphene, the electromagnetic behavior of each parasitic element can be dynamically controlled, allowing them to act as either active or passive elements. Through appropriate programming, the antenna successfully generates single-beam, dual-beam, and quad-beam patterns, demonstrating graphene's capability as an efficient switching and beam-shaping material at sub-THz frequencies. The antenna achieves a maximum realized gain of 2 dBi for single-beam configuration, 1.3 dBi for dual-beam operation, and 0.7 dBi for quad-beam mode, with a -10 dB impedance bandwidth extending from 187 GHz to 214 GHz.

These performance characteristics make the proposed antenna well suited for emerging applications such as 6G indoor communications (high-data-rate access with electronic beam tracking), transparent smart surfaces (>99% transmittance for windows and displays), short-range radar (multi-direction sensing for drones and autonomous vehicles), and spectroscopy (material characterization across 187-214 GHz). In summary, this chapter demonstrates the combination of optical transparency, pattern reconfigurability, and beam programmability within a single compact structure operating at 200 GHz. These contributions establish a new design paradigm for sub-THz beam steering antennas, offering a pathway toward low-complexity, transparent, and programmable radiating systems for future 6G and smart environment applications.

Chapter 3

Pattern Reconfigurability of Graphene Dipole Antennas Via Magnetic Biasing

3.1 Introduction

Beam steering (the ability to electronically direct the main radiation lobe without mechanical movement) is a critical functionality for terahertz (THz) communication, sensing, and radar systems. Conventional phased arrays provide fast steering but suffer from high complexity, cost, and power consumption, especially at sub-THz frequencies [122]. Alternative architectures such as leaky-wave antennas, reflectarrays, and transmitarrays have been extensively investigated; however, they still involve trade-offs among steering agility, bandwidth, efficiency, and implementation complexity [123].

In the THz, optical and infrared regimes, metasurfaces (arrays of subwavelength scatterers) have enabled a paradigm shift in wavefront control [123]. Static dielectric metasurfaces based on high-index materials (e.g., GaN, silicon, TiO_2) have demonstrated efficient beam deflection, focusing, and holography [123]. However, their lack of post-fabrication tunability restricts adaptability to varying environmental conditions [124]. Various tuning mechanisms for metasurfaces (thermo-optic, electro-optic, carrier depletion, phase-change, mechanical actuation) are discussed in Chapter 4.

Graphene, a two-dimensional material with electrically tunable conductivity, has emerged as a promising platform for reconfigurable antennas (as demonstrated in Chapter 2). When a magnetic field is applied to graphene, its conductivity becomes anisotropic and is described by a tensor with non-zero off-diagonal (Hall) terms, inducing non-reciprocal wave propagation and controllable phase shifts.

Magnetically biased graphene has been explored for several THz applications.

Correas-Serrano et al. [125] investigated magnetized graphene cylindrical waveguides and proposed their use for reconfigurable dipole antennas in the low THz band. Hlali et al. [126] analyzed a non-reciprocal antenna array based on magnetized graphene for THz applications. Fakhte and Taskhiri [127] designed a THz dielectric rod antenna using magnetically biased graphene to switch between linear and circular polarizations. More recently, Taskhiri and colleagues [128] demonstrated a THz dielectric resonator antenna that uses a DC magnetic bias to switch between linear and circular polarizations. Additional studies have examined magnetized graphene for frequency selective surfaces [129], non-reciprocal leaky-wave antennas [130], and Faraday rotation in stacked magnetized graphene [131].

Despite the successful use of magnetically biased graphene for polarization manipulation and non-reciprocal functionalities, the realization of dynamic and continuous beam steering has received limited attention. To the best of our knowledge, magnetic-field-controlled beam steering in graphene-based dipole antennas incorporating parasitic elements has not yet been investigated. This chapter directly addresses this gap by proposing a dipole antenna with eight parasitic elements whose radiation pattern can be steered using out-of-plane and in-plane magnetic fields in the sub-THz range.

This mechanism offers several benefits. It provides contactless biasing: a single uniform magnetic field can be applied to different combinations of parasitic elements, eliminating the need for dense individual biasing networks and significantly simplifying fabrication. By exploiting the conductivity tensor of graphene, the interaction between the dipole and the parasitic elements can vary both in magnitude and phase, effectively modulating the phase shift across the elements and enabling wide-angle, continuous steering, a capability difficult to achieve with conventional electrostatic biasing [132, 133].

It is worth noting that electrostatic biasing primarily enables scalar conductivity tuning, which limits independent phase and amplitude control compared to magnetically induced anisotropic conductivity. Moreover, the gain of the antenna can be enhanced by applying a magnetic field, resulting in reduced dissipative losses and current redistribution across the parasitic elements for a more directive radiation pattern, thus avoiding the off-resonance efficiency drawbacks common in electrostatically tuned parasitic elements. This work introduces a paradigm shift in the design of graphene-based antennas: from locally addressed, electrostatic-controlled reconfigurability towards beam steering controlled via magnetic bias [70].

In Chapter 2, the graphene dipole antenna with eight parasitic elements was designed at 200 GHz and the parasitic elements were dynamically controlled via electrostatic biasing to obtain pattern reconfiguration. In this chapter, we consider the same antenna as a starting point but aim to operate at 260 GHz according to IEEE standards. The frequency increase necessitates adjustments in the dipole length, parasitic element spacing, and electrostatic biasing levels to maintain proper resonance, beam steering capabilities, and impedance matching.

The 260 GHz band is of particular interest for emerging 6G wireless systems and THz sensing applications. According to IEEE Std 802.15.3d, the frequency range around 260 GHz offers a wide continuous bandwidth suitable for high-data-rate short-range communications (e.g., intra-chip or kiosk downloading) [134]. Additionally, this band lies within an atmospheric transmission window (relatively low oxygen and water vapor absorption), making it attractive for outdoor short-range links, high-resolution radar imaging, and spectroscopy. By operating at 260 GHz, the proposed antenna is directly applicable to these next-generation scenarios, while also allowing us to study the impact of increased plasmonic confinement and reduced parasitic element dimensions compared to the 200 GHz design in Chapter 2.

The behavior of the antenna at high frequency deviates from classical RF assumptions. In particular, the traditional half-wavelength dipole approximation no longer gives optimal performance due to the plasmonic properties of graphene, substrate effects, and strong frequency dispersion. Therefore, a systematic optimization approach is carried out to obtain better impedance matching, minimal shift from resonance, and enhanced overall performance.

3.2 Graphene Conductivity Tensor

By applying magnetic field on graphene, the motion of charge carriers is varied by the Lorentz force, leading to cyclotron frequency introducing Hall conductivity that couples orthogonal current components and breaking the symmetry in the material response. The surface conductivity of graphene under magnetic tuning is expressed as a second order tensor [135]:

$$\sigma = \begin{bmatrix} \sigma_{xx} & \sigma_{xy} \\ \sigma_{yx} & \sigma_{yy} \end{bmatrix} \tag{2}$$

where σ_{xx} and σ_{xy} denote the longitudinal and Hall conductivity, respectively. The beam steering and non-reciprocal wave propagation is enabled by the presence of non-zero off-diagonal terms (σ_{xy}).

Kubo formula can be used to derive the components of longitudinal and Hall conductivity under magnetic biasing conditions. These components are primarily dominated by the intraband transition at the THz frequencies and room temperature and can be expressed as:

$$\sigma_{xx} = \frac{e^2 \mu_c}{\pi \hbar^2} \frac{1}{\Gamma - j\omega} \tag{3.1}$$

$$\sigma_{xy} = \frac{e^3 B v_F^2}{\pi \hbar^2} \frac{1}{(\Gamma - j\omega)^2} \tag{3.2}$$

where e denotes the electron charge, μ_c is the chemical potential, $\hbar$ is the reduced Planck constant, and Γ represents the carrier scattering rate. The parameters ω, v_F, and B correspond to the angular frequency, Fermi velocity, and applied magnetic field strength, respectively. The values of σ_{xx} and σ_{xy} directly influence the amplitude and phase of the induced currents on the driven dipole and parasitic elements. In particular, the off-diagonal term σ_{xy} introduces an asymmetry in current distribution, allowing controlled rotation of the radiation pattern and enabling wide-angle, tunable beam steering. Therefore, carefull tuning of these conductivity components under magnetic biasing is essential for achieving accurate reconfigurable beam control.

An increase in the magnetic field intensity enhances the off-diagonal Hall conductivity term σ_{xy}, thereby inducing nonreciprocal behavior and asymmetry in the surface current distribution. This asymmetric electromagnetic response is the fundamental mechanism responsible for beam steering in magnetically biased graphene antennas and metasurfaces. Physically, the off-diagonal term σ_{xy} introduces a phase shift between orthogonal current components on the dipole and parasitic elements. This phase difference modfies the constructive and destructive interference of radiated fields, effectively rotating the main beam and enabling continuous steering over a wide angular range. For a simple illustration, consider an electric field applied along the x-direction (E_x). In the presense of a non-zero off-daigonal conductivity, a transverse current $J_y = \sigma_{xy} E_x$ is generated along the y-direction. This induced trasverse current redistributes the currents on the parasitic elements, creating asymmetry in the radiated fields and enabling controlled wide beam steering. By tuning the magnitude of σ_{xy} via magnetic field, the direction, shape, and directivity of the radiation pattern can be dynamically tuned, providing reconfigurable and nonreciprocal antenna behavior.

3.3 Wave Propagation and Non-Reciprocity in Biased Graphene

The conductivity tensor of magnetically biased graphene leads to non-reciprocal electromagnetic behavior, meaning that wave propagation features depend on the propagation direction [136,137]. This is basically different from graphene with electrostatic biasing, which remains reciprocal. Forward and backward propagation surface Plasmon polariton waves experience distinct phase velocities in magnetically biased antennas [138]. Mode coupling in magnetically tuned graphene occurs between orthogonal field components and radiation patterns become asymmetric [139]. This non-reciprocal behavior is required for obtaining continuous beam steering without complex feeding networks. Practically, this symmetry allows the main beam to be steered continuously in a desired direction without requiring complex feeding networks, since the wave experiences different phase accumulation along different paths. In other words, nonreciprocity translates directly into controllable rotation and shaping of the radiation pattern, enabling dynamic beam steering and enhanced directivity in magnetically biased graphene antennas [140].

3.3.1 Surface Plasmon Polaritons (SPPs) in Magnetically Biased Graphene

Graphene supports confined surface plasmons polaritons whose dispersion properties are impacted by magnetic biasing. The dispersion relation of SPPs on magnetically tuned graphene can be expressed as:

$$k_{\mathrm{SPP}} = \frac{\omega_{\mathrm{eff}}}{\sigma_{\mathrm{eff}}} \tag{3.3}$$

where σ_{eff} represents an effective conductivity that includes both longitudinal and Hall components. ω_{eff} is the effective angular frequency of the surface plasmon mode, which accounts for both excitation frequency and modifications due to the substrate and plasmonic response of graphene. The magnetic tuning modifies the SPP dispersion in such a way that propagation constantly becomes direction-dependent and phase gradients can be dynamically introduced along the antenna. Moreover, the strength of the magnetic field also controls the radiation pattern, and these effects directly translate into beam steering capabilities in graphene-based radiating structure.

3.3.2 Magnetoplasmons in Graphene via Magnetic Biasing

When a magnetic field is applied on graphene, it gives rise to magnetoplasmons, which are collective oscillations of charge carriers influenced by both plasmon confinement and cyclotron motion of electrons. Unlike conventional graphene surface plasmon polaritons, magnetoplasmons exhibit direction-dependent dispersion, enabling nonreciprocal guided waves along the graphene surface. The dispersion relation of graphene magnetoplasmons is determined by the poles of the two-dimensional dielectric response function given by [141]

$$1 - V(q)\,\Pi(q,\omega) = 0, \tag{3.4}$$

where

$$V(q) = \frac{2\pi e^2}{\varepsilon q}, \tag{3.5}$$

$$\Pi(q,\omega) = \text{polarization operator of graphene under magnetic bias.} \tag{3.6}$$

Efficient coupling between the free space THz radiation and magnetoplasmons relies on structural symmetry and excitation conditions. Patterning of graphene into finite geometries or periodic structures facilitates momentum matching between incident beam and magnetoplasmons modes, thus enabling efficient excitation. In the presence of magnetic bias, this coupling becomes inherently asymmetric in magnetic biased configurations, allowing preferential excitations of propagating modes in a single direction.

From an antenna perspective, this behavior is highly significant. Magnetically biased graphene supports direction-dependent guided modes, which can serve as travelling waves or leaky wave radiation channels, where the dispersion properties of the surface wave control the radiation pattern. By adjusting either the strength or polarity of the magnetic field, it becomes possible to dynamically modify the magnetoplasmons propagation thereby changing the beam shape and radiation angle.

Furthermore, the interplay between magnetoplasmons and magnetic tuning introduces an additional degree of freedom. As the magnetic field shows anisotropy and nonreciprocity, the Fermi levels control field confinement and loss. This biasing is unique to graphene and positions it as an attractive platform for terahertz reconfiguration, even though such antenna implementations have yet to be realized experimentally.

3.3.3 Practical Considerations for Magnetic Bias Implementation

The simulations assume a constant magnetic field of 2.5 T applied selectively to specific parasitic elements, either in-plane (magnetic field vector lying in the plane of the antenna) or out-of-plane (field perpendicular to the antenna plane). For example, a configuration like P12 means that parasitic elements 1 and 2 are simultaneously biased with a magnetic field of 2.5 T, while the remaining elements are unbiased. The same principle applies to other combinations (e.g., P34, P24, P37, P2468) and to both in-plane and out-of-plane orientations.

A field strength of 2.5 T is achievable with small neodymium permanent magnets (mm-scale) or with low-power electromagnets for short duty cycles. For out-of-plane selective biasing, small permanent magnets or micro-coils could be placed underneath each parasitic element. For in-plane selective biasing, patterned ferromagnetic layers or micro magnets integrated on the substrate surface would be required. However, such localized magnetic biasing is challenging to implement in practice due to field fringing, crosstalk between adjacent parasitic elements, and fabrication complexity. Perfect field uniformity over each biased sector is assumed in the simulations; in reality, leakage fields and gradients may reduce steering efficiency. These practical constraints are beyond the scope of this numerical study but should be addressed in future experimental work. For compact THz systems, a trade-off exists between steering angle (higher B gives larger tilt) and device size, weight, and complexity of the magnetic source array.

3.4 Initial Dipole Antenna design

The initial dipole antenna was designed on a silicon dioxide SiO_2 substrate and then eight parasitic elements were integrated around the two dipole arms, as shown in Figure 3.1. While the antenna in chapter 2 was designed on a polyimide substrate to achieve optical transparency, the magnetic biasing study in this chapter focuses on electromagnetic performance without the need for transparency. Therefore, a standard SiO_2 was chosen for its well-characterized dielectric properties (relative permittivity of 3.9 and loss tangent of 0.001), ease of integration with magnetic field sources, and lower cost for potential experimental validation. The same antenna geometry (dipole and eight parasitic elements) is retained, allowing a direct comparison between electrostatic tuning (chapter 2) and magnetic tuning (this chapter).

The design strategy began with the classical half-wavelength approximation; the length of the dipole arms was set to ($\lambda/2$) at 260 GHz, computed using the effective wavelength in the substrate medium. This configuration behaved as an initial point for the optimization process.

The 260 GHz band is of particular interest for emerging 6G wireless systems and terahertz sensing applications. According to IEEE standard 802.15.3d, the frequency range around 260 GHz offers a wide continuous bandwidth suitable for high data rate short-range communications (e.g., intra-chip or kiosk downloading) [134]. Additionally, this band lies within an atmospheric transmission window (relatively low oxygen and water vapor absorption), making it attractive for outdoor short-range links, high-resolution radar imaging, and spectroscopy. By operating at 260 GHz, the proposed antenna is directly applicable to these next-generation scenarios, while also allowing us to study the impact of increased plasmonic confinement and reduced parasitic elements dimensions compared to the 200 GHz design in chapter 2.

The initial simulation revealed significant deviations from the expected performance, including impedance matching and frequency shifting, confirming that $\lambda/2$ theory is not enough at terahertz frequencies, especially for antennas based on graphene. To address this issue, a parametric sweep in finite element simulation (FEM) using COMSOL with frequency-domain analysis was performed. Key antenna parameters such as dipole length, width, gap, substrate thickness and radius were varied, while monitoring the impedance matching, reflection coefficient (S_{11} and resonant frequency. The optimal configuration was selected based on achieving minimum reflection $S_{11} < -10\,\mathrm{dB}$ and alignment of the resonance with 260 GHz.

This approach allowed a quantitative evaluation of how each geometric parameter affects impedance matching and resonance, ensuring a guided and reproducible optimization process suitable for THz graphene antennas.

The most critical parameter in the design of dipole antenna is its length that governs the resonance. At sub-terahertz frequencies, the surface plasmon polariton

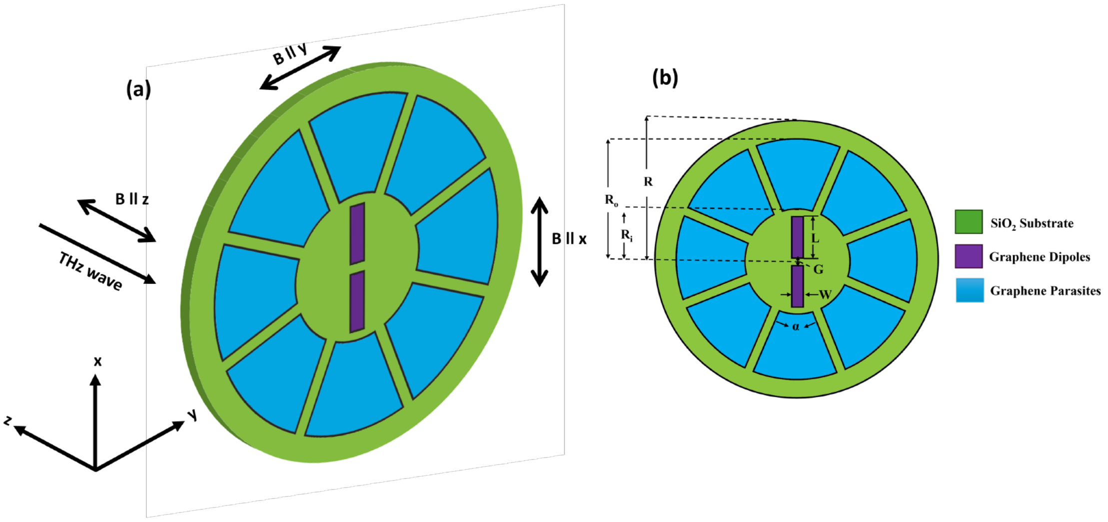

Figure 3.1: (a) 3D schematic of the graphene dipole antenna with eight parasitic elements under magnetic biasing. The configurations $B \parallel x$ and $B \parallel y$ correspond to in-plane magnetic fields, whereas $B \parallel z$ corresponds to the out-of-plane magnetic field, and (b) Top-view of the graphene dipole antenna.

(SPP) of graphene has impact on the effective electrical length, leading to the resonance occurs at a length much shorter than free space $\lambda/2$.

A parametric sweep on the length (L) of dipole arm was performed from 116-126 µm while monitoring the reflection coefficient over the frequency range around 260 GHz. The resonance was achieved at L = 122 µm, with a better impedance matching and -10 dB bandwidth from 240 GHz to 280 GHz. As shown in Figure 3.2, by either increasing or reducing the length from 122 µm, the frequency shifts, resulting in impacing the impedance matching. The behavior confirmed that impact of plasmons dominates the behavior of antenna at this frequency range, needing shorter arm lengths than calculated classical theory. After fixing the dipole arm length, varying it between 35-45µm in 2µm step has only a minor impact on the impedance bandwidth and rsonant frequency, as depicted in Figure 3.3.The impedance matching improves with a slight broadening at W = 39 µm, due to reduced ohmic losses and then reduces by further increasing. However, excessively large arm width reduces the field confinement and increased capacitive effects. An optimal arm width was therefore selected to obtain the trade-off between low S_{11} parameters and stable resonance near 260 GHz.

The gap between the feeding arms plays a significant role in determining the coupling strength and input capacitance of antenna. A parametric sweep was carried out by varying the gap from 20-25 µm with a step size of 1 µm and analyzed its impact on reflection coefficient. As shown in Figure 3.4, a 24 µm gap increased capacitive coupling leads to improve impedance matching and the values below and above 24 µm reduced coupling, resulting in degrading impedance matching. The

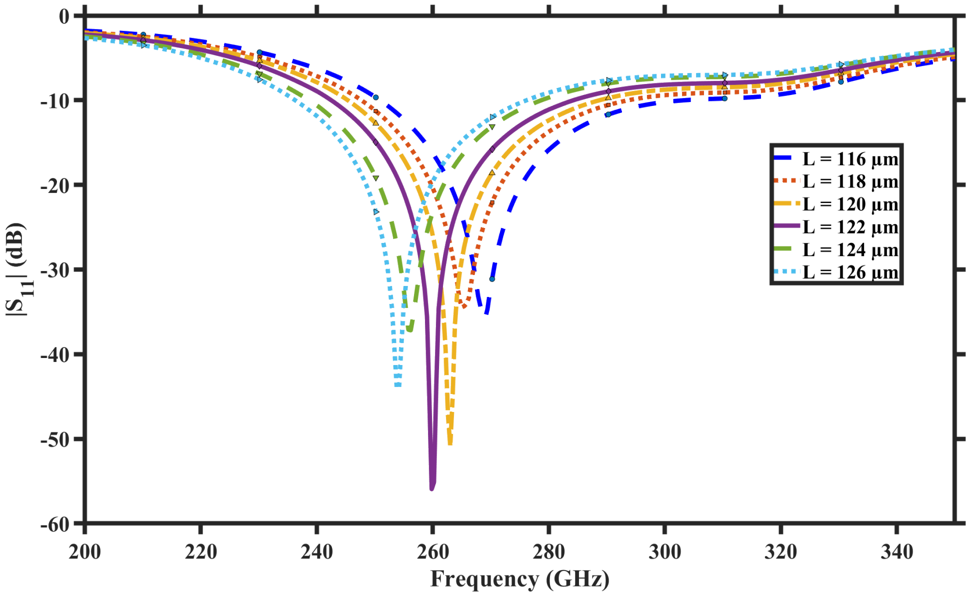

Figure 3.2: S_{11} versus frequency as a function of L

resonance also experiences a slight shift with variation in gap. Finally, the thickness of substrate was also varied from 200 µm to 250 µm with a step size of 10 µm , and it has impact on antenna with substrate and the effective permittivity at sub-terahertz frequencies, as shown in Figure 3.5. Simulation results highlighted

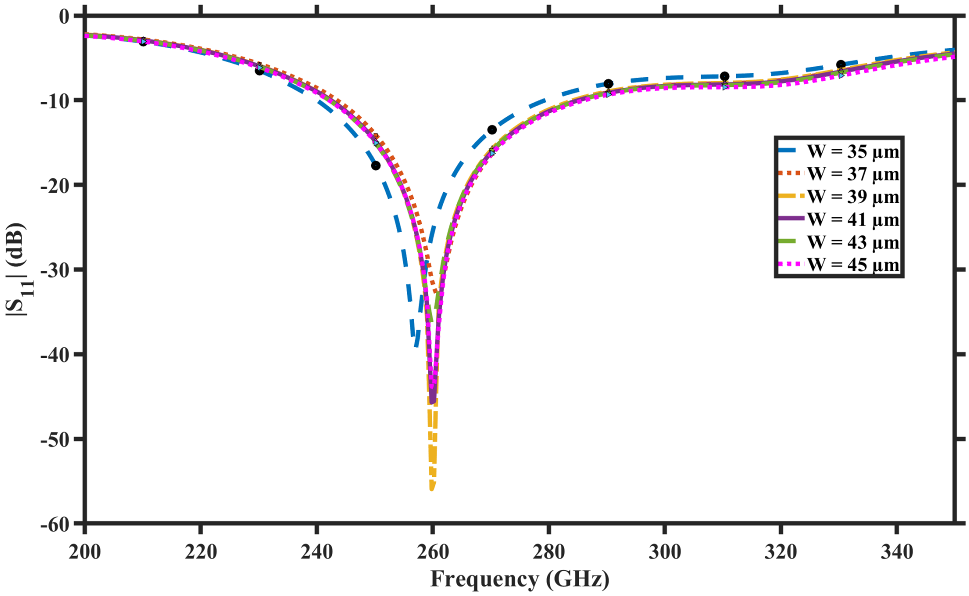

Figure 3.3: S_{11} versus frequency as a function of W

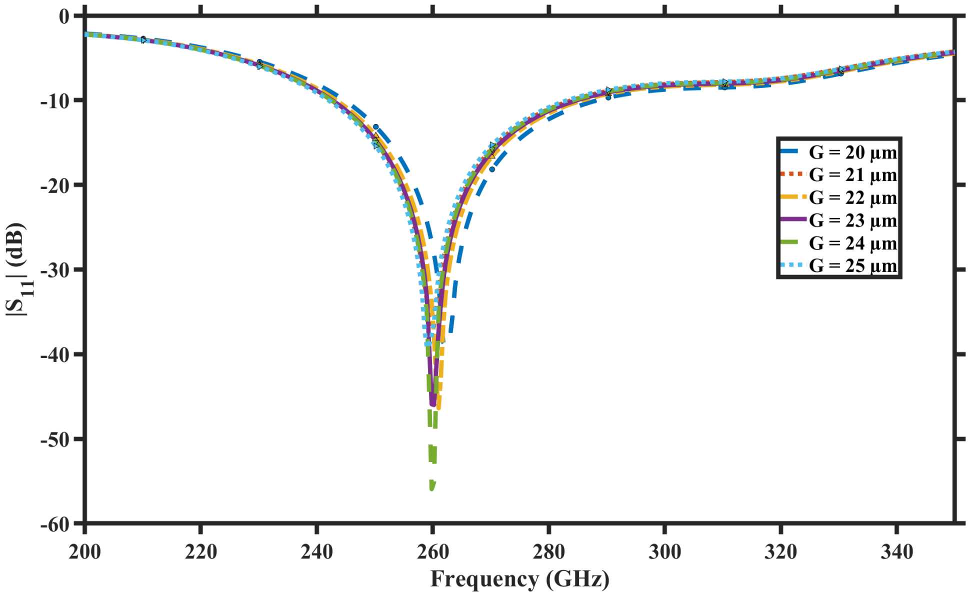

Figure 3.4: S_{11} versus frequency as a function of G

that the substrate thickness below 230 µm shift the resonance towards lower frequencies and above 230 µm towards higher frequency. So, an optimal value of 230 µm balanced the dielectric loading and field confinement. Therefore, selecting an appropriate substrate thickness improves the impedance matching and corrects the minor shift in the resonance.

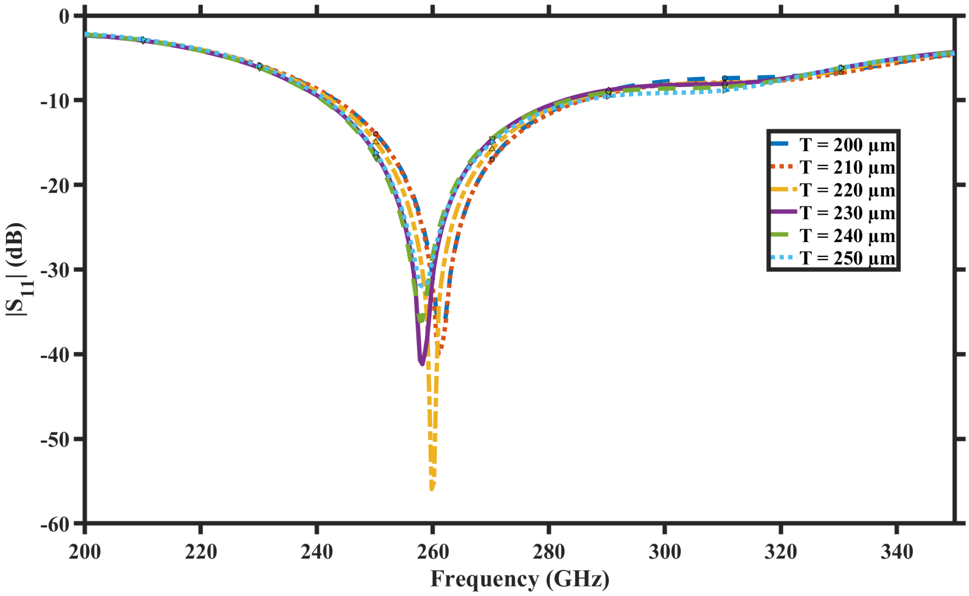

Figure 3.5: S_{11} versus frequency as a function of T

3.4.1 Electric Field Distribution

Figure 3.6 presents the electric field distribution at 260 GHz for the graphene dipole antenna when all the parasitic elements are non-magnetized. As analyzed, the electric field is strongly concentrated along the dipole arms, with the maximum intensity occurring near the dipole arms edges instead of the feed port. This behavior can be explained by the fundamental current and voltage distribution of a resonant dipole antenna. At 260 GHz, standing wave current distribution is supported by the dipole, where the current is maximum at the center and then gradually decreases towards the ends of the arms. The voltage distribution follows the opposite behavior: it is maximum at the feed and maximum towards the open ends. Since the electric field magnetite is directly related to the local charge, accumulation, and voltage distribution, the field intensity increases as we move away from the feeding port toward the ends of the dipole arm. The strong field enhancement near the arm tips corresponds to regions of high charge density caused by the open-circuit boundary condition. This is a classical characteristic of half-wave dipole resonators.

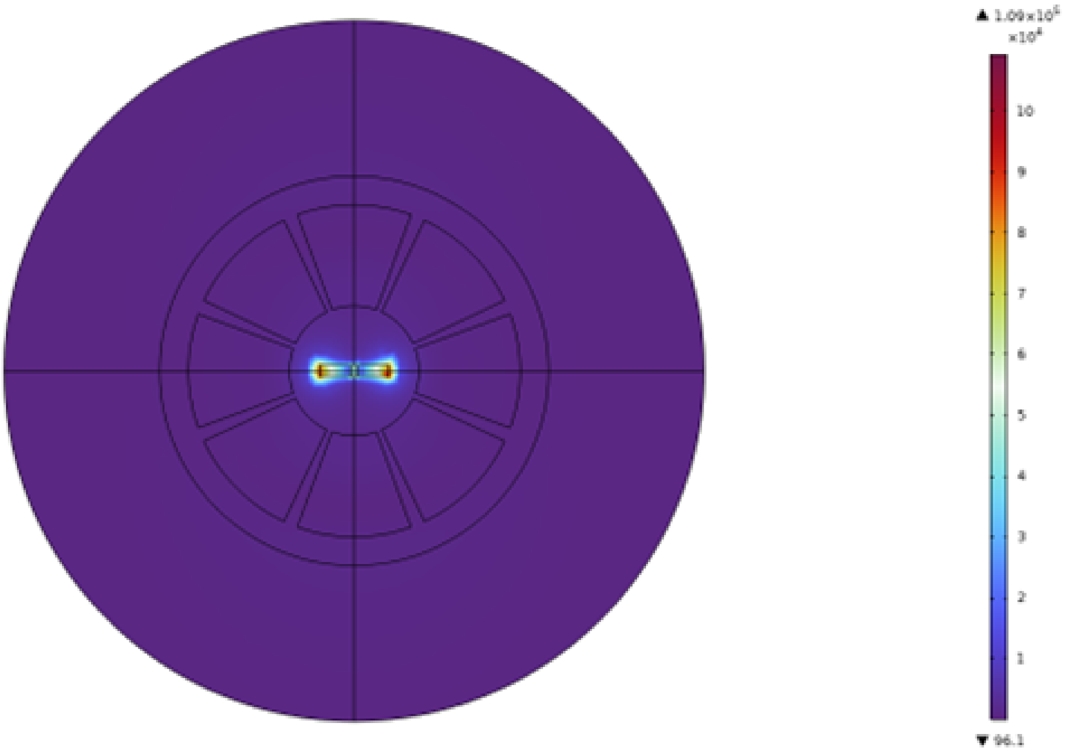

Figure 3.6: Simulated electric field distribution for the dipole at 260 GHz, with non-magnetized parasitic elements

Although the parasitic elements surrounding the dipole are turned off, they do not disturb the near-field distribution in this configuration because they are not electromagnetically excited. In the absence of coupling, the dipole behaves as an isolated resonant radiator, and the field pattern is governed primarily by its intrinsic standing-wave resonance.

The localized high electric field around the dipole arms indicates strong capacitive behavior near the arm extremities. This is particularly important in high-frequency designs, where edge effects and field confinement contribute significantly to radiation efficiency and impedance characteristics.

As shown in Figure 3.7, when a magnetic field (B = 2.5 T) is applied along the x-axis exclusively to parasitic elements 1 and 5 while the dipole remains electrically tuned and not magnetically biased, the electric field distribution along the x-axis exhibits a controlled but largely symmetric perturbation relative to the unbiased case. The x-component is dominating due to the orientation of dipole along the x-axis, and its maximum intensity remains concentrated at the dipole ends because of charge accumulation at 260 GHz. The activation of parasitic elements 1 and 5 changes their surface impedance via anisotropic longitudinal conductivity; but the magnetic field applied is along the x-axis, the induced hall conductivity remains weak and doesn't introduce strong transverse current rotation. As a result, the parasitic elements couple reactively to the near field of the dipole, leading to localized enhancement of electric field in their vicinity without producing pronounced lateral asymmetry. The field contour remains nearly mirror-symmetric about the vertical axis, suggesting that the induced currents on elements 1 and 5 are comparable in magnitude and phase. This inference is further supported by analyzing the simulated surface current distributions, which confirm that the current amplitudes and phases on these elements are nearly identical. Consequently, the electromagnetic response corresponds to moderate reactive loading rather than strong nonreciprocal magnetoplamonic behavior, implying that any beam modification arising from this configuration is primarily due to subtle phase redistribution rather than aggressive directional steering. As shown in Figure 3.8, when a magnetic field is applied on graphene parasitic elements 1 and 5) along the z-axis (out of plane), the electric field distribution exhibits a noticeable different behavior compared to the in-plane magnetization. Because magnetization is perpendicular to the graphene surface, the Hall conductivity terms become significant, introducing strong anisotropy and transverse carrier motion within the biased parasitic elements. This modulates the surface current distribution of the surface not only in magnitude but also in phase, resulting in magetoplasmonic coupling between the driven dipole and the activated parasites. In the Ez plot, the field is strongly concentrated in the dipole also at the center of the parasitic elements 1 and 5, highlighting the interaction of intensified near field. Unlike the nearly symmetric perturbation analyzed under in-plane tuning, the out-of-plane magnetic field produces a more pronounced redistribution of the vertical field component, reflecting the presence of traverse current components induced by the Hall effect. The field contours appear slightly distorted and less

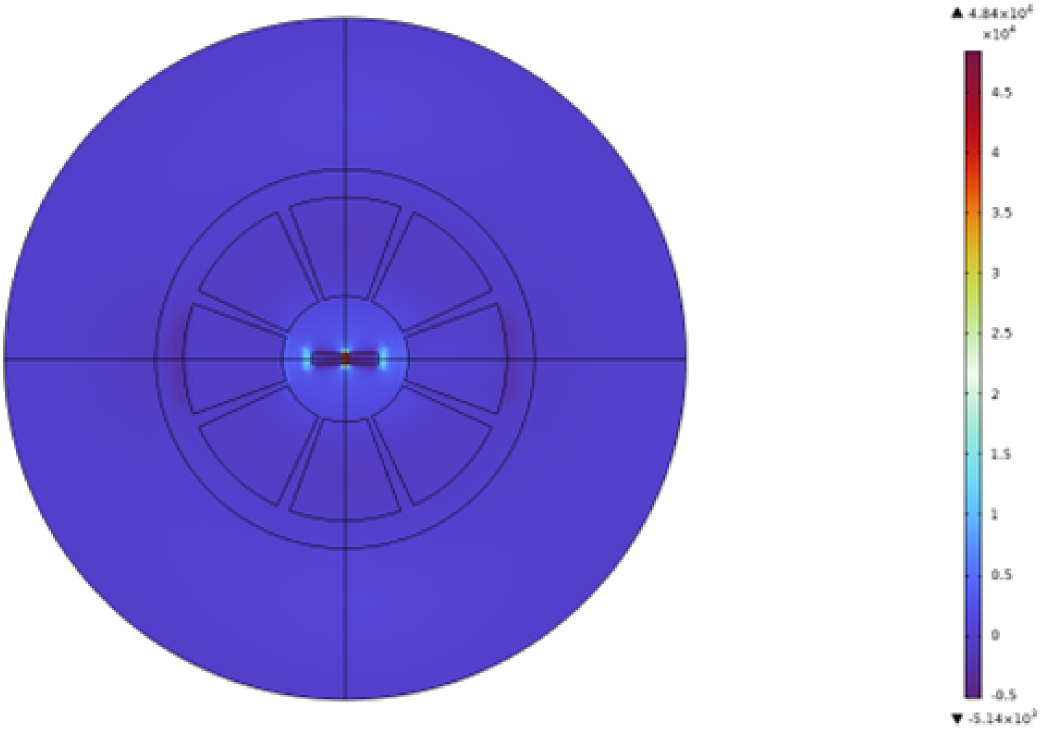

Figure 3.7: Distribution of the x-component of the electric field at 260 GHz for the graphene dipole antenna with an in-plane magnetic field on parasitic elements 1 and 5.

uniformly distributed around the structure, demonstrating that the perpendicular magnetic tuning introduces stronger electromagnetic asymmetry and modifies the reactive and radiative coupling mechanisms. This enhanced coupling is a precursor to more significant beam steering and radiation pattern reconfiguration in the far field, as the altered current phase on the parasitic elements effectively creates a larger phase gradient across the antenna aperture.

In summary, the optimization process involved the tuning of dipole's various parameters including lengths, widths, and gap, to achieve enhanced impedance matching and resonance at 260 GHz. The parametric sweep demonstrated that careful adjustment of these parameters allowed for enhanced near-field coupling between the driven dipole and the parasitic elements, as evidenced by the E_z distributions under both in-plane and out-of-plane magnetic biasing. The resulting configuration exhibits stronger reactive and radiative coupling, more pronounced phase gradients across the antenna aperture, and a field redistribution that directly contributes to beam steering and radiation pattern reconfiguration.

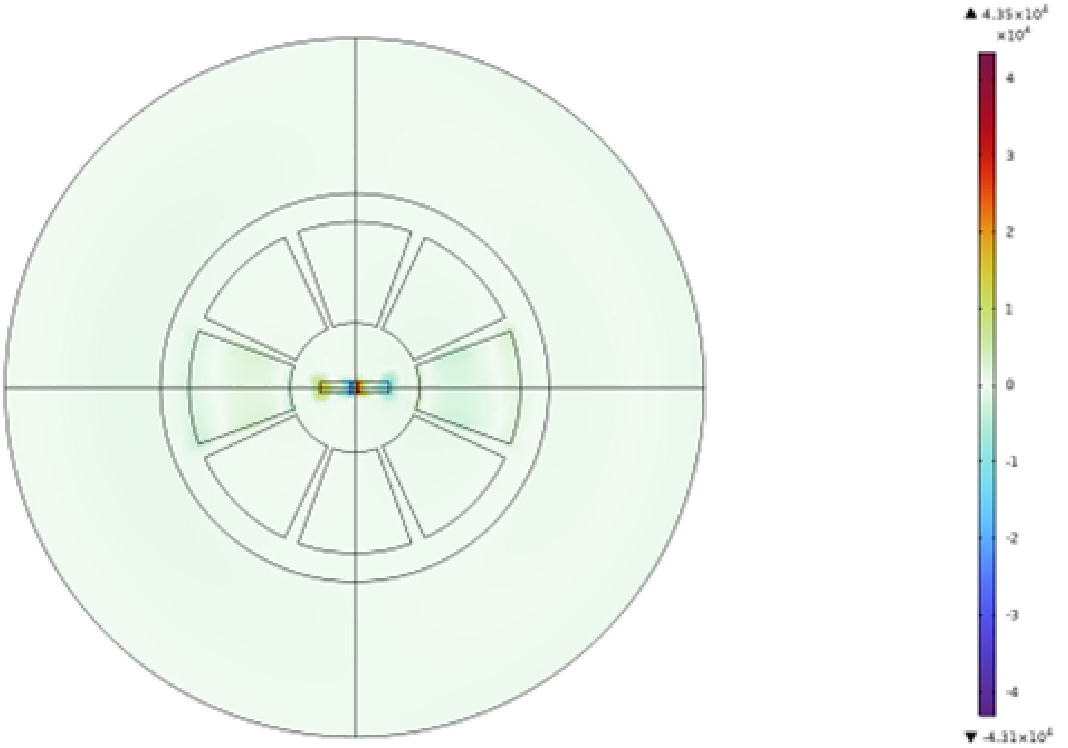

Figure 3.8: Electric field distribution at 260 GHz for the graphene dipole antenna with a 2 T out of magnetic field bias applied to parasitic elements 1 and 5.

3.5 Performance Analysis of In-Plane Magnetic Biasing

The S_{11} parameters were evaluated for various combinations of parasitic elements selective in-plane magnetization. As shown in Figure 3.9, the resonance frequency didn't shift for all configurations; the resonance depth changes according to the activated parasitic elements. This highlights that magnetic biasing mainly influences the impedance matching condition instead of intrinsic resonant modes. Localized anisotropic loading is introduced by the activation of a single parasitic element, modestly enhancing impedance matching. Furthermore, multi-parasitic elements activation improves the redistribution of stored magnetic energy and changes the effective radiation resistance, leading to deeper S_{11} minima. Symmetric multi-parasitic element configurations give the strongest impedance matching enhancement, whereas asymmetric configurations modulate the current imbalance required for the tilting of the radiation beam. Therefore, parasitic element-controlled magnetic bias works as a reconfigurable impedance biasing approach coupled to directional beam control. Figure 3.10 shows the simulated realized gain for different

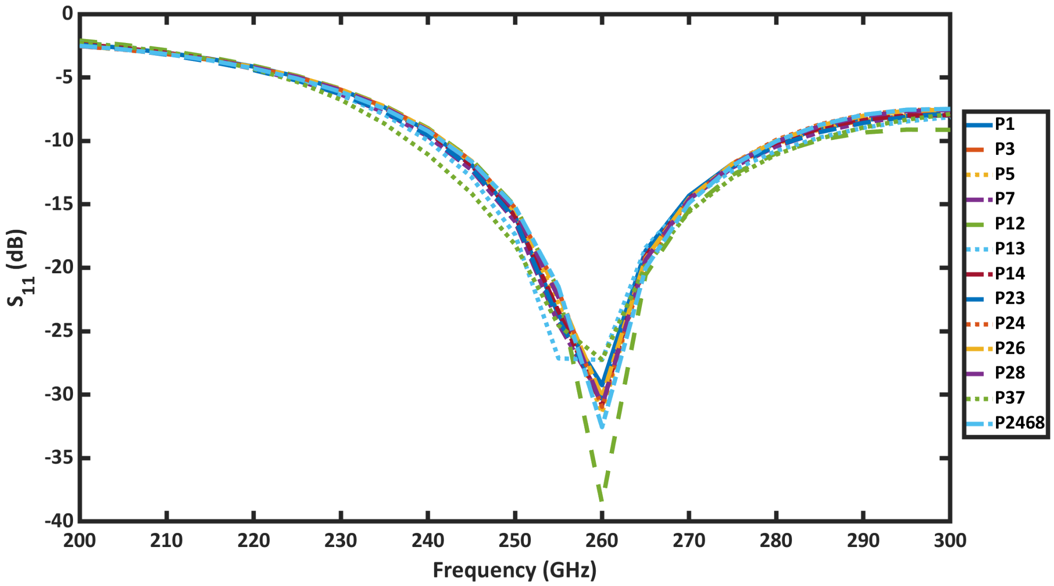

Figure 3.9: Simulated S_{11} as a function of frequency for various combinations of parasitic elements via in-plane magnetization

parasitic elements configurations via in-plane magnetic field. The realized gain integrates both impedance mismatching effects and radiation efficiency and is defined as

$$G_r(\theta, \phi) = \eta_{\text{tot}}\, D(\theta, \phi) \tag{3.7}$$

where $D(\theta, \phi)$ denotes the directivity. The total efficiency is given by

$$\eta_{\text{tot}} = \eta_{\text{rad}} \left(1 - |S_{11}|^2\right) \tag{3.8}$$

Thus, the realized gain relies on radiation efficiency, impedance matching, and angular redistribution of radiated power Across all parasitic configurations, the realized gain increases with frequency and reaches a maximum near the resonance region around 250 GHz to 270 GHz. This behavior is consistent with the antenna approaching the condition where the reactive part of the input impedance vanishes, i.e., $\text{Im}(Z_{\text{in}}) = 0$, and the radiation resistance becomes dominant. The input reflection coefficient S_{11} is given by

$$S_{11} = \frac{Z_{\text{in}} - Z_0}{Z_{\text{in}} + Z_0} \tag{3.9}$$

where Z_0 is the characteristic impedance and Z_{in} is the input impedance perturbed via magnetization. Since the realized gain includes the factor $(1 - |S_{11}|^2)$, configurations exhibiting deeper S_{11} minima correspond to improved impedance matching and enhanced power transfer. Consequently, this results in increased realized gain.

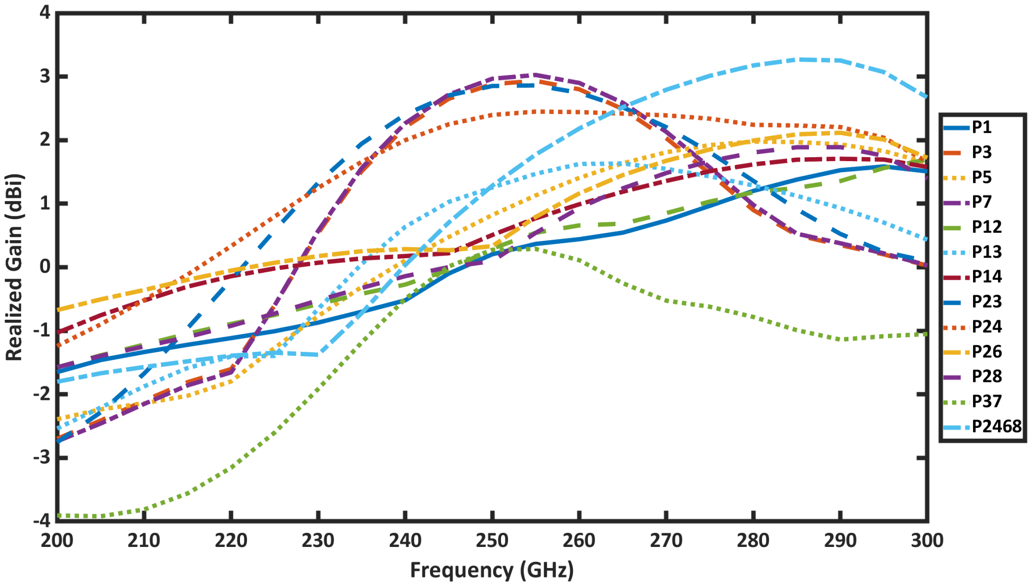

Figure 3.10: Simulated realized gain as a function of frequency for different parasitic combinations

The use of an in-plane magnetization changes the constitutive parameters of the biased parasites. Under magnetization, permeability becomes gyrotropic and mathematically written as

$$\mu = \begin{bmatrix} \mu & j\kappa & 0 \\ -j\kappa & \mu & 0 \\ 0 & 0 & \mu_z \end{bmatrix} \tag{3.10}$$

where k represents the magnetically induced coupling term. The non-reciprocal coupling between orthogonal field components is introduced by the off-diagonal components, leading to phase propagation depends on direction and asymmetric current redistribution.

Single parasitic element configurations such as P1 and P5 exhibit relatively low realized gains of 0.4 dBi and 1.4 dBi, respectively, whereas P3 and P7 obtain the same realized gain of 2.8 dBi. Among the dual-parasitic elements configurations, P23 and P24 provide a realized gain of 2.4 dBi and 2.8 dBi, respectively. Other dual configurations such as P12, P14, and P26 produce realized gains of 1 dBi, 1.1 dBi, and 2.8 dBi, respectively. Meanwhile, P13 and P28 yield realized gains of 1.8 dBi and 2.8 dBi, respectively. Finally, the P2468 configuration obtains a realized gain of 2.1 dBi. In this case, the distributed multi-parasitic element bias exhibits modal symmetry while enhancing impedance matching and radiation efficiency. Because the perturbation is more uniformly distributed, destructive interference is minimized and directivity is improved.

In contrast, the P37 combination demonstrates reduced gain across the band, especially below 260 GHz, which highlights that opposing parasitic bias introduces a strong azimuthal phase imbalance, enhancing stored reactive energy instead of radiated energy. As a result, the radiation efficiency decreases and the realized gain is suppressed.

Overall, the results indicate that the selection of parasitic elements via in-plane magnetic field acts as a reconfigurable control approach that simultaneously affects impedance matching and radiation efficiency and radiation directivity. While the fundamental resonance frequency remains nearly constant, the redistribution of current density and induced phase gradients enable dynamic gain enhancement or suppression depending on the activated parasitic element combination. By organizing the results according to single, dual, and multi-parasitic configurations, it becomes clear that symmetrically distributed activations consistently improve impedance matching, reduce destructive interference, and enhance gain, providing an understanding of how the selection of parasitic elements govern beam shaping and efficiency.

Figure 3.11 represents the total efficiency of the proposed graphene dipole antenna as a function of frequency for various parasitic element combinations via in-plane magnetic bias and was defined in eq. (6.7). Efficiency incorporates the effects of impedance mismatch and dissipative losses. Changes among parasitic states thus reflect variations in radiation resistance, stored reactive energy, and matching conditions introduced by the magnetic bias. At the lower band (200-230 GHz),

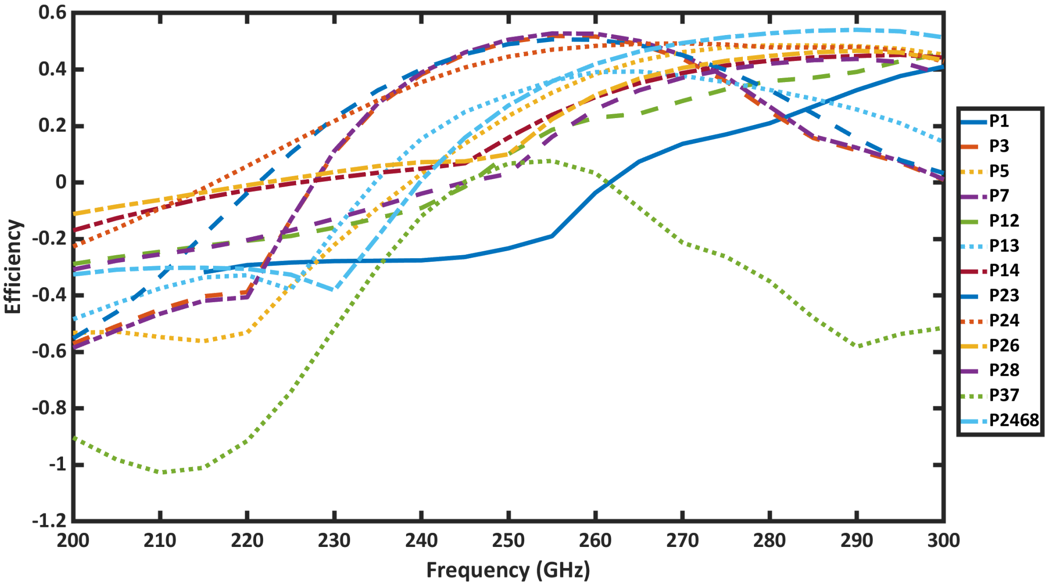

Figure 3.11: Simulated efficiency as a function of frequency for different parasitic combinations

most combinations exhibit negative values in the plotted scale, highlighting poor radiation efficiency and strong reactive energy below resonance. In this region, the antenna operates in an inductive regime where

$$Z_{\text{in}} = R_{\text{rad}} + R_{\text{loss}} + jX \tag{3.11}$$

with $|X| \gg R_{\text{rad}}$, resulting in weak radiation and strong reflection. The P37 combination demonstrates the most severe degradation, reaching the lowest efficiency, which highlights that opposite parasitic magnetic bias introduces strong azimuthal phase imbalance, resulting an increase of stored magnetic energy instead of power radiation, thus reducing both radiation efficiency and impedance matching.

As the frequency approaches resonance, the reactive component becomes zero and radiation resistance dominates. In this region, several combinations such as P7, P24, P23 and P28 exhibit pronounced efficiency enhancement, exceeding 45-50%. This highlights that parasitic element magnetic bias redistributes surface current in a manner that increases radiation resistance while simultaneously enhancing impedance matching. Since the realized gain depends on η_{tot}, these combinations correspond to the higher gain values observed previously.

The combination P3 exhibits an efficiency of 52%, while P1 shows a negative efficiency value. P5 state achieves an efficiency of 38%. Among the multi-parasitic element cases, P12 provides 22% efficiency, P13 reaches 38%, and both P14 and P25 demonstrate efficiencies of 30%. Finally, P2468 combination exhibits an efficiency of 41%, indicates that distributed multiparasitic element magnetic bias maintains modal symmetry while reducing mismatch losses. Because the perturbation is more spatially uniform, destructive interference is minimized and radiation efficiency remains high.

Overall, the efficiency curves confirm that parasitic element selection through in-plane magnetization acts as a reconfigurable mechanism that controls both radiation efficiency and impedance matching. Combination that preserves modal symmetry while introducing controlled current redistribution enhances total efficiency, whereas opposing parasitic element bias generates phase imbalance and reactive energy storage, leading to reduced radiative performance. In-plane magnetic bias provides an effective and flexible mechanism for controlling the electromagnetic behavior of the graphene antenna. By selectively activating parasitic elements, it is possible to tune impedance matching, redistribute surface currents, and introduce controllable phase gradients across the structure. Configurations that maintain symmetry improve radiation efficiency and realized gain, while asymmetric biasing enables beam shaping via controlled phase imbalance.

3.6 In-Plane Magnetic Field-Induced pattern reconfiguration

Figure 3.12(a-d) presents the realized far-field radiation patterns for parasitic element in-plane magnetic field applied to parasites P1, P3, P5, and P7, respectively. In the unbiased case, the dipole exhibits mirror symmetry and generates a conventional bi-directional broadside pattern centered around $\theta_0 = 90°$. When an off-axis magnetic field is applied to an individual parasitic element, the constitutive parameters become anisotropic and gyrotropic.

For parasitic element P1, shown in Figure 3.12a, the magnetic bias breaks the left-right symmetry of the dipole current distribution. The induced surface current density J(r) becomes stronger and phase-advanced on the biased side. Since the far field is determined by

$$\mathbf{E}_{\text{far}}(\theta, \phi) \propto \int_V \mathbf{J}(\mathbf{r})\, e^{jk\hat{\mathbf{r}}\cdot\mathbf{r}}\, dV \tag{3.12}$$

Any symmetry in amplitude or phase directly modifies the angular interference condition. The result is a clear beam tilt towards P1, where constructive interference is enhanced and the radiation maximum shifts from the symmetric broadside direction.

In the case of P5, the magnetic bias is applied to the opposite side of the structure, as shown in Figure 3.12b. Consequently, the direction of the induced phase gradient reverses. The reverse phase imbalance $\Delta\phi(y) \neq 0$ now favors constructive interference on the opposite azimuthal side, producing a beam tilt toward P5. The radiation pattern appears as a mirrored version of the P1 case, confirming that the beam direction is controlled by the spatial location of the magnetic perturbation.

For P3, depicted in Figure 3.12c, the magnetic bias is applied along a different azimuthal orientation relative to the feed axis. In this combination, the perturbation introduces a dominant transverse phase component that makes one lobe of the pattern towards 270° and the other to be ceased due to destructive interference. The redistribution of reactive near-field energy produces a stronger directional symmetry as compared to P1 and P5, highlighting that the induced phase gradient aligns more efficiently with the dominant current path of the dipole, resulting in a more pronounced unidirectional characteristic.

Similarly, P7, illustrated in Figure 3.12d, produces a complementary steering effect. The gyrotropic coupling alters the local propagation constantly and creates an effective transverse wavevector component opposite that in P3. As a result, the maximum radiation shifts towards 90°, demonstrating controllable beam rotation via parasitic selection.

Physically, the beam tilt can be interpreted as effective phase steering and introducing a transverse phase gradient modifies the constructive interference condition from ($\theta_0 = 90°$) to ($\theta_0 = 90° + \Delta\theta$), where $\Delta\theta$ is proportional to the magnetically induced phase imbalance governed by k. The magnitude and direction of the tilt depend on which parasitic element is biased, confirming that the maximum radiation follows the spatial location of the anisotropic perturbation. Figure 3.13 shows simulated radiation patterns for various combinations of magnetically biased parasitic elements. Each subplot illustrates how selective magnetic activation redistributes surface currents and produces controlled beam steering via gyrotropic anisotropy.

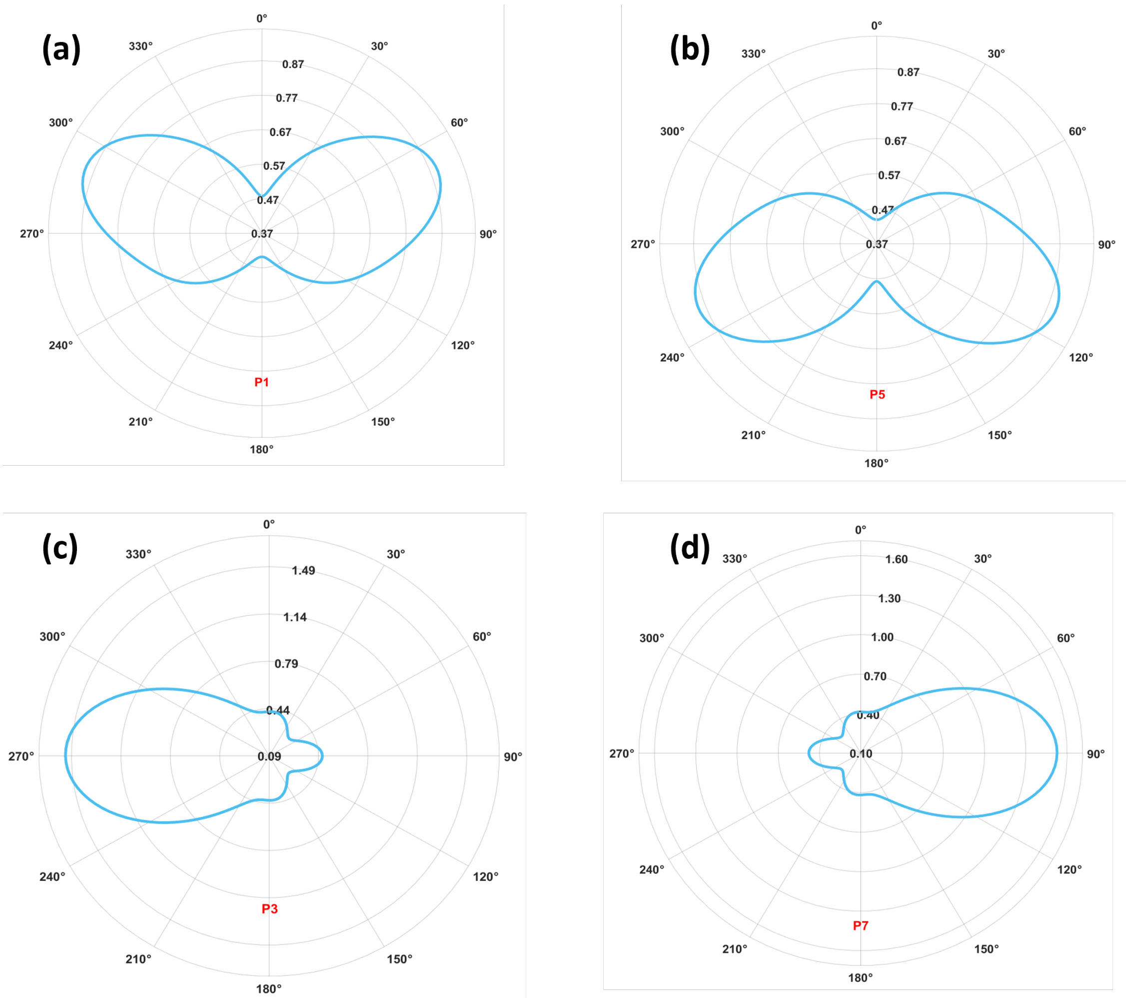

Figure 3.12: Simulated beam steering at 260 GHz under in-plane magnetic bias: (a) magnetic field applied to P1, (b) P5, (c) P3, and (d) P7

In Figure 3.13a, where P12 is biased, the radiation patterns become asymmetric with multiple lobes. The main lobe is directed towards the activated parasites, whereas secondary lobes appear due to partial phase imbalance across adjacent parasites. The beam deviation is noticeable but not highly directive, highlighting moderated anisotropic perturbation. Figure 3.13b shows that biasing P13 results in stronger front-to-back asymmetry. The main lobe shifts more distinctly toward the

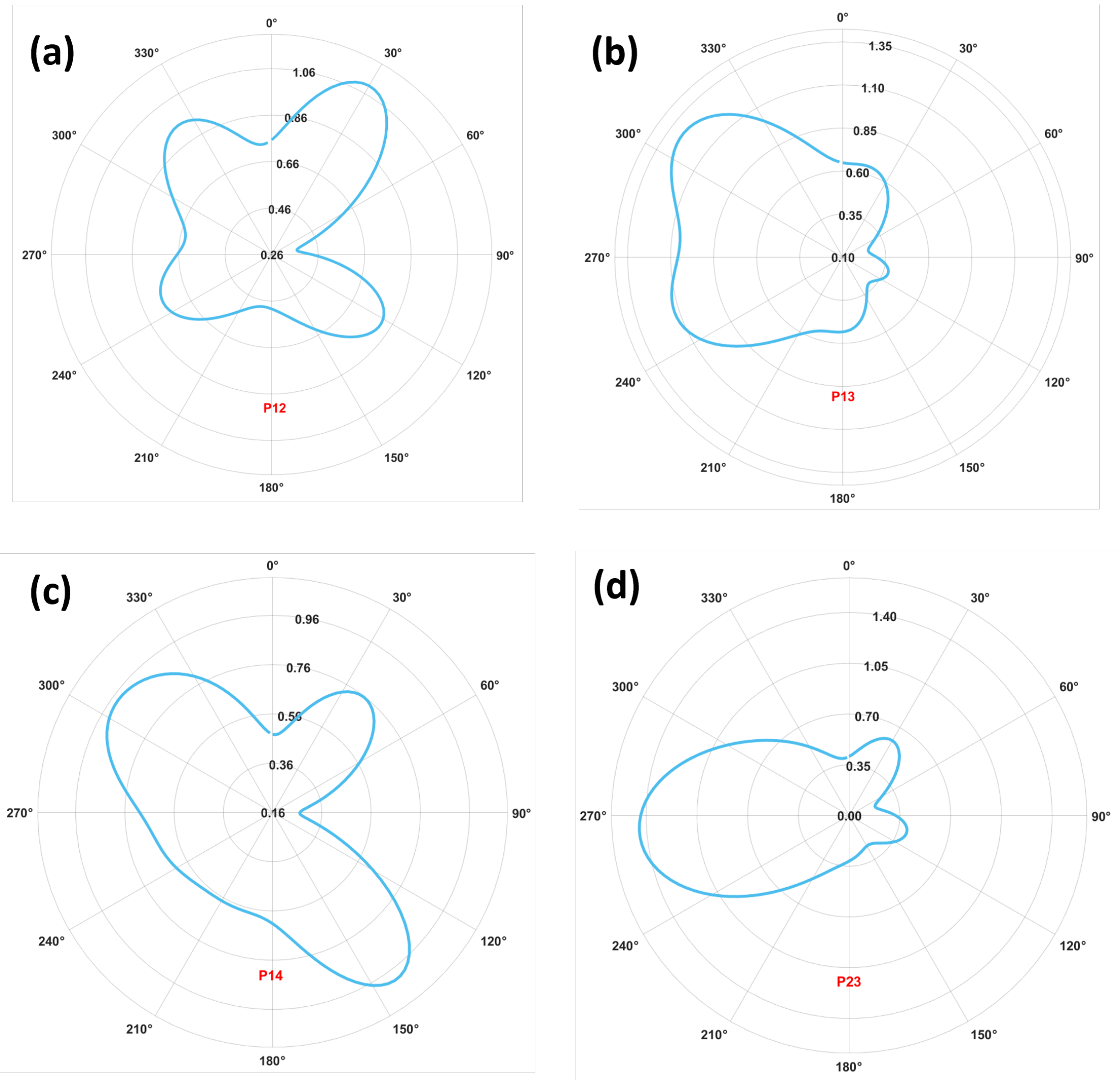

Figure 3.13: Simulated radiation patterns for the activation of dual parasitic element combinations. (a) P12, (b) P13, (c) P14, and (d) P23

biased region, and the side lobe levels increase on the opposite side. This suggests enhanced non-reciprocal phase accumulation, generating a clearer steering effect compared to P12.

In Figure 3.13c, activating P14 produces a more pronounced multi-lobed structure. Two dominant lobes appear, highlighting strong interference between the adjacent parasitic element currents. The radiation tilt is larger, demonstrating that this parasitic position induces stronger coupling with the dominant dipole mode.

In Figure 3.13d, where P2 and P3 are simultaneously biased, the radiation pattern becomes significantly directional. A dominant single main lobe appears with suppressed back radiation. The combined magnetic bias improves constructive interference in one angular direction while destructively interfering elsewhere, leading to higher directivity and improved beam steering performance.

Figure 3.14 demonstrates the radiation pattern for the activation of additional dual parasitic element combinations: (a) P24, (b) P26, (c) P28, and (d) P37. These combinations further demonstrate how different spatial distributions of magnetic bias control the radiation symmetry, lobe formation, and beam direction.

In Figure 3.14a, the pattern exhibits a dominant main lobe directed approximately towards 270°, with one weaker side lobe. The symmetric distribution highlights constructive interference along one transverse direction and partial destructive interference elsewhere. The beam tilt is pronounced, suggesting strong phase imbalance between the activated parasites and the remaining structure.

The radiation becomes multi-lobed with comparable lobe amplitudes in several angular directions, as illustrated in Figure 3.14b. The presence of three significant lobes highlights coupling between non-adjacent parasites. This combination produces distributed radiation rather than a single highly directive beam, implying weaker spatial coherence compared to P24.

In Figure 3.14c, the pattern evolves toward a more symmetric four-lobed structure. The lobes are more evenly spaced, highlighting balanced excitation of higher-order modes. This suggests that the selected sectors generate a more periodic current redistribution, reducing dominant beam steering but enhancing angular coverage.

In Figure 3.14d, the radiation becomes strongly bidirectional, with two dominant opposite lobes near 90° and 270°. Back radiation is significantly reduced between these lobes, and smaller ripples appear due to residual higher-order mode contributions. This behavior highlights that activating P3 and P7 introduces near-symmetric phase opposition, producing a directional dual beam response.

Overall, these results present that increasing spatial separation or symmetry between activated parasitic elements modifies interference conditions. Adjacent-parasitic element combinations (e.g., P24) favor single beam steering, while symmetric or widely separated parasitic elements (e.g., P28 and P37) promote multi-lobed or bidirectional radiation, which confirms that parasitic element-selective magnetic biasing enables flexible radiation reconfiguration by controlling phase gradients and modal distribution across the structure. Figure 3.15 presents the radiation pattern for the P2468 combination, where four alternating parasitic elements (P2, P4, P6 and P8) are simultaneously magnetically biased. This symmetric and periodic activation strongly modifies the current distribution across the structure and excites higher-order angular modes. The radiation pattern exhibits a clear four-lobed structure, with two dominant lobes around approximately 150° and 210°, and two additional side lobes near 30° and 330°. The near-symmetric distribution about the vertical axis highlights that the magnetic bias is applied in

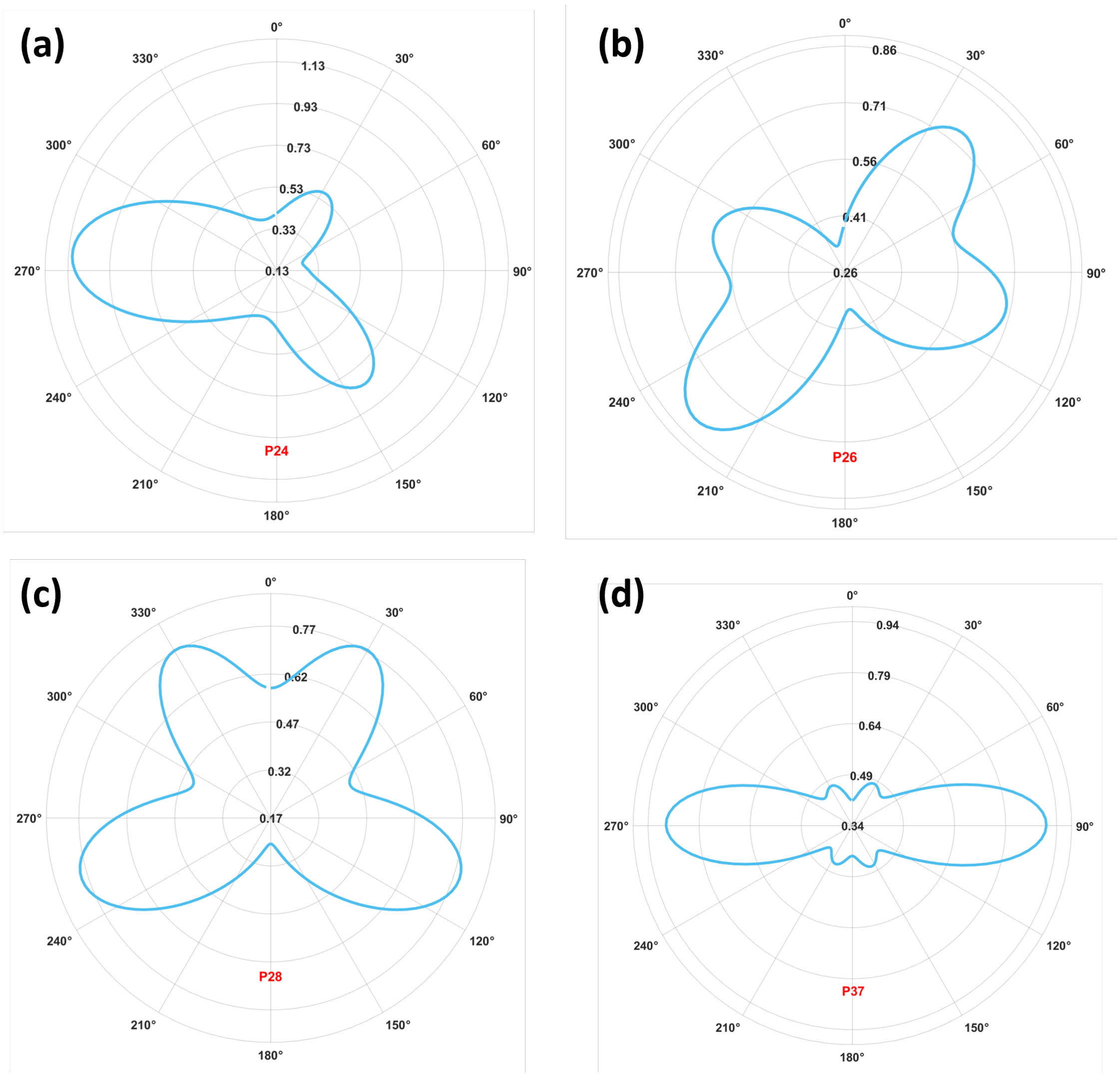

Figure 3.14: Simulated radiation patterns for the activation of dual parasitic element combinations. (a) P24, (b) P26, (c) P28, and (d) P37

a spatially periodic manner, creating a balanced phase modulation across the circumference. Compared to single or dual parasitic element activation, this combination reduces single-direction beam steering and instead promotes multi-directional radiation. The alternating parasitic element bias introduces a periodic phase variation around the structure, which can be interpreted as an angular phase function ($\phi(\theta) = \phi_0 + m\theta$), where m denotes a higher-order azimuthal mode number. As a result, constructive interference occurs at multiple angular positions, forming dual main lobes rather than a single steered beam.

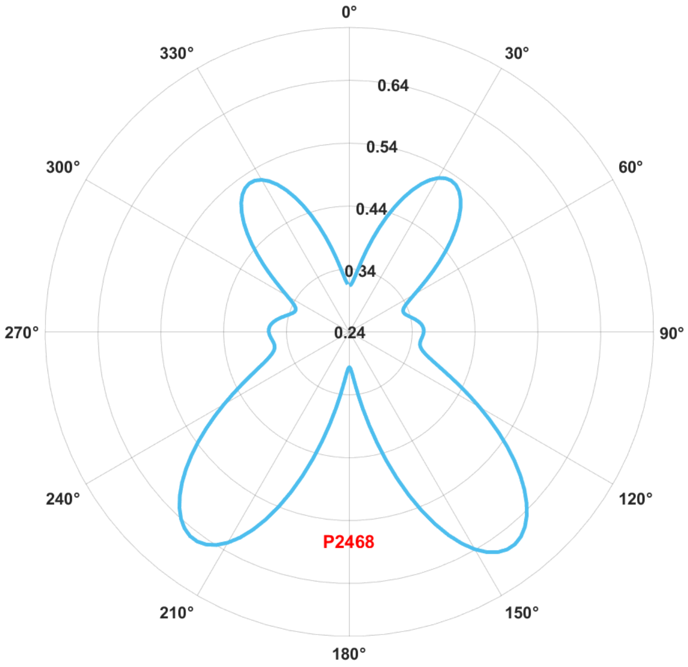

Figure 3.15: Simulated radiation of P2468 combination, where alternating parasitic elements (P2, P4, P6 and P8) are simultaneously biased via in-plane magnetization

3.7 Performance Analysis of out-of-Plane Magnetic Biasing

Figure 3.16 presents the simulated S_{11} parameters for the activation of various parasitic elements combinations when a magnetic field is applied along the z-axis. In contrast to the magnetic field along the x-axis, the magnetic field is now normal to the plane of antenna, modifying the effective permeability primarily along the perpendicular direction.

It is analyzed that all parasitic elements combinations exhibit a well-defined resonance at 260 GHz. The resonance depth reaches the value between -25 dB and 42.5 dB relying on the activated parasitic combination, highlighting excellent impedance matching under magnetic field applying along z-axis. The small variation in the resonance frequency across the activation of various parasitic elements suggests that the normal magnetic bias doesn't significantly disturb the in-plane current distribution responsible for resonance formation.

Compared to the magnetization along the x-axis, where stronger anisotropic coupling could induce resonance shifts, the magnetic field along the z-axis produces only small frequency deviations. This behavior can be explained by the permeability tensor under normal magnetization, where the dominant in-plane components remain nearly symmetric and the off-diagonal gyrotropic terms couple less effectively to the transversely dipole currents. As a result, the effective inductance and capacitance of the antenna are only weakly perturbed, maintaining a stable resonant frequency. The differences in minimum S_{11} levels among combinations such as P1, P3, P23, P24, P37 and P2468 highlight that parasitic activation still slightly changes the stored magnetic energy and local current density. However, these changes mainly impact matching depth instead of resonance position. Combinations involving multiple adjacent parasitic elements tend to exhibit deeper nulls, suggesting improved impedance matching due to more uniform magnetic loading.

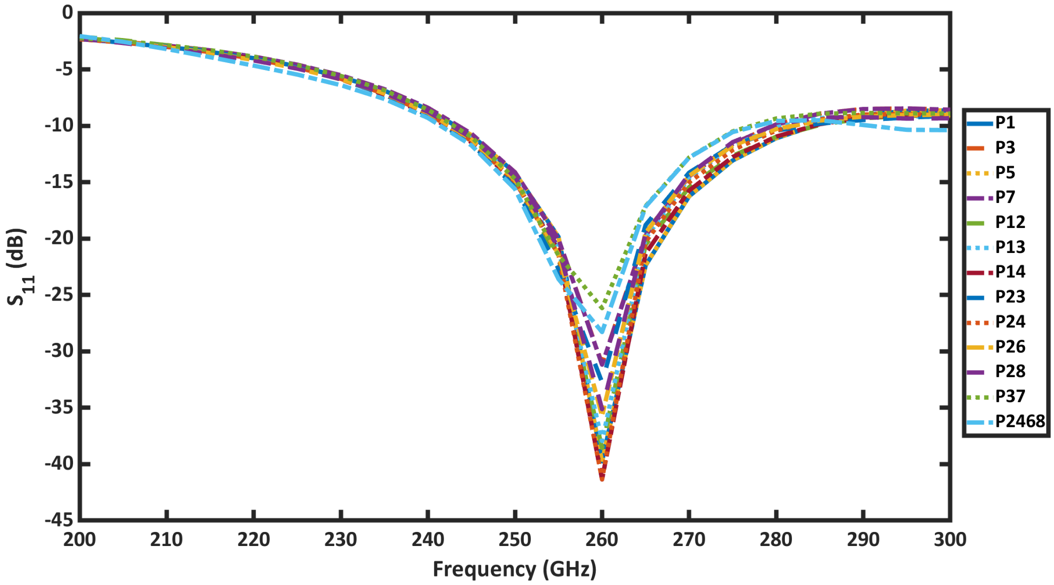

Figure 3.16: Simulated S_{11} as a function of frequency for various combinations of parasitic elements via in-plane magnetization

Overall, this plot demonstrates that out-of-plane magnetic bias preserves the intrinsic resonance frequency of the antenna while allowing moderate tuning of impedance matching quality. Unlike in-plane magnetization, it doesn't strongly shift the resonance but instead provides a more stable and symmetric electromagnetic response. This confirms that resonance tuning is highly sensitive to the direction of magnetization and that perpendicular magnetic bias mainly influences matching rather than reactive resonance control.

Figure 3.17 shows the realized gain for the combinations of different parasitic element sector activation when an out-of-plane magnetization is applied. Unlike the in-plane magnetization case, where strong anisotropic coupling induces beam tilting and resonance shift the perpendicular magnetic bias primarily influences the overall radiation strength while preserving resonance stability.

It is analyzed that the realized gain gradually increases with frequence for all sector configuration reaching a maximum in the vicinity of 260-275 GHz which corresponds to the -10 dB impedance bandwidth identified in the S_{11} plot. Below resonance (200-300 GHz), the gain remains negative or low (-3 dBi to -1 dBi), highlighting inefficient radiation due to reactive energy storage. As the frequency approaches resonance, the radiation efficiency improves, and the realized gain increases accordingly. Among the various combinations, P24 exhibits the highest peak realized gain, exceedingly approximately 4 dBi near 260 GHz, suggesting that activating this sector under perpendicular magnetic biasing improves constructive radiation and improves effective aperture utilization. Combinations such as P23 and P2468 also exhibit relative high peak gain indicating that multi sector activation can improve radiation coupling even under out of plane magnetization

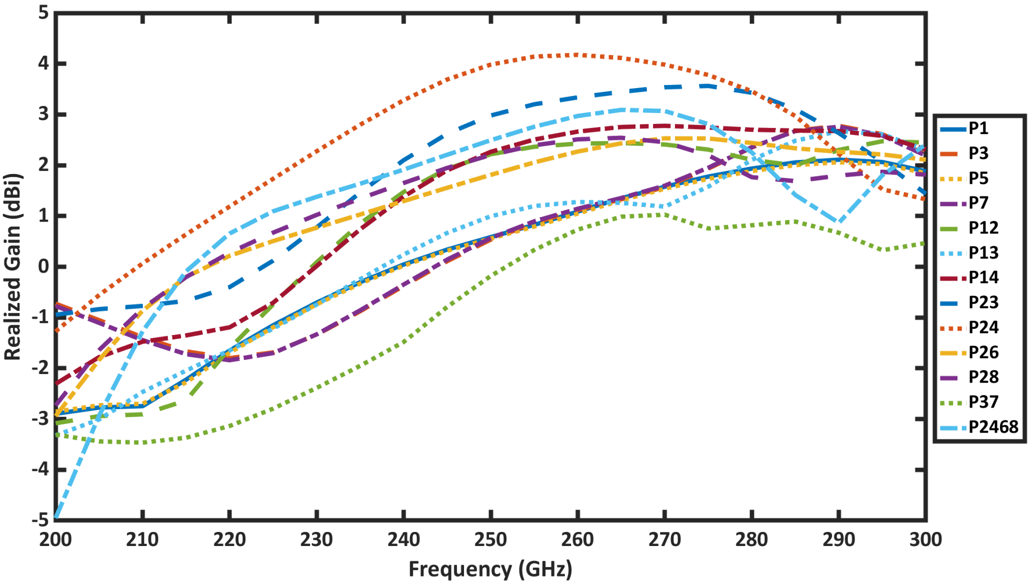

Figure 3.17: Simulated realized gain as a function of frequency for different parasitic combinations under out-of-plane magnetization

Single sector cases (P1, P3, P5, P7) and certain distribution combinations such as P37 show comparatively lower peak gains, generally in the range of 1-2.5 dBi, highlighting that localized magnetic loading changes current distribution but does not significantly enhance directivity under perpendicular bias.

Importantly the overall realized gain variation across combinations is moderate compared to the in-plane magnetic bias scenario, confirming that out-of-plane magnetic bias does not strongly induce transverse phase gradients responsible for beam steering. Instead, it mainly varies the magnitude of the radiated power by slightly modifying current density distribution and stored magnetic energy.

The correlation between the realized gain peaks and the S_{11} minima further confirms that enhanced impedance matching results in improved radiation performance near resonance. Since the resonance frequency remains relatively stable across parasitic element combinations, the realized gain maxima also occur within a narrow frequency band.

Overall, the results reveal that out-of-plane magnetic bias preserves resonance stability while allowing moderate tuning of radiation direction but instead influence gain enhancement through controlled magnetic loading of selected parasitic elements. This indicates the directional sensitivity of magnetic field orientation in governing radiation reconfigurability and performance optimization.

The radiation efficiency as a function of frequency (200-300 GHz) for the activation of different parasitic element combinations under out-of-plane magnetization is presented in Figure 3.18. The results show a consistent frequency-dependent improvement in efficiency for all combinations, with notable differences in magnitude and stability depending on the activated parasitic elements. At lower frequencies (220-240 GHz), the radiation efficiency is negative for most combinations, highlighting that a significant portion of the accepted power is dissipated or stored reactively rather than radiated. This behavior corresponds to the off-resonance region, where impedance mismatch and stored magnetic energy dominate. Among all cases, combination P37 exhibits the lowest efficiency in this region, reaching approximately -0.7 around 240 GHz, demonstrating stronger reactive loading and higher loss contribution when these opposite parasitic elements are activated.

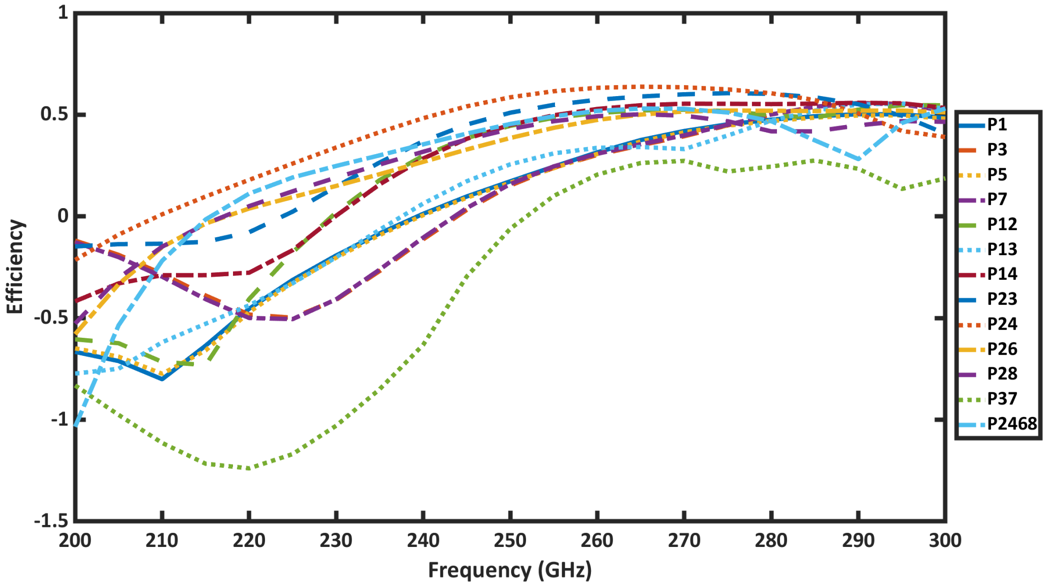

Figure 3.18: Simulated efficiency as a function of frequency for different parasitic combinations under out-of-plane magnetization

As the frequency increases toward 240-260 GHz, efficiency rises steadily for all combinations. This improvement coincides with the resonance region observed in the S_{11} characteristics The enhanced impedance matching at resonance reduces reflected power and increases the fraction of radiated energy and round 260-275 GHz, most combinations achieve their maximum efficiency values.

Among the dual-parasitic elements combination, P24 provides the highest peak efficiency, exceedingly 0.5 near 260-270 GHz, whereas combinations P23, P14, and P2468 also show relatively high efficiencies, generally in the range of 0.4-0.5. This highlights that activating symmetrically distributed adjacent parasitic elements under normal magnetic bias promotes enhanced distribution and reduced dissipative losses, thereby improving radiation efficiency.

Single-parasitic element combinations (P1, P3, P5, P7) show moderate peak efficiencies around 0.35-0.4 at higher frequencies. Although their efficiency enhances near resonance, the improvement is slightly lower compared to optimized dual- or multi-parasitic elements combinations, demonstrating that isolated magnetic loading does not fully utilize the available radiating aperture.

Combination P37 remains comparatively lower in efficiency across the entire frequency range, even at resonance, where it reaches only about 0.1-0.15, which implies that this parasitic element arrangement introduces non-uniform current distribution and additional internal losses under out-of-plane magnetization.

Beyond 280 GHz, the efficiency curves tend to saturate or slightly decline, indicating operation beyond the optimal resonance region. The relatively small spread in peak efficiency values compared to the in-plane magnetization case confirms that out-of-plane magnetization mainly effects the magnitude of radiated power rather than modulating the induced anisotropic effects or beam steering.

Overall, the results show that under out-of-plane magnetic bias, radiation efficiency is mainly governed by resonance quality and sector symmetry. Multi-parasitic element symmetric combination provides improved efficiency due to better current balance and reduced reactive energy storage, while asymmetric or widely separated parasitic elements activations lead to reduced radiation performance.

The simulated radiation patterns for the activation of single parasitic elements P1, P3, P5, and P7 under out-of-plane magnetic field are shown in Figure 18. The plots evidently display that activating various individual parasitic elements generates distinct beam orientations and asymmetrical radiation distributions, confirming that the radiating behavior is strongly dependent on the parasitic element position.

For the P1 combination (Figure 3.19a), the radiation pattern exhibits dual beams orientated towards 60° and 300° direction. This highlights that activating P1 introduces an asymmetric current distribution that favors radiation in the upper-right quadrant relative to the antenna center. In the case (Figure 3.19b), the radiation pattern is oriented towards -150° with a secondary lobe around 270°. The pattern becomes more skewed, showing stronger directivity in the lower-left

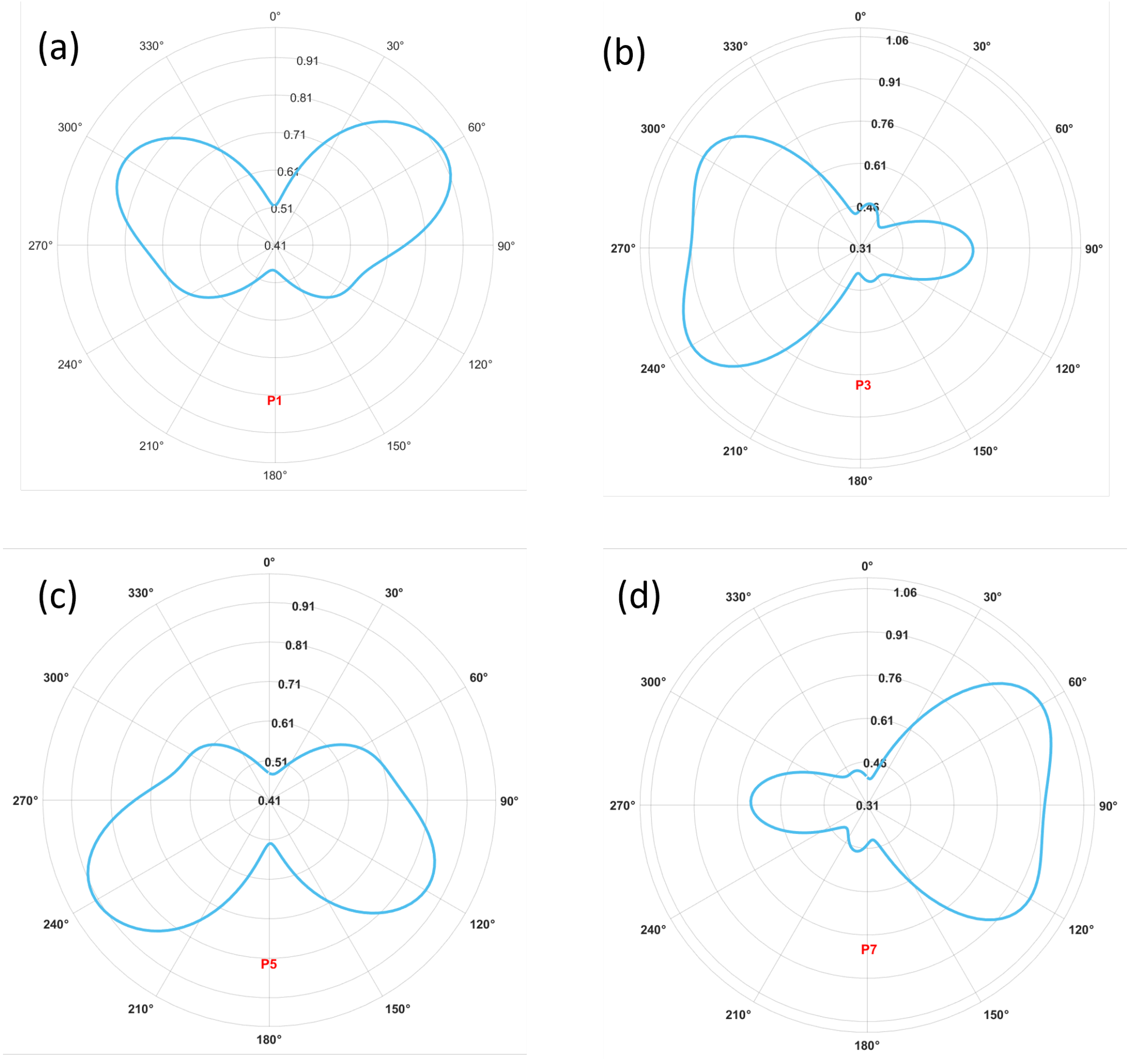

Figure 3.19: Simulated beam steering at 260 GHz under out-of-plane magnetic bias: (a) magnetic field applied to P1, (b) P5, (c) P3, and (d) P7

quadrant, confirming that changing the activated parasites effectively rotates the current concentration region, resulting in beam steering.

For P5 activation (Figure 3.19c), the radiation pattern is again rotated relative to P1. Compared to P3, the pattern shows a slightly more balanced distribution between the two lobes, although the radiation remains clearly directional rather than omnidirectional.

In Figure 3.19d, the beam orientation in the P7 combination rotates to 180° with the main lobe directed towards 60°-80° and the secondary lobe near 90°. The radiation direction appears somewhat more distorted compared to P1 and P5, suggesting stronger phase non-uniformity when this parasitic element is activated.

Overall, the results display a systematic rotation pattern corresponding to the angular position of the activated parasitic elements. Each single parasitic element excitation generates an asymmetric current distribution that produces a tilted beam. The approximate 90° spatial separation among P1, P3, P5 and P7 results in corresponding beam reorientation in the far-field domain, confirming that selective parasitic element activation provides effective beam steering capability without altering the physical geometry of the antenna.

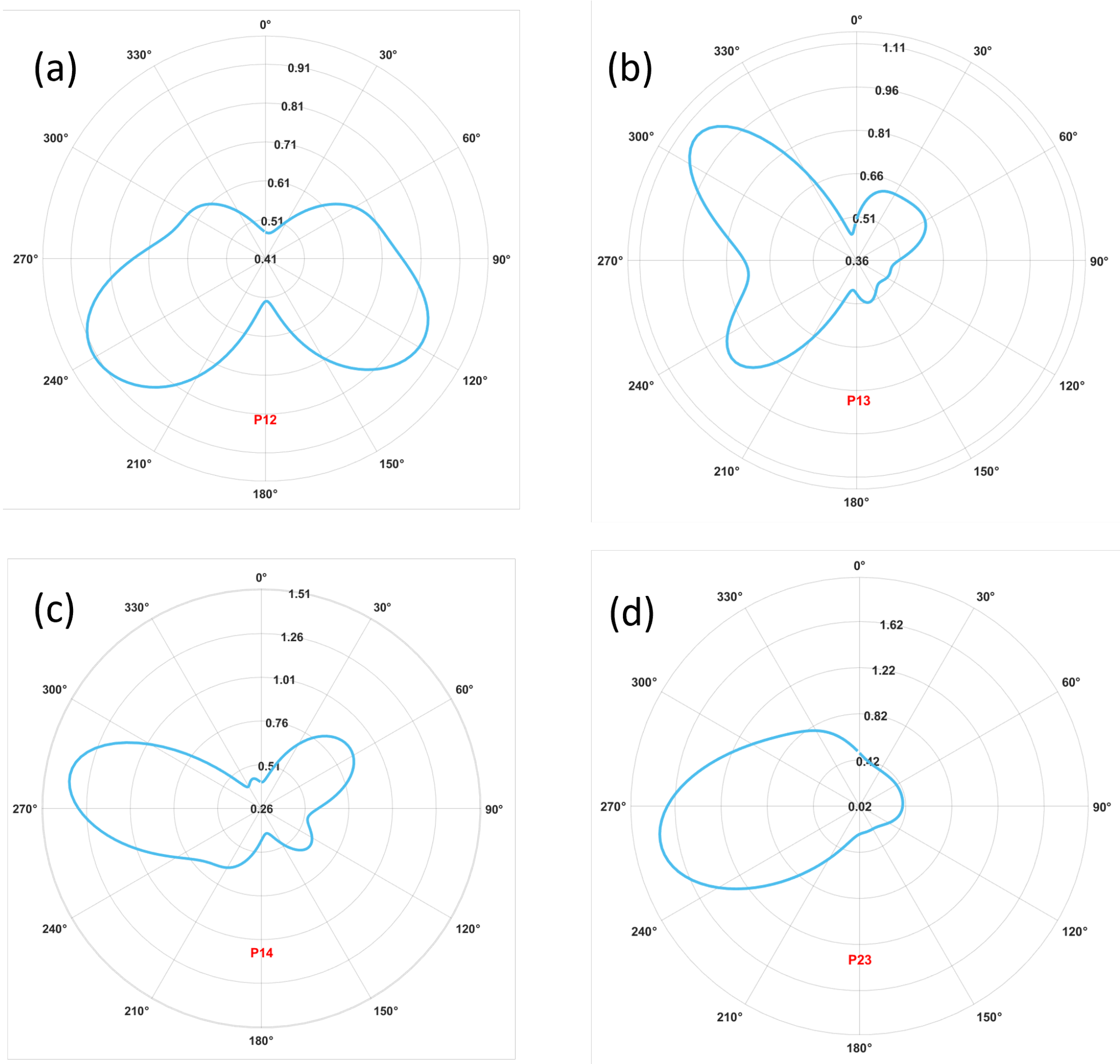

Figure 3.20: Simulated radiation patterns for the activation of dual parasitic element combinations under out-of-plane magnetization. (a) P12, (b) P13, (c) P14, and (d) P23

The radiation patterns for activating various parasitic elements combinations are depicted in Figure 3.20. The radiation for dual parasitic element combinations P12, P13, P14, and P23 under the applied out-of-plane magnetics bias compared to the single parasitic element cases the dual parasites combination exhibit stronger directivity and more pronounced beam shaping due to enhanced current redistribution and constructive interference between adjacent or separated sectors.

In Figure 3.20a, where two adjacent parasites (P12) are activated, the radiation pattern presents a bidirectional structure with a dominant lobe directed towards 240° and a secondary lobe near 120°. The pattern remains relatively symmetric compared to single parasitic element combinations, showing that adjacent parasitic activation generates moderate directivity improvement without excessive distortion and the back radiation around 0° remains suppressed, confirming improved front to back ratio relative to single parasitic element activation.

In the P13 case where the activated parasites are separated by one inactive parasite, the radiation pattern becomes more asymmetrical. The dominant lobe shifts toward 310°, and the secondary lobe appears around 230°, as shown in Figure 3.20b. The beam appears more tilted and slightly narrower than in P12, highlighting stronger phase non-uniformity and directional reinforcement due to increased spatial separation between the active regions.

In Figure 3.20c, the P14 combination where the activated parasitic elements located further apart, the radiation pattern demonstrates a stronger and more concentrated main lobe around 280° and the peak magnitude is noticeable higher than in P12 and P13, exhibiting enhanced constructive interference. Secondary lobes are reduced in comparison, suggesting improving beam focusing, which highlights that activating parasites with the larger angular separation can generate stronger directional radiation.

In the P23 case the pattern becomes highly directive with a dominant narrow, main lobe directed towards 250°, as illustrated in Figure 3.20d. The back lobe is substantially suppressed, producing unidirectional radiation characteristic. Among the four combinations, P23 exhibits the highest directivity and beam concentration, highlighting an optimal current alignment and phase coherence between the selected parasites.

Figure 2.21 presents the radiation patterns for activating dual-parasitic elements P24, P26, P28, and P37 under the out-of-plane magnetization. Compared to single parasitic combinations, these combinations exhibit stronger beam shaping, higher directivity, and more pronounced constructive or destructive interference effects depending on the angular separation of the activated parasites.

For the P24 combination (Figure 3.21a), the radiation pattern is highly directional with a dominant main lobe centered around 270°. The peak magnitude is significantly larger than in previously discussed combinations highlighting strong constructive interference between the activated parasitic elements. The back radiation is substantially suppressed, leading to a high front-to-back ratio, indicates that P24 provides efficient beam focusing on a single preferred direction.

In Figure 3.21b, where the activated parasitic elements (P26) are more symmetrically positioned, the pattern becomes bidirectional. Two nearly equal main lobes appear around 80° and 260°, resembling a dipole-like radiation pattern aligned horizontally. The symmetry highlights balanced current distribution across the structure, leading to radiation in opposite directions rather than a single steered beam.

For P28 (Figure 3.21c), the radiation remains predominantly bidirectional, like P26, but with slightly higher peak intensity and improved lobe definition. The two main lobes are again centered approximately at 90° and 265°. This behavior confirms that activating parasites positioned opposite each other reinforces symmetric modal excitation, generating a two-lobe pattern. In Figure 3.21d, theP37 combination demonstrates a four-lobed radiation structure, showing multiple maxima approximately around 50°, 135°, 215°, and 310°, with reduce intensity along

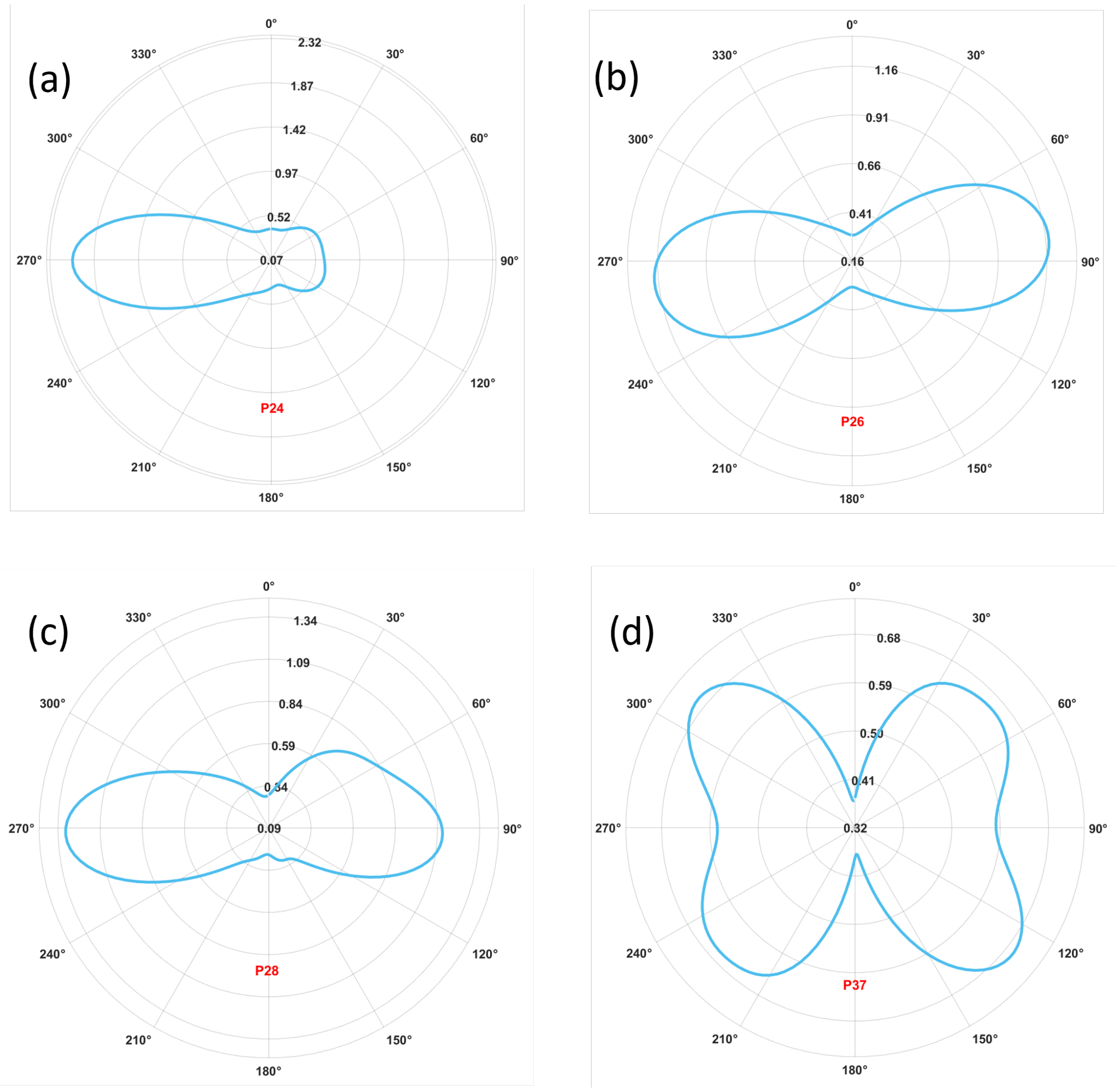

Figure 3.21: Simulated radiation patterns for the activation of dual parasitic element combinations. (a) P24, (b) P26, (c) P28, and (d) P37

the principal axes. This highlights the excitation of high order mode due to the specific spatial arrangement of the activated parasitic element rather than forming a single dominant beam, the energy is distributed among several angular direction resulting in lower directivity compared to P24.

Overall, the result exhibits increased angular separation and symmetry between activated parasites and strongly affects beam formation. Combinations such as P24 produce highly directive single-beam radiation due to constructive phase alignment, while symmetric arrangements like P26 and P28 produce dipole-like bidirectional patterns. More complex combinations such as P37 excite dual element activation, providing flexible control over beam direction, symmetry, and directivity without altering the antenna geometry, enabling effective radiation reconfiguration through selective magnetic loading.

The simulated radiation pattern for activating multi-parasitic elements combination (P2468) under out-of-plane magnetization is illustrated in Figure 3.22. In this combination, four parasitic elements distributed symmetrically around the dipole antenna are simultaneously activated, generating a highly balanced current distribution. The radiation pattern demonstrates a dual beam characteristic, directed towards 90° and 270° in the azimuthal plane. Both beams are identical in magnitude and shape, highlighting strong symmetry in the excited modes. There are no back and side lobes, leading to a deep null along the vertical axis, confirming that the antenna behaves similarly to a horizontally oriented dipole under this excitation condition. The P2468 combination doesn't produce a single steered beam as compared to asymmetrical dual parasitic elements (P24 and P23). Instead, the symmetric placement of the activated parasitic elements enforces balanced phase distribution, resulting in equal radiation in opposite directions. The absence of significant side lobes further highlights that higher-order modes are largely suppressed, and the dominant radiation arises from a fundamental dipole-like mode. The relatively narrow beamwidth of the two main lobes suggests enhanced directivity compared to single-sector excitation. However, since the energy is divided into two opposite directions rather than concentrated into one, the pattern remains bidirectional rather than unidirectional.

Table 3.1 lists the optimal parasitic configurations for both in-plane and out-of-plane magnetic bias. The corresponding beam characteristics and the best realized gain for each configuration are also provided.

Table 3.1: Optimal parasitic configurations under in-plane and out-of-plane magnetic bias

Bias type	**Best config.**	**Beam characteristic**	**Gain (dBi)**
In-plane	P14	Highly directive single beam	2.8
In-plane	P3	Bidirectional (two lobes)	2.7
Out-of-plane	P23	Unidirectional main lobe	2.8
Out-of-plane	P24	Unidirectional main lobe	3.8

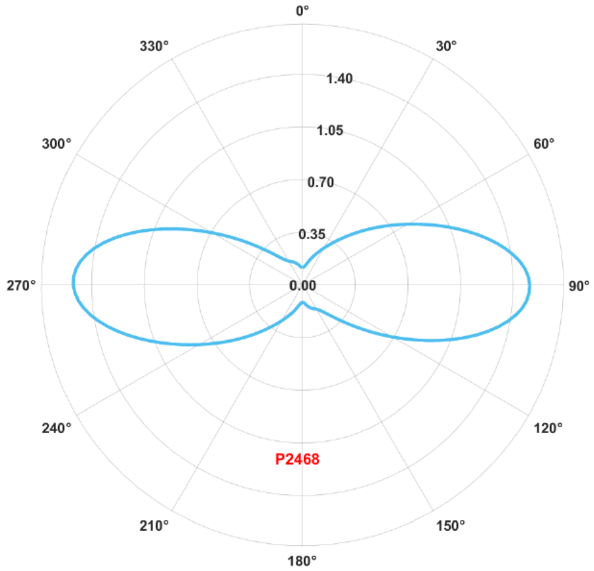

Figure 3.22: Simulated radiation of P2468 combination, where alternating parasitic elements (P2, P4, P6 and P8) are simultaneously biased via out-of-plane magnetization.

Table 3.2 compares the performance of the magnetically biased antenna proposed in this chapter with the electrostatic design from Chapter 2. Magnetic biasing achieves higher realized gain (up to 3.8 dBi) and enables a wider range of scanning angles in the azimuthal plane, including continuous steering patterns that are not possible with discrete electrostatic biasing.

Table 3.2: Comparison of magnetic biasing (this chapter) vs. electrostatic biasing (Chapter 2)

Parameter	**This Ph.D. thesis (magnetic)**	**This Ph.D. thesis (electrostatic)**
Frequency (GHz)	260	200
Peak gain (dBi)	3.8 (out-of-plane, P24)	2.0
In-plane best gain (dBi)	2.8 (P14, P3)	–
Steering angle range	Wide-angle continuous (up to 180°+)	Discrete steps: 0°, 90°, 180°, 270°
Biasing method	Selective magnetic field (in-plane / out-of-plane)	Individual gate lines
Power consumption	Negligible (DC bias)	Negligible (DC bias)
Transparency	No (SiO_2 substrate)	Yes (polyimide)

3.8 Trade-offs in Graphene-Based Beam-Steering Antennas

The design of reconfigurable antennas using graphene involves inherent trade-offs among key performance metrics, including steering range, realized gain, operating frequency, tuning mechanism, and structural complexity. Electrostatic biasing, the most widely adopted approach, enables precise control of the graphene chemical potential through gate voltages, offering continuous or discrete beam steering with relatively simple biasing networks [142, 143]. However, electrostatically tuned antennas often suffer from limited steering range when implemented in compact planar geometries, and the achievable gain is typically moderate due to the inherent losses of monolayer graphene.

In contrast, magnetic biasing introduces anisotropic conductivity through the Hall effect, enabling non-reciprocal wave propagation and potentially wider steering angles without the need for complex gate electrode arrays [144]. Nevertheless, magnetic biasing requires external magnetic field sources (e.g., permanent magnets or electromagnets), which increases device footprint and weight, presenting a trade-off between steering flexibility and system compactness. Furthermore, the combination of both biasing mechanisms, as explored in this work, offers enhanced reconfigurability at the cost of increased control complexity. Another critical trade-off exists between steering range and realized gain. Reflectarray-based designs achieve high gain (exceeding 25 dBi) by employing large aperture sizes and hundreds of tunable elements, but their beam steering range is typically limited to ±30° to ±45° due to phase quantization errors and element coupling [145]. Conversely, dipole-based designs offer wider pattern reconfigurability, including full 360° azimuthal coverage as demonstrated in Chapter 2, but with modest gain values (typically below 4 dBi) suitable for short-range applications such as chip-to-chip communication and intra-device interconnects.

Operating frequency also plays a decisive role. At lower THz frequencies (100-300 GHz), graphene's intraband conductivity dominates, enabling efficient plasmonic resonance and reconfigurability. However, as frequency increases beyond 1 THz, interband transitions become significant, increasing ohmic losses and reducing radiation efficiency [146]. Consequently, most practical graphene-based beam-steering antennas reported in the literature operate below 300 GHz or above 1.5 THz, with a notable performance gap in the sub-THz to 1 THz region.

Table 3.3 presents a comprehensive comparison of representative graphene-based beam-steering antennas and reconfigurable structures reported in the literature, highlighting the diverse tuning mechanisms, steering capabilities, and performance metrics achieved to date.

Table 3.3: Comparison of tuning mechanisms, steering range, and key performance metrics of reconfigurable antennas and metasurfaces.

Reference	**Tuning Mechanism**	**Steering Range**	**Key Metrics**
[142]	Electrostatic	360°	0.86–1.63 dBi from 1.75–2.03 THz
[143]	Electrostatic	−68° to +26° (94° total)	19.7 dBi at 2 THz, SLL: −10.8 dB
[144]	Magnetic	Tunable	Non-reciprocal, THz operation
[145]	Electrostatic	±45°	25.6 dBi from 122–128 GHz
[147]	Electrostatic	0°, ±20°, ±30°, 37°	36 dBi at 23.6 THz
This Ph.D. thesis	Electrostatic	360° Discrete	2 dBi at 200 GHz
This Ph.D. thesis	Magnetic + Electrostatic	0°, 10°, 15°, 20°, 30°, 45°, 60°, 90°, 180°+	3.8 dBi at 260 GHz

3.9 Conclusion

This chapter investigated the effect of magnetic bias on the performance of a graphene-pattern reconfigurable antenna under both in-plane and out-of-plane magnetic field configurations. Numerical analysis shows that the applied magnetic bias significantly modifies the electromagnetic response of the graphene layer by altering its conductivity and surface current distribution. The in-plane magnetic bias primarily influences the propagation of surface waves along the antenna plane, whereas the out-of-plane magnetic bias enhances field interaction normal to the structure, leading to noticeable changes in resonance behavior.

By adjusting the magnetic bias, the antenna exhibits tunable resonance characteristics and improved reconfigurability. These results demonstrate that magnetic-field-controlled graphene patterns provide an effective mechanism for achieving dynamically tunable antenna performance, which is promising for future terahertz and reconfigurable communication applications.

Chapter 4

Design of Hybrid Graphene-Lithium Niobate Nonlinear Metasurface for Dual-Harmonic Generation

4.1 Introduction

The development of ultra-compact, high-efficiency nonlinear optical devices is essential for advancing integrated photonics and optoelectronics, with key applications including on-chip frequency conversion [148], ultrafast optical modulation [149], and quantum light generation [150]. Nonlinear metasurfaces (arrays of subwavelength artificial building blocks) have demonstrated remarkable ability to enhance light-matter interactions at subwavelength scales [151, 152], offering precise control over the phase, amplitude, and polarisation of both fundamental and harmonic fields. However, achieving simultaneous second-harmonic generation (SHG) and third-harmonic generation (THG) on a single, tunable metasurface platform remains a major challenge. Conventional approaches often rely on bulky nonlinear crystals or plasmonic nanostructures, which suffer from high losses, limited power handling, and poor tunability [153, 154]. Recently, simultaneous SHG and THG has been demonstrated in engineered metasurfaces for RF systems, in metal-dielectric metasurfaces assisted by THz fields, and in MoS2-based metasurfaces.

Metasurfaces are now established as a versatile platform. By employing uniform or spatially varying geometries, they enable tailored control over the phase, amplitude, and polarisation of nonlinear signals, a capability difficult to achieve with conventional optics. This paradigm opens free-space applications such as mode conversion, beam shaping, and nonlinear holography. However, their subwavelength thickness makes conventional phase-matching inapplicable. To overcome this, structural resonances are used to localise electromagnetic fields intensely within the nanostructures. Various resonance types have been explored to enhance SHG, including Mie resonances [155, 156], bound states in the continuum (BIC) [157–159], Fano resonances [160, 161], and anapoles [162–164].

Over the past decade, resonant metasurfaces have been widely studied to create intense localised fields for nonlinear optics [165,166]. Early work used plasmonic resonances in metal and graphene metasurfaces, but performance was limited by optical losses. More recent progress has moved to low-loss dielectric and hybrid systems, employing III-V semiconductors such as gallium phosphide (GaP) [167], aluminium gallium arsenide (AlGaAs) [168], graphene-insulator-graphene (GIG) [169], and gallium arsenide (GaAs) [170], which benefit from strong second- and third-order nonlinearities. Their high refractive index contrast enables strong field confinement, but their narrow bandgap causes absorption of second-harmonic signals in the visible, limiting conversion efficiency [171]. Guided-mode resonances (GMRs), despite their strong field confinement and high quality factors, have not been fully exploited for this purpose. Efficient coupling of free-space radiation to guided modes in periodic structures can dramatically enhance light-matter interactions, leading to high Q-factors and substantial enhancement of both SHG and THG.

Most nonlinear optical devices are optimised for a single nonlinear process, yet many materials exhibit simultaneous second- and third-order nonlinearities. Although undesired orders can be suppressed by careful design, sufficiently large nonlinearities mean that both SHG and THG influence the system response. THG can arise from two competing processes: cascaded sum-frequency generation (CSFG, a second-order process) and direct THG (DTHG, a third-order process) [172]. Their efficiencies depend on the material's nonlinear susceptibility and the device's modal spectrum. While it is possible to optimise one process over the other [172], in non-optimised systems their contributions to the THG signal may be entangled, making experimental differentiation necessary.

Lithium niobate ($LiNbO_3$) is outstanding for SHG due to its strong second-order nonlinearity, high damage threshold, and compatibility with integrated photonic circuits [173, 174]. Thin-film $LiNbO_3$ further improves efficiency through modal phase-matching and resonance effects [175, 176]. Meanwhile, graphene is a promising platform for THG because of its third-order nonlinear susceptibility and electrostatic tunability via bias voltage [177, 178].

SHG and THG have been reported in $LiNbO_3$ [179,180] and in magnesium-doped $LiNbO_3$ ($Mg{:}LiNbO_3$) [181]. In those cases, however, the THG process is usually attributed either to direct THG in GaP or to cascaded sum-frequency generation in $LiNbO_3$. A detailed investigation of THG in such hybrid systems is still lacking.

Integrating $LiNbO_3$'s second-order nonlinearity with graphene's third-order response presents challenges, but recent advances in nanofabrication, including accurate 2D material transfer [182], thin-film nanostructuring of $LiNbO_3$ [183], and van der Waals stacking [184], offer promising solutions. Numerical simulations are critical to identify key geometric parameters and operating conditions that enhance nonlinear interactions, thereby guiding experimental efforts and reducing development costs.

The absence of such hybrid metasurfaces can be attributed to several difficulties: achieving efficient coupling between $LiNbO_3$'s second-order response and graphene's third-order response, precise alignment and stacking of atomically thin graphene with $LiNbO_3$ thin films, and optimising optical field overlap in a subwavelength structure to enhance both SHG and THG simultaneously. While recent studies have demonstrated standalone $LiNbO_3$-based SHG [185] or graphene-enhanced THG devices [186], a unified platform combining both materials has not yet been realised.

4.1.1 Tuning Mechanisms for Reconfigurable Metasurfaces

The lack of post-fabrication tunability is the main limitation of static metasurfaces. Once fabricated, their electromagnetic properties are fixed, restricting adaptability to varying environmental conditions [124]. Thus, obtaining reconfigurability has become a central research goal, focusing on active materials whose optical properties can be dynamically varied by external stimuli. Several tuning approaches have been explored:

1. **Thermo-optic biasing**: Materials whose refractive index changes with temperature offer tunability, but thermal tuning suffers from slow response times and high power consumption, making it impractical for high-speed operation [187].

2. **Electro-optic biasing**: Electro-optic effects (e.g., in lithium niobate) allow fast modulation via applied electric fields, achieving sub-nanosecond switching. However, high voltages, specialized material integration, and limited index modulation depth remain challenges [188].

3. **Depletion biasing**: Modulating free-carrier concentration in semiconductors (e.g., III-V compounds) offers moderate speed but introduces absorption losses and free-carrier dispersion that degrade performance [189].

4. **Phase-change materials (PCMs)**: Materials such as $Ge_2Sb_2Te_5$ (GST) can be reversibly switched between amorphous and crystalline phases with distinct refractive indices. PCMs provide non-volatile biasing (state persists without power), but they are slow, energy-intensive, and have limited cycling endurance [190].

5. **Mechanical actuation**: Physically reconfiguring metasurface elements or spacing offers large index contrast without intrinsic optical loss, but mechanical actuation is slow, prone to reliability issues, and difficult to scale for large apertures [191].

Each of these biasing schemes involves trade-offs among speed, power consumption, tuning range, losses, and system complexity. There remains a critical gap for a biasing approach that is fast, highly efficient, and scalable across sub-THz and IR frequencies. This gap motivates the exploration of emerging hybrid material platforms, such as the graphene-lithium niobate metasurface proposed in this chapter, where guided-mode resonances provide strong field enhancement and the materials themselves offer distinct second- and third-order nonlinearities.

Motivated by these challenges, this chapter proposes a novel hybrid graphene-$LiNbO_3$-SiO_2 metasurface that supports simultaneous SHG and THG on a single resonant platform. SHG is mediated by the strong $\chi^{(2)}$ nonlinearity of $LiNbO_3$, harnessed through guided-mode resonance enhancement, while THG originates from the $\chi^{(3)}$ response of graphene and SiO_2. Numerical results show SHG and THG efficiencies reaching $\eta_{\text{SHG}} = 2.37 \times 10^{-4}$ and $\eta_{\text{THG}} = 4.8 \times 10^{-6}$, respectively, highlighting the coexistence of distinct nonlinear orders arising from different material responses and GMRs within the same metasurface. This material-enabled separation of nonlinear processes distinguishes the proposed architecture from previous hybrid approaches and provides a versatile platform for multifunctional nonlinear photonic devices. Overall, these results underscore the potential of combining $LiNbO_3$ and graphene in metasurfaces for nonlinear integrated photonics.

4.2 Theory of Nonlinear Optics

In electromagnetic theory, the polarization density of a material is commonly assumed to be linearly proportional to the applied electric field, expressed as [192–194]:

$$P = \varepsilon_0 \, \chi^{(E)} \, E \tag{4.1}$$

where χ denotes the electric susceptibility of the medium. In the most general case, the susceptibility can be tensorial, allowing the induced polarization to depend on the direction of the applied electric field. Moreover, the polarization may include contributions arising from magnetic fields through magneto-electric coupling. However, for simplicity, we restrict our discussion to isotropic media characterized by a scalar electric susceptibility and neglect any magnetic coupling effects.

At low electric field strengths, the linear relation $P = \varepsilon_0 \chi E$ provides an accurate description of the material response. When the applied fields become sufficiently strong, however, deviations from linearity emerge, giving rise to nonlinear optical phenomena. To account for these effects, the polarization must be expressed as a series expansion that includes higher-order terms in the electric field.

$$P = \varepsilon_0 \left[\chi^{(1)} + \chi^{(2)} E + \chi^{(3)} E^2 + \cdots \right] E \tag{4.2}$$

In Eq. (2), the electric susceptibility is expanded into a series of terms of increasing order. The first term, $\chi^{(1)}$, corresponds to the familiar linear susceptibility. Generally, the lower-order terms are much larger than the higher-order ones, so that $\chi^{(1)} \gg \chi^{(2)} \gg \chi^{(3)}$, and so on. As a result, at low electric field strengths, the linear term dominates the response. However, when the field becomes sufficiently strong, such as with high power lasers or pulsed lasers that generate brief, intense spikes, higher order nonlinear terms begin to contribute significantly.

In linear optics, different light frequencies do not interact, so they can be considered independently, and the resulting fields simply add. Interference and the combination or separation of frequencies and wavevectors can be handled straightforwardly using Fourier analysis. In contrast, in the nonlinear regime, the powers of the electric field cause mixing between different frequencies, wavevectors, and phases. This introduces new degrees of freedom, enabling phenomena such as frequency conversion and all-optical information processing.

As a simple example, consider a second-order nonlinearity acting on a field composed of two frequency components [195,196].

$$E(t) = \frac{1}{2}\left(E_1 e^{-i\omega_1 t} + E_2 e^{-i\omega_2 t} + \text{c.c.}\right) \tag{4.3}$$

where E_1 and E_2 are the two components of electric field, which are complex constants, along with their complex conjugates. When this field is squared, the resulting expression clearly contains terms at twice the original frequencies, as well as terms corresponding to the sum and difference of the two frequencies, and even a constant (DC) component.

As a result, the squared electric field contains all harmonic and mixed-frequency terms as follows:

$$\begin{aligned} E^2(t) = \frac{1}{4}\Bigg(& E_1^2\, e^{-i2\omega_1 t} + E_2^2\, e^{-i2\omega_2 t} + 2E_1E_2\, e^{-i(\omega_1+\omega_2)t} \\ & + 2E_1E_2^*\, e^{-i(\omega_1-\omega_2)t} + |E_1|^2 + |E_2|^2 + \text{c.c.}\Bigg) \end{aligned} \tag{4.4}$$

If the field is cubed, a similar pattern occurs, but with an even larger set of frequency components. For a field with three frequency components, all three can interact in a third-order nonlinear process. The doubling of the fundamental frequency is known as second-harmonic generation (SHG), while tripling is referred to as third-harmonic generation (THG). Processes that combine frequencies through addition or subtraction are called sum-frequency generation (SFG) and difference frequency generation (DFG), respectively. When three frequencies combine to produce a fourth, this is generally referred to as four-wave mixing (FWM) [197].

Macroscopic material properties are commonly described in terms of electric susceptibility. For example, the relative permittivity can be written as [198]:

$$\frac{\varepsilon}{\varepsilon_0} = 1 + \chi \tag{4.4}$$

In the linear regime, the susceptibility reduces to its first-order term, $\chi = \chi^{(1)}$, which is independent of the applied field strength. As a result, the permittivity ε remains constant and does not vary with the intensity of the electromagnetic field.

In the nonlinear regime, however, the polarization expression implies that the susceptibility becomes dependent on the electric field strength. Third-order nonlinearities introduce an explicit dependence on the field intensity. Consequently, macroscopic material parameters such as the permittivity and refractive index are no longer fixed but vary with the strength of the applied field. A linear dependence on the electric field gives rise to the Pockels effect, while a dependence on the square of the electric field leads to the Kerr effect [199].

To understand the microscopic origin of nonlinear optical effects, we consider a classical anharmonic oscillator model. In this picture, electrons are bound in a potential well that deviates from a perfect parabola at large displacements. The resulting nonlinear restoring force leads to the generation of harmonics when the electron is driven by an intense optical field.

The macroscopic polarization can be written in terms of the microscopic electron displacement as [196,198]:

$$P = -eNx \tag{4.5}$$

where N is the electron density. When the electron displacement x is small, the binding potential can be approximated by a smooth Taylor expansion around the equilibrium position:

$$U(x) = \frac{1}{2}m_0\omega_0^2x^2 + \frac{1}{3}m_0C_2x^3 + \frac{1}{2}m_0C_3x^4 + \cdots \tag{4.6}$$

The corresponding restoring force is obtained by taking the negative gradient of the potential,

$$F(x) = -\frac{dU}{dx} = m_0\omega_0^2x + m_0C_2x^2 + m_0C_3x^3 \tag{4.7}$$

We assume that $\omega_0^2 \gg C_2C_3$, so that for small displacements the linear restoring force dominates. However, when the electron is driven far from its equilibrium position, the higher-order terms become relevant and give rise to nonlinear behavior. Including a phenomenological damping term with coefficient γ and an external driving electric field $E(t)$, the equation of motion for the electron becomes

$$m_0\ddot{x} + m_0\gamma\dot{x} + m_0\omega_0^2x + m_0C_2x^2 + m_0C_3x^3 = -eE(t) \tag{4.8}$$

where the driving field is assumed to be harmonic. For a monochromatic excitation, the electric field can be written as

$$E(t) = \frac{1}{2}(E_0 e^{-i\omega t} + \text{c.c.}) \tag{4.9}$$

The electron displacement can then be expressed as a sum of harmonics of the driving frequency:

$$x(t) = \sum_{n=1}^{\infty} \frac{1}{2}(A_n e^{-in\omega t} + \text{c.c.}) \tag{4.10}$$

Substituting this expression into the equation of motion and collecting terms oscillating at the same harmonic $e^{-in\omega t}$ yields a set of independent equations for each amplitude A_n [196, 198, 199].

$$A_1 = \frac{eE_0}{m_0(\omega_0^2 - \omega^2 - i\gamma\omega)} \tag{4.11}$$

This expression exhibits the same frequency dependence as the classical bound-electron model used in linear optical theory. Although additional contributions at the fundamental frequency arise from the nonlinear x^2 and x^3 terms, these contributions are much smaller because they are proportional to the higher-order coefficients C_2 and C_3, as well as higher-order amplitudes A_n, which are themselves weak.

Finally, the amplitude A_1 can be directly related to the linear susceptibility $\chi^{(1)}$ through the first-order polarization relation $P^{(1)} = \varepsilon_0 \chi^{(1)} E$ together with the microscopic polarization expression, provided that only the leading (linear) term in the displacement x is considered.

By equating the first-order polarization written in terms of the susceptibility with the microscopic expression for the polarization, we obtain

$$\varepsilon_0 \chi^{(1)} \frac{1}{2} E_0 (e^{-i\omega t} + \text{c.c.}) = -eN \frac{1}{2} A_1 (e^{-i\omega t} + \text{c.c.}) \tag{4.12}$$

Substituting the expression for A_1 and solving for the susceptibility yields

$$\chi^{(1)}(\omega) = \frac{e^2 N}{\varepsilon_0 m_0} \frac{1}{\omega_0^2 - \omega^2 - i\gamma\omega} \tag{4.13}$$

which is the well-known expression for the linear susceptibility in the classical bound-electron oscillator model.

Using the same approach, higher-order harmonic responses can also be obtained. For example, to determine the amplitude of the third harmonic (A_3), we collect only the terms oscillating at 3ω.

$$A_3 = \frac{1}{4} \frac{C_3 A_1^3}{\omega_0^2 - (3\omega)^2 - i3\gamma\omega} \tag{4.14}$$

By relating the third-order polarization to the third-order susceptibility through $P^{(3)} = \varepsilon_0 \chi^{(3)} E^3$, and using the connection between A_1 and $\chi^{(1)}$, one finds

$$\chi^{(3)}(\omega,\omega,\omega;3\omega) = \frac{C_3 N^2 e^4}{4m_0}\chi^{(1)3}(\omega)\chi^{(1)}(3\omega) \tag{4.15}$$

The phase accumulated by the fundamental wave is

$$\phi_\omega = k(\omega)L \tag{4.16}$$

whereas the phase accumulated by the third-harmonic wave is

$$\phi_{3\omega} = 3k(3\omega)L = \frac{3\omega}{c}n(3\omega)L \tag{4.17}$$

The nonlinear wavevector must equal the sum of the input wavevectors,

$$k_{NL} = \sum_i k_i \tag{4.18}$$

In metasurfaces, this condition determines the direction in which the generated nonlinear signal propagates, unless additional phase control is introduced through structural design or engineered phase gradients.

Conventional nonlinear optical materials typically require a substantial bulk in order to achieve a measurable response, and their efficiency is often limited by strict phase-matching requirements. In contrast, metasurfaces can provide a significant nonlinear response within an ultrathin footprint, making them highly attractive for on-chip integration. One of the key advantages of metasurfaces is that the phase-matching condition is greatly relaxed, since the interaction length across the surface is much shorter than the wavelength, resulting in negligible phase accumulation [195, 199].

Similar to linear metasurfaces, nonlinear metasurfaces can be broadly categorized into plasmonic and dielectric types. In plasmonic metasurfaces, metallic nanostructures couple strongly with light and support localized surface plasmons (LSPs), which tightly confine the electromagnetic fields both within and near the metal. Since the nonlinear polarization scales with powers of the field (depending on the specific nonlinear process), this strong field confinement can dramatically enhance the generated nonlinear signals. Moreover, metals themselves often exhibit significant intrinsic nonlinearities, though the largest fields are typically localized at the metal boundaries [200]. Plasmonic metasurfaces have been successfully used to demonstrate second-harmonic generation (SHG) [201], third-harmonic generation (THG) [202], and four-wave mixing (FWM) [203].

A major limitation of plasmonic structures, however, is their inherent absorption, which can reduce efficiency and lead to damage at high laser intensities. Dielectric or semiconductor metasurfaces address this issue: while they provide somewhat weaker field confinement [204], they are far less absorptive and can withstand higher laser powers. Additionally, dielectric resonators can support Mie resonances with both electric and magnetic dipole contributions, which can be tailored through geometry to optimize the nonlinear response [205].

As discussed earlier, second-order nonlinear processes such as SHG require some form of asymmetry in the system. In the case of metasurfaces, this asymmetry can be introduced even if the underlying crystal is symmetric or no external field is applied. By designing asymmetric meta-atoms or arranging them in a pattern that locally breaks symmetry, a measurable second-order nonlinear response can be achieved [206].

Nonlinear metasurfaces are particularly well-suited for interactions with circularly polarized light. Circular dichroism measures the difference in response between left- and right-handed circular polarizations (LCP and RCP). In the nonlinear regime, a nonlinear circular dichroism can be defined as the difference in the generated nonlinear signal when the system is excited with LCP versus RCP light. A key advantage of this approach is that the fundamental, non-converted light does not interfere with the measurement [207]. Another benefit of using circularly polarized light is access to the Pancharatnam-Berry (PB) phase, which provides robust and simple phase control. In linear optics, the phase of scattered light can be tuned by rotating the individual meta-atoms; in the nonlinear regime, a similar PB-phase concept applies. This allows for the steering of nonlinear signals in different directions depending on the circular polarization handedness and can be used for polarization-dependent nonlinear holography [208].

Phase control is also possible with linearly polarized light. For example, E. Almeida in [203] demonstrated that rectangular etchings in a thin gold film can generate a four-wave mixing (FWM) signal, and the aspect ratio of the rectangles can be tuned to control the nonlinear phase across the full 2π range. This phase tuning enabled the deflection, diffraction, and lensing of the FWM signal. In a subsequent study [202], V-shaped gold antennas embedded in a silica dielectric were used to control the phase of third-harmonic generation (THG). By varying the arm length and the angle between the arms, the authors achieved full 2π phase coverage with a consistent amplitude. This approach was then used to encode a nonlinear hologram, where illumination with an infrared laser reproduced the encoded images at the third harmonic, which could be easily separated from the background infrared light.

Nonlinear metasurfaces have demonstrated a remarkable range of functionalities, including harmonic generation, four-wave mixing, and nonlinear holography. However, one persistent challenge is that the conversion efficiency of the fundamental wave into the nonlinear wave is quite low, and improving this efficiency remains an active area of research. One strategy to enhance efficiency is to incorporate materials with strong optical transitions at the resonant frequencies of the metasurface, such as quantum wells or transition metal dichalcogenides (TMDs) [202]. Moreover, the ability to tune the nonlinearity, whether via structural design, choice of material, or applied fields, is highly feasible for practical applications.

4.3 Graphene Optical Conductivity in Nonlinear Hybrid Metasurface

Graphene is a two-dimensional (2D) material, and its optical response is typically described in terms of its surface conductivity $\sigma(\omega)$, which relates the current density $J(\omega)$ to the applied electric field $E(\omega)$ as:

$$J(\omega) = \sigma(\omega)\, E(\omega) \tag{4.19}$$

In pristine graphene, the conductivity is isotropic [209]. Extensive theoretical treatments and experimental measurements [210,211] have characterized graphene's conductivity across a wide spectral range, from the infrared to the visible and ultraviolet.

The linear response of graphene is governed by its surface conductivity, which includes both intraband and interband contributions to the Kubo formula. For the baseline case $E_F = 0$ eV at room temperature, the linear surface conductivity is given by:

$$\sigma(\omega) = \frac{e^2 k_B T \tau}{\pi \hbar \bar{\omega}} \left[\frac{E_F}{k_B T} + 2 \ln \left(e^{-E_F/(k_B T)} + 1 \right) \right] + \frac{i e^2}{4 \pi \hbar} \ln \frac{\xi - i\bar{\omega}}{\xi + i\bar{\omega}}, \tag{4.20}$$

where e is the elementary charge, $\hbar$ denotes the reduced Plank constant, k_B is the Boltzmann constant, $T = 300$ K represents the temperature, $\tau = 0.5$ ps is the carrier relaxation time. Here, $\bar{\omega} = i\omega\tau$ and $\xi = 2|E_F|\tau/\hbar$, where ω is the fundamental angular frequency.

The nonlinear response of graphene is primarily dominated by interband transitions at the telecom wavelengths. The total surface current density including linear and third-order nonlinear contributions is expressed as

$$J_s = \sigma(\omega) E_t + \sigma_s^{(3)} |E_t|^2 E_t, \tag{3}$$

where E_t is the tangential electric field at the graphene boundary, $\sigma(s)$ denotes the linear surface conductivity, and $\sigma_s^{(3)}$ is the third-order surface conductivity associated with THG.

For optical frequencies ($\hbar\omega \gg E_F$), the third-order conductivity is given by [212, 213]:

$$\sigma_s^{(3)}(3\omega; \omega, E_F, \tau, T) = \frac{i e^4}{48 \pi \hbar^3 \omega^4} \left[\tanh \left(\frac{\hbar \omega}{4 k_B T} \right) + i \frac{\hbar}{\tau \omega} \right]. \tag{4.21}$$

Thus, in our proposed nonlinear hybrid metasurface, the linear conductivity of graphene is primarily dominated by interband transitions in the near-infrared, while the third-order nonlinear conductivity governs the generation of the third harmonic. The guided-mode resonance in lithium niobate strongly improves the local field, increasing both the SHG from lithium niobate and THG from graphene, enabling an efficient, multifunctional nonlinear metasurface [204, 214].

4.4 Design of a Hybrid Nonlinear Metasurface

The proposed nonlinear hybrid metasurface based on guided-mode resonant dielectric grating composed of a graphene-$LiNbO_3$-SiO_2, as depicted in Figure 4.1. The structure consists of three-layer stack arranged along the z-axis, comprising a monolayer graphene sheet, z-cut lithium niobate layer and glass (SiO_2) substrate. The metasurface is periodic in both x- and y-directions with a grating period P. Each graphene unit cell has a square footprint of side width W and contains a centrally positioned $LiNbO_3$ pillars with a thickness of H and with the same width as graphene. A monolayer graphene is deposited on the top of lithium niobate layer, acting as nonlinear and tunable layer that enables active modulation of Fermi level (E_F) via electrical biasing. The metasurface is illuminated by a normally incident wave with a wavelength of 1550 nm and electric field polarization oriented along the x-axis.

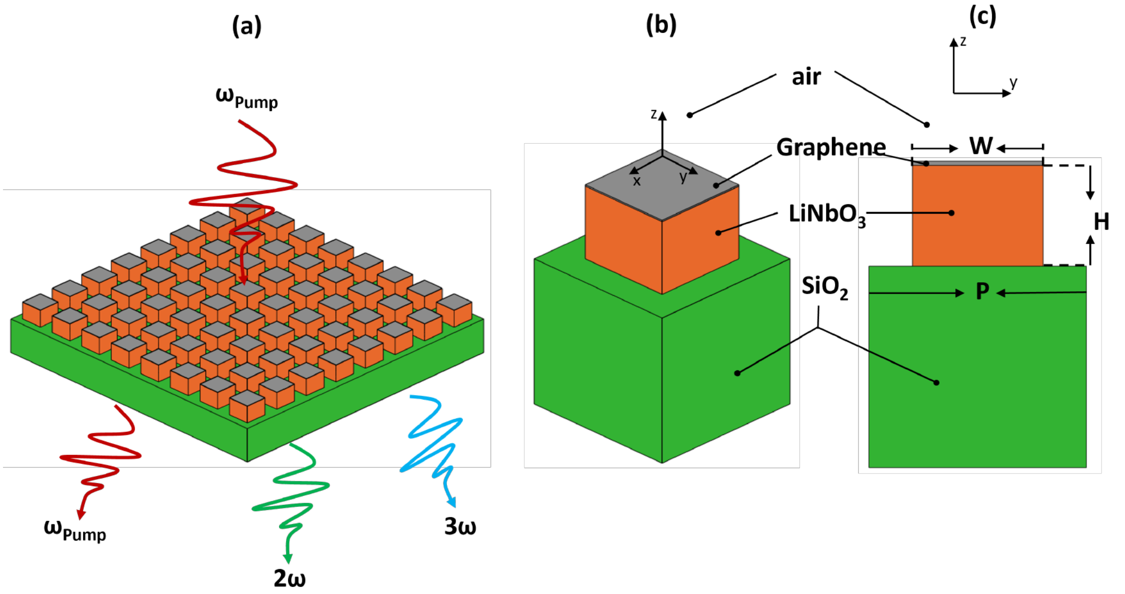

Figure 4.1: Schematic illustration of the graphene-lithium niobate metasurface. (a) Three-dimensional (3D) schematic of the proposed nonlinear hybrid metasurface unit cell designed for SHG and THG, (b) 3D view of a single unit cell, (c) Two-dimensional top view of the metasurface. Here P denotes the grating period, H and W denote the thickness and width of the lithium niobate pillar, respectively.

The graphene layer on top of the $LiNbO_3$ pillars is biased using a coplanar side-gate configuration. Metal contacts (e.g., Au/Ti) are deposited at the edges of the metasurface, connecting to the graphene sheet. The $LiNbO_3$ pillars act as a dielectric spacer, while the SiO_2 substrate serves as an insulating layer. A gate voltage applied between the graphene and a buried electrode (or the silicon substrate) shifts the Fermi level E_F via capacitive charging. The relationship $E_F \propto$

$\sqrt{V_g}$ (derived in Chapter 2) holds, with E_F up to 0.5 eV achievable at $V_g \approx$ 5–10 V. Because the pillars are periodic and isolated, the bias must be applied globally to the entire graphene sheet; sector-wise biasing is not implemented in this design.

In numerical model, lithium niobate is treated as a dispersive anisotropic medium, with its optical axis aligned along the x-direction of the simulation coordinate system. The orientation is consistent with the nonlinear polarization tensor employed in our analysis, where the dominant second-order nonlinear coefficient d_{33} couples to the $(E_x)^2$ field component. The ordinary and extraordinary refractive indices at the fundamental wavelength of 1550 nm are calculated using the Sellmeier model addressed in [215]. Specifically, at 1550 nm the refractive indices of lithium niobate are $n_x = n_e = 2.138$ and $n_y = n_z = n_o = 2.211$, where n_o and n_e denote the ordinary and extraordinary indices, respectively. The in-plane anisotropy breaks symmetry in the xy-plane and gives rise to polarization-dependent linear and nonlinear responses, even for metasurfaces exhibiting C_{4v} structural symmetry [216]. The initial geometric configuration of the metasurface was adapted from Ref [217].

We consider a z-cut lithium niobate crystal as the primary source of second-order optical nonlinearity in the proposed hybrid metasurface. When the structure is excited at the pump wavelength, lithium niobate generates a nonlinear polarization $P^{(\mathrm{NL})}$ which can be expressed in terms of the second-order susceptibility tensor:

$$\begin{bmatrix} P_x^{\mathrm{NL}} \\ P_y^{\mathrm{NL}} \\ P_z^{\mathrm{NL}} \end{bmatrix} = 2\varepsilon_0 \begin{bmatrix} d_{33} & d_{31} & d_{31} & 0 & 0 & 0 \\ 0 & d_{22} & -d_{22} & 0 & 0 & 0 \\ 0 & 0 & 0 & -d_{22} & d_{31} & 0 \end{bmatrix} \begin{bmatrix} E_x^2 \\ E_y^2 \\ E_z^2 \\ 2E_yE_z \\ 2E_xE_z \\ 2E_xE_y \end{bmatrix} \tag{4.22}$$

where E_x, E_y, and E_z denote the components of the fundamental electric field inside the $\mathrm{LiNbO_3}$ layer. For z-cut $\mathrm{LiNbO_3}$, the dominant nonlinear interaction arises from d_{33} coefficient, which couples most efficiently to the $(E_x)^2$ field component due to the chosen orientation of the optical axis.

The second-order nonlinear coefficients employed in this study are $d_{31} = -3.2$ pm/V, $d_{22} = 1.9$ pm/V, and $d_{33} = -19.5$ pm/V, corresponding to a wavelength of 1313 nm.

Although the metasurface is designed to operate at a fundamental wavelength of 1550 nm, the dispersion of the second-order nonlinear coefficients of lithium niobate in the near-infrared regime is relatively weak. As experimentally demonstrated in Ref. [218], the values of d_{31}, d_{22}, and d_{33} vary by less than 10% over the wavelength range from 1.3 μm to 1.6 μm. Consequently, the use of the 1313 nm nonlinear coefficients at 1550 nm introduces only a negligible error and does not affect the qualitative or quantitative conclusions of this study.

In addition to the intrinsic second-order nonlinearity of the lithium niobate layer, the third-order nonlinear response of the silicon dioxide substrate is also considered. This contribution is modeled by explicitly including a third-order nonlinear susceptibility of $\chi^{(3)} = 2 \times 10^{-22}\,\mathrm{m}^2/\mathrm{V}^2$, consistent with previously reported experimental values [212]. Although the nonlinear response of $\mathrm{SiO_2}$ is relatively weak compared to that of lithium niobate, its inclusion ensures a comprehensive description of the nonlinear processes occurring within the hybrid metasurface.

For bottom illumination (through the $\mathrm{SiO_2}$ substrate), the incident refractive index increases from 1 to 1.45, which redshifts the guided-mode resonance by approximately 8 nm, reduces the Q-factor from 947 to about 850, and decreases the nonlinear conversion efficiency by roughly 20% due to weaker field confinement. Top illumination is therefore preferred for optimal performance, though bottom illumination may be acceptable in integrated configurations where the substrate is transparent and the superstrate is not used.

4.5 Simulations and Results

All numerical simulations were carried out using finite-element method (FEM) implemented in COMSOL Multiphysics. In the simulations, graphene is modeled as an infinitesimally thin 2D boundary layer located on the top of lithium niobate layer and its linear optical response is incorporated via a frequency-dependent surface conductivity which is applied through the surface current density boundary condition, in which the tangential electric field E_t drives linear surface current. The nonlinearity of graphene is comprised by creating an additional nonlinear surface current density in terms of:

$$J^{NL} = \sigma^{(3)} |E_t|^2 E_t$$

which accounts for the third-order nonlinearity responsible for generation of third harmonic. This formulism permits the solver to self-constantly evaluate the nonlinear current induced at the graphene interface under pump excitation and the resulting harmonic fields, without depending on perturbative post-processing.

The nonlinear efficiency of the second harmonic generation (SHG) and third-harmonic generation (THG) was optimized with respect to zeroth diffraction order, as this order corresponds to the collinear harmonic signal propagating normal to the metasurface plane. In typical experimental configurations, the zeroth order can be collected most efficiently due to its direct coupling into free space or integrated optical components. For metasurfaces in the subwavelength, higher diffractions orders are suppressed, and the zeroth order dominates the nonlinear emission because of constructive interference and favorable phase match conditions across the periodic array. This optimization strategy is widely adopted in nonlinear metasurface works and gives a performance metric that is directly relevant for practical on-chip and free-space implementations employing normal-incidence excitation and collection [219].

The nonlinear conversion efficiencies for second-harmonic generation and third-harmonic generation, denoted by η_{SHG} and η_{THG}, respectively, were evaluated using quantum-classical correspondence formulism [220]. Within this framwork, and following the definition of differential efficiency that is commontly used for parametric nonlinear processes, the normalized conversion efficiency of an nth-order harmonic process (with $n = 2$ for SHG, and $n = 3$ for THG) scales as:

$$\eta_n = \frac{|E_{\text{out}}|^2}{|E_{\text{pump}}|^{2n}} \tag{4.23}$$

with additional geometric correction factors accounting for oblique incidence and transmission angles.

To extract the radiated harmonic fields, the components of the far-field propagate at an angle θ_i and are characterized by in-plane wavevector components (k_x, k_y) were obtained using a spatial averaging procedure. Specifically, the harmonic electric fields were projected onto plane wave modes by applying the phase factor $\exp[i(k_x x + k_y y)]$ and performing spatial averaging over the output plane. This approach effectively implements a Green's function-based far-field extraction technique within COMSOL and enables accurate separation of different diffraction orders.

For the nth-order harmonic process (either SHG or THG), the conversion efficiency implemented in COMSOL is given by

$$\begin{aligned} \eta_{\mathrm{XHG}} = \frac{\cos(\theta_t^{\mathrm{XHG}})}{\cos(\theta_i)} & \left[\left| \left\langle e^{i(k_x^{\mathrm{XHG}} x + k_y^{\mathrm{XHG}} y)} \frac{\sqrt{n_{xx}^{\mathrm{XHG}}}\, E_x^{\mathrm{XHG}}}{E_0} \right\rangle \right|^2 \right] \\ & + \left[\left| \left\langle e^{i(k_x^{\mathrm{XHG}} x + k_y^{\mathrm{XHG}} y)} \frac{\sqrt{n_{yy}^{\mathrm{XHG}}}\, E_y^{\mathrm{XHG}}}{E_0} \right\rangle \right|^2 \right] . \end{aligned} \tag{4.24}$$

Where η_{XHG} represents either η_{SHG} or η_{THG}, θ_i is the angle of incidence of fundamental pump beam, and $(\theta_i)_{\mathrm{XHG}}$ is the transmission angle at the corresponding harmonic frequency. The quantities $(k_x)_{\mathrm{XHG}}$ and $(k_y)_{\mathrm{XHG}}$ denote the in-plane wavevector components of the emitted harmonic field, while $(n_{xx})_{\mathrm{XHG}}$ and $(n_{yy})_{\mathrm{XHG}}$ are the diagonal components of the refractive-index tensor computed at the harmonic frequency. The terms $(E_x)_{\mathrm{XHG}}$ and $(E_y)_{\mathrm{XHG}}$ correspond to the electric field components of the generated harmonic wave, E_0 is the amplitude if the incident pump field, $\langle\cdot\rangle$ denotes spatial averaging over the output plane.

The primary objective of this work is to optimize the geometry of the proposed nonlinear hybrid metasurface to enhance both the second-harmonic generation (SHG) and third-harmonic generation (THG) simultaneously. The efficiencies of these nonlinear processes are quantified by η_{SHG} and η_{THG}, respectively. In comparison to most designs of metasurface addressed in the literature, which are typically optimized to enhance only a single nonlinear process, our design approach aims at dual-process optimization, where both nonlinear responses are maximized at the same pump wavelength. This strategy is particularly attractive for multifunctional nonlinear photonic devices, where multiple frequency conversion processes are needed within a single platform.

To obtain this objective, we focus on two geometrical parameter rs that have the strongest influence on the formation of guided-mode resonances (GMRs): the grating period P, and the thickness H of the lithium niobate layer. The effective refractive indices of the guided modes are directly controlled with the help of these parameters, supported by patterned lithium niobate pillars and determine how effectively these modes can couple to free space radiation. By tuning H and P, it is therefore possible to control the phase matching condition between the guided mode and incident beam, that plays a central role in improving the local electromagnetic fields and, consequently, the nonlinear optical response. All other geometric parameters of the graphene and $LiNbO_3$ were kept constant throughout the optimization process to clearly isolate the role of GMRs tuning and geometric dispersion. Particularly, the duty cycle was fixed at $dc = \frac{W}{P} = 0.75$, and the Fermi level of graphene was set to 0 eV. The metasurface was illuminated by a normal incident beam with a wavelength of 1550 nm and is linearly polarized along the x-direction, with a pump intensity of $1\,\mathrm{GW/cm^2}$. This excitation configuration was chosen to ensure consistent comparison across different geometries and to reflect typical experimental conditions.

The grating period P was chosen from 800 nm to 1100 nm to span the region where the guided-mode resonance of the $LiNbO_3$ layer falls near the pump wavelength of 1550 nm. From the grating equation $\beta = 2\pi m/P$, and using the effective indices of the homogenized layer ($n_{\text{eff}} \approx 1.8$–$2.2$), the fundamental TE and TM resonances appear at P between 850 nm and 1050 nm. The thickness H was scanned from 500 nm to 1000 nm to cover the transition from subwavelength to multi-mode waveguide behaviour. The upper bound was limited by computational cost and the onset of higher-order modes that complicate the nonlinear response.

In the simulations, illumination is from the top (air side). For bottom illumination (through the SiO_2 substrate), the effective refractive index of the incident medium changes from 1 to 1.45, which shifts the GMR condition. Preliminary simulations show a redshift of the resonance by approximately 8 nm and a slight reduction in Q-factor (from 947 to 850). The nonlinear conversion efficiencies decrease by about 20% due to weaker field confinement. Top illumination is therefore preferred for optimal performance, but bottom illumination may be used in integrated configurations where the substrate is transparent and the superstrate is not used.

A two-dimensional parametric sweep was carried out to systematically explore the optical response of the metasurface at the pump wavelength of 1550 nm. The grating period P varied from 800 nm to 1100 nm in step of 10 nm, while the thickness H of $LiNbO_3$ varied from 500 nm to 1000 nm with the same step size. Periodic conditions were applied along x and y directions to model an infinite metasurface array, while perfectly matched layers (PMLs) were applied at the top and bottom boundaries to suppress artificial reflections.

For each combination of (H, P), linear simulations were first performed at the fundamental pump wavelength to evaluate the reflectance and transmittance. These results were then followed by nonlinear frequency domain simulations to compute the corresponding SHG and THG conversion efficiencies. To identify the optimal geometrical configuration enabling simultaneous emhancement of both nonlinear processes, a figure if merit (FOM) was defined as $\text{FOM} = \log_{10}(\eta_{\text{SHG}} \cdot \eta_{\text{THG}})$,which balances the contributions of SHG and THG over several orders of magnitude.

The optimization procedure consisted of three steps. First, a coarse sweep across the entire parameter space revealed the main resonance features and identfied the region containing the minimum of the FOM. A refined sweep was then performed around this region to narrow down the optimal values of H and P. Finally, a local BOBYQA optimization over P, H, and the duty cycle d_c was applied to precisely locate the maximum nonlinear conversion efficiency.

The linear optical response of the metasurface at the pump wavelength is summarized in the reflectance and transmittance maps as shown in Figure 4.2, plotted as a function of (H, P). Both maps highlight prominent diagonal features characterized by strongly enhanced reflections and suppressed transmission. These diagonal branches correspond to guided-mode resonances (GMRs), arising from phase matching between the normally incident wave and the guided modes supported by the periodically patterned $LiNbO_3$ layer. The periodic grating provides additional in-plane momentum required to couple free-space radiation into these guided modes, which subsequently confine the electromagnetic field within the structure and reradiate into the far field, producing sharp spectral features in the linear response.

To isolate the contribution of graphene, the same metasurface geometry was simulated without the graphene layer. Without graphene, the linear transmittance and reflectance exhibit similar GMR features, but the quality factor increases slightly (from 947 to 1020) due to reduced ohmic losses. The SHG efficiency remains unchanged (graphene does not contribute to SHG), but the THG efficiency drops to near zero, confirming that graphene is the sole source of THG in the hybrid design. This confirms that graphene's third-order nonlinearity is essential for achieving the dual-harmonic functionality.

To analytically interpret the GMRs, the patterned lithium niobate layer was homogenized using effective medium theory, treating the grating as a composite material consisting of lithium niobate pillars embedded in air with a duty cycle of $d_c = 0.75$. The effective permittivity was calculated separately for electric fields polarized parallel ($\epsilon_{\parallel}$) and perpendicular ($\epsilon_{\perp}$) to the pillars, corresponding to TM

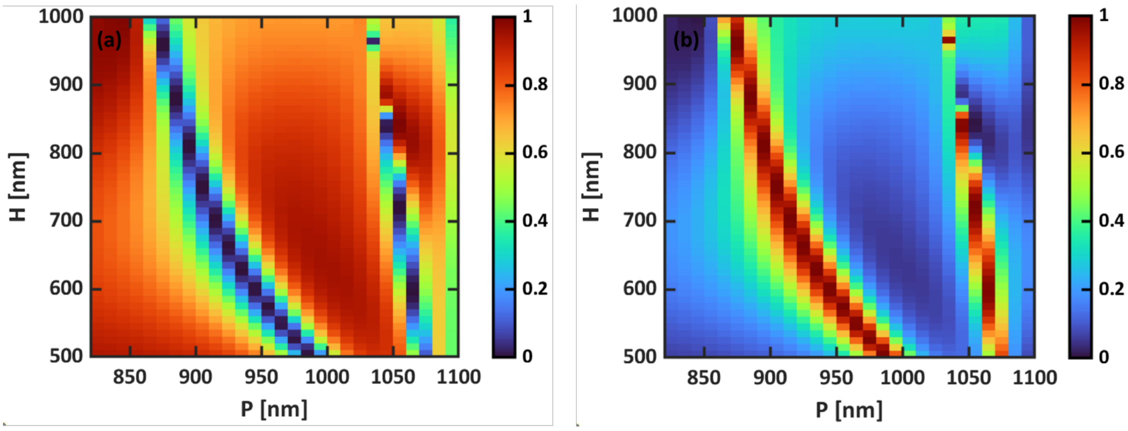

Figure 4.2: 2D map of transmittance and reflectance as a function of (H and P). (a) Transmittance, (b) Reflectance

and TE polarizations, respectively.

$$\epsilon_{\parallel} = d_c\,\epsilon_{\mathrm{LiNbO_3}} + (1 - d_c)\,\epsilon_{\mathrm{air}} \tag{4.25}$$

$$\epsilon_{\perp} = \left(\frac{d_c}{\epsilon_{\mathrm{LiNbO_3}}} + \frac{1 - d_c}{\epsilon_{\mathrm{air}}}\right)^{-1} \tag{4.26}$$

The corresponding effective refractive indices were then computed as $n_{\mathrm{TM}}^{\mathrm{core}} = \sqrt{\epsilon_{\parallel}}$ and $n_{\mathrm{TE}}^{\mathrm{core}} = \sqrt{\epsilon_{\perp}}$. Using these indices, the phase-matching condition for GMR excitation at normal incidence is expressed by the grating equation.

$$\beta = k_0 n_{\mathrm{eff}} = \frac{2\pi m}{P}, \tag{4.27}$$

where k_0 is the free space wavenumber, n_{eff} is the effective index of the guided mode, p is the grating period, and m is the diffraction order. Analytical loci of the fundamental modes (TE_0, TM_0) and the first higher-order mode (TM_1) in the H-P parameter space closely match the resonance branches observed in the numerical simulations, confirming the origin of the guided-mode resonances. The phase-matching condition defines the values of the effective refractive index n_{eff} needed for resonant coupling as a function of the grating period. By applying this condition, analytical loci were constructed in the H–P parameter space corresponding to the excitation of GMRs associated with the fundamental and higher-order modes (TM_0, TE_0, and TM_1). Higher-order modes were found to lie outside the investigated parameter range and were therefore neglected. These loci represent the set of geometrical configurations for which the guided mode becomes phase-matched to free-space radiation and can be excited as leaky resonances. The analytically

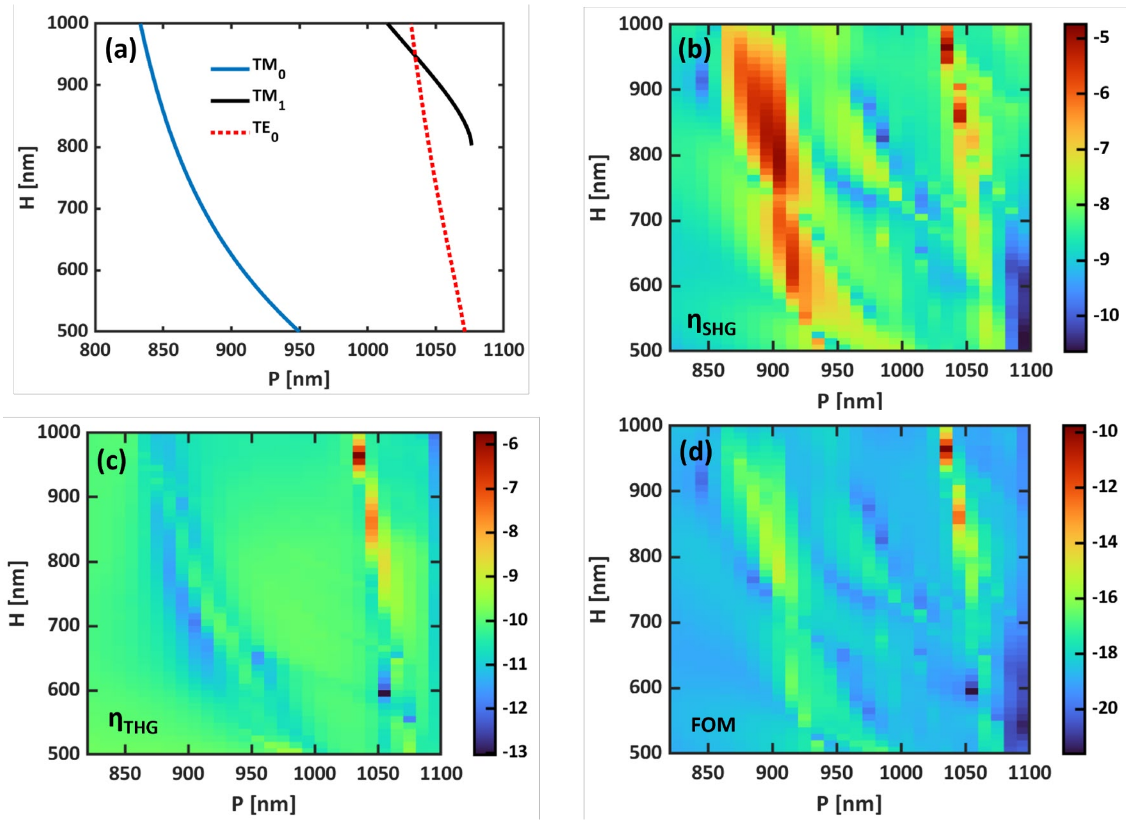

Figure 4.3: 2D color maps of nonlinear efficiencies versus lithium niobate thickness H and grating period P: (a) guided-mode resonance loci (TM_0, TE_0, and TM_1) in the H–P plane; (b) η_{SHG}; (c) η_{THG}; and (d) $FOM = \log_{10}(\eta_{\mathrm{SHG}} \cdot \eta_{\mathrm{THG}})$

derived loci show excellent agreement with the resonance branches observed in the numerical linear response, as shown in Figure 4.3a.

A notable feature is the intersection between the TE_0), and TM_1 branches occurring approximately at $H = 947\,\mathrm{nm}$ and $P = 1035\,\mathrm{nm}$. This crossing corresponds to the simultaneous phase matching of two distinct guided modes at the pump wavelength and plays a key role in enhancing nonlinear frequency conversion processes.

The nonlinear conversion efficiencies for SHG and THG were computed using full-wave finite element simulations over the same coarse H–P parameter space used in the linear analysis. The spatial distribution of $\log_{10}(\eta_{\mathrm{SHG}})$,$\log_{10}(\eta_{\mathrm{THG}})$, and the figure of merit were analyzed to compute the simultaneous enhancement of both nonlinear processes, as shown in Figure 4.3(b)-(d).

$$FOM = \log_{10}(\eta_{\mathrm{SHG}} \cdot \eta_{\mathrm{THG}}) \tag{4.28}$$

The SHG efficiency is predominantly enhanced along the GMR branches identified in the linear response, confirming the role of resonant field confinement. In contrast, the THG enhancement is strongly associated with the TE_0 resonance branch, while only a weaker signature is observed along the TM_0 branch. As a result, The FOM maps reflect a combined behavior, exhibiting strong enhancement along the TE_0 branch and a pronounced maximum in the vicinity of its intersection with the TM_1 branch. This crossing region emerges as the most favorable operating point within the explored parameter space.

From the coarse parameter sweep, the global maximum of FOM is identified around $P \approx 1030\,\mathrm{nm}$ and $H \approx 960\,\mathrm{nm}$, where $\eta_{\mathrm{SHG}} \approx 1.74 \times 10^{-5}$ and $\eta_{\mathrm{THG}} \approx 1.84 \times 10^{-6}$, yielding FOM of approximately -10.49. This coarse analysis provides both physical insight into the resonance mechanisms and an initial estimate of the optimal design region.

To further refine the optimization, a second parametric sweep was performed in a reduced region around the identified maximum. In this refined sweep, the grating period was varied from 1025 nm to 1035 nm and the thickness from 920-100 nm, both with a resolution of 1 nm. The refined maps confirm the presence of the TE_0-TM_1 crossing and reveal a local maximum of SHG at this point, with $\eta_{\mathrm{SHG}} \approx 6.86 \times 10^{-5}$, while $\eta_{\mathrm{THG}} \approx 1.31 \times 10^{-6}$, corresponding to a FOM of approximately -10.04, as shown in Figure 4.4(a-c)

A detailed analysis of the refined parameter space shows that the absolute maxima of the SHG and THG occur at slightly different geometrical configurations, as highlighted in Figure 4.4. THe maximum SHG efficiency is obtained at $P \approx 1027\,\mathrm{nm}$ and $H \approx 996\,\mathrm{nm}$, where $\eta_{\mathrm{SHG}} \approx 1.0 \times 10^{-4}$. Conversely, the maximum THG efficiency occurs near $P \approx 1030\,\mathrm{nm}$ and $H \approx 958\,\mathrm{nm}$, where $\eta_{\mathrm{THG}} \approx 2.24 \times 10^{-6}$. The later configuration coincides with a peak in absorptance, shown in Figure 4.4d, highlighting stronger field confinement and increased nonlinear interaction.

Within the refined region, the maximum value of FOM coincides with the maximum of SHG, indicating that the combined metric is primarily influenced by the SHG contribution in this parameter range, while THG remains comparatively less dominant. The corresponding values at the characteristic points are summarized in Table 1

Table 4.1: Nonlinear efficiencies and FOM at the characteristic points.

Point	P (nm)	H (nm)	η_{SHG}	η_{THG}	FOM
Crossing (local SHG max)	1029	960	6.86×10^{-5}	1.31×10^{-6}	-10.04
Abs. max η_{SHG} (FOM max)	1027	996	1.00×10^{-4}	1.47×10^{-6}	-9.83
Abs. max η_{THG}	1030	958	1.69×10^{-5}	2.24×10^{-6}	-10.42

Finally, a local optimization using the BOBYQA (Bound Optimization BY Quadratic Approximation) algorithm was performed. BOBYQA is a derivative-free optimization method that iteratively constructs a quadratic model of the objective

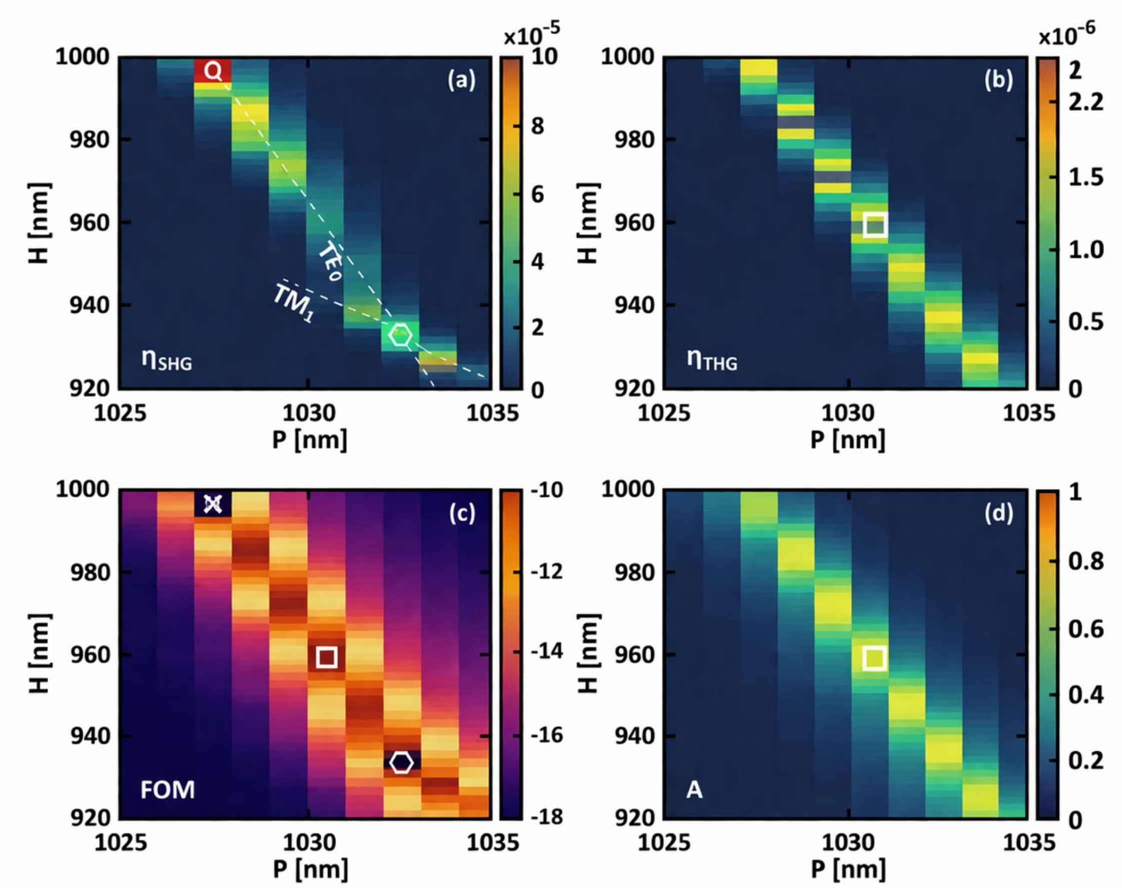

Figure 4.4: Maps of nonlinear conversion efficiencies and FOM versus H and P: (a) η_{SHG}, (b) η_{THG}, and (c) $FOM = \log_{10}(\eta_{\mathrm{SHG}}\eta_{\mathrm{THG}})$. In (c), the white cross, square, and circle denote the maxima of η_{SHG}, η_{THG}, and FOM, respectively.

function (here, the FOM) within a trust region. It is well-suited for expensive simulations because it requires only function evaluations, not gradients. The algorithm was run with initial bounds ±20nm around the best FOM point from the refined sweep, and the duty cycle d_c was allowed to vary between 0.5 and 0.85. The algorithm converged to the same optimal configuration identified in the refined sweep, namely $P \approx 1027\ nm$ and $H \approx 996\ nm$, confirming the robustness and consistency of the optimization procedure.

To assess the robustness of the optimized design, a sensitivity analysis was performed by varying P, H, and W within ±5 nm of the optimal values ($P =$ 1027 nm, $H =$ 996 nm, $W =$ 770 nm). The FOM was recalculated for each perturbation. A ±2 nm variation changes η_{SHG} by less than 15% and η_{THG} by less than 20%, indicating moderate tolerance. Larger deviations (±5 nm) reduce efficiencies by up to 50%, highlighting the need for nanoscale fabrication precision. These tolerances are achievable with electron-beam lithography but may challenge deep-UV lithography.

4.5.1 Electric field distribution

Figure 4.5 shows the spatial distribution of the magnitude of the electric field for the optimized metasurface geometry with a grating period of 1027 nm and lithium niobate thickness of 996 nm, and duty cycle of 0.75, under excitation at the fundamental wavelength of 1550 nm. The field profile illustrated three different observation planes, the top surface of $LiNbO_3$ layer ($z = H$), the middle plane of the lithium niobate pillar ($z = H/2$), and a vertical cross-section via the center of unit cell ($y = 0$). For each plane, the electric field distribution is plotted at the pump, second harmonic, and third harmonic wavelengths, permitting a direct comparison of field confinement, symmetry, and modal structure across different nonlinear processes.

The white square in each panel displays the boundaries of a single unit cell, demonstrating how the electromagnetic fields are distributed to the metasurface geometry. The color scale represents the magnitude of the electric field, normalized to the incident pump amplitude.

Figure 4.5(a-c) displays the electric field magnitude in the in-plane calculated at the top surface of $LiNbO_3$ layer, immediately below graphene sheet. This plane is specifically needed, as it links to the region where both the nonlinearity of graphene and lithium niobate layer, respectively, are strongly driven.

At the pump wavelength shown in Figure 4.5a, the field distribution displays a pronounced localization near the center of the unit cell, with relatively smooth spatial variation and mirror symmetry along the x- and y-axis. This pattern is the feature of a guided-mode resonance excited under normal incidence, where the incident beam couples effectively into a leaky guided mode defended by the lithium niobate pillar. The strong field enhancement near the surface shows efficient energy transfer from free space into the guided mode, which is a prerequisite for enhancing nonlinear optical response.

At the second harmonic wavelength (Figure 4.5b), the field pattern becomes more structured and shows multiple lobes within the unit cell; as compared to fundamental field, the SHG field exhibits stronger spatial modulation and reduced symmetry, reflecting the tensorial nature of second order nonlinear polarization in the $LiNbO_3$ and the different phase matching conditions at the harmonic wavelength. Importantly, the SHG field remains strong, confined within the unit cell and overlaps spatially with the pump field maxima. This strong spatial overlap between the fundamental and second harmonic field enhances the effective nonlinear polarization and contributes directly to the observed high SHG efficiency.

As shown in Figure 4.5c, the third harmonic field shows even more complex distribution, with diagonal characteristics and localized spots inside the unit cell. This complexity arises from the combined effect of nonlinear polarization in graphene and the excitation of higher-order modes at the THG wavelength. Despite the increased spatial complexity, the THG field remains strongly near the graphene-$LiNbO_3$ interface, showing that the nonlinear current induced in the graphene is effectively coupled to radiative modes. This localization confirms that the optimized geometry supports the emission of efficient THG in the zeroth diffraction order.

Figure 4.5(d-f) shows the magnitude of electric field at the mid-plane ($z = H/2$) of the lithium niobate layer. This plane gives insight into how deeply the guided modes penetrate the pillar and how the second and third nonlinear fields develop inside the nonlinear medium. At the pump wavelength (Figure 4.4d), the fundamental field is strongly confined within the lithium niobate layer and exhibits a clear standing wave pattern along the vertical direction, confirms that the pump excitation couples to a pillar-guided mode rather than remaining a surface-localized resonance. The strong field intensity throughout the thickness of the slab is particularly important for SHG, as it increases the effective interaction volume over which the second order nonlinearity is generated.

As depicted in Figure 4.5e, the second harmonic field displays a highly symmetric and well-defined modal structure, with central lobes surrounded by multiple lobes. This pattern reveals a resonant SHG mode supported by the pillar, likely associated with TM_1 guided mode identified in the analytical phase-matching analysis. The strong confinement of the SHG field within the lithium niobate layer highlights that the second harmonic generation is effectively trapped and enhanced by the guided mode resonance before radiating into the far field.

In contrast, at $z = H/2$, the third harmonic field (Figure 4.5f) looks more fragmented and less symmetric. This behavior reflects the fact that the THG is generated from graphene sheets, with the generated field subsequently coupled into pillar modes with reduced penetration depth. The presence of multiple spots inside the $LiNbO_3$ layer reveal efficient coupling between the induced nonlinear polarization in graphene and resonant modes at the pillar, further contributing to overall THG enhancement. Figure 4.5(g-i) illustrates vertical cross sections of the electric field magnitude at $y = 0$ plane, ranging from the substrate region via the $LiNbO_3$ layer and into the glass substrate. These plots give a direct visualization of the electric field confinement vertically and modal profiles associated with the guided-mode resonances.

At the fundamental wavelength, the electric field is strongly concentrated within the graphene-lithium niobate interface, with a clear maximum at the center and then decays towards the edges, confirming the excitation of guided modes, as shown in Figure 4.5g. This vertical confinement is important for obtaining strong local field enhancement and maximizing the strength of nonlinear interactions.

As illustrated in Figure 4.5h, the SHG field shows multiple vertical lobes, consistent with the excitation of resonant guided modes at the SHG wavelength. The

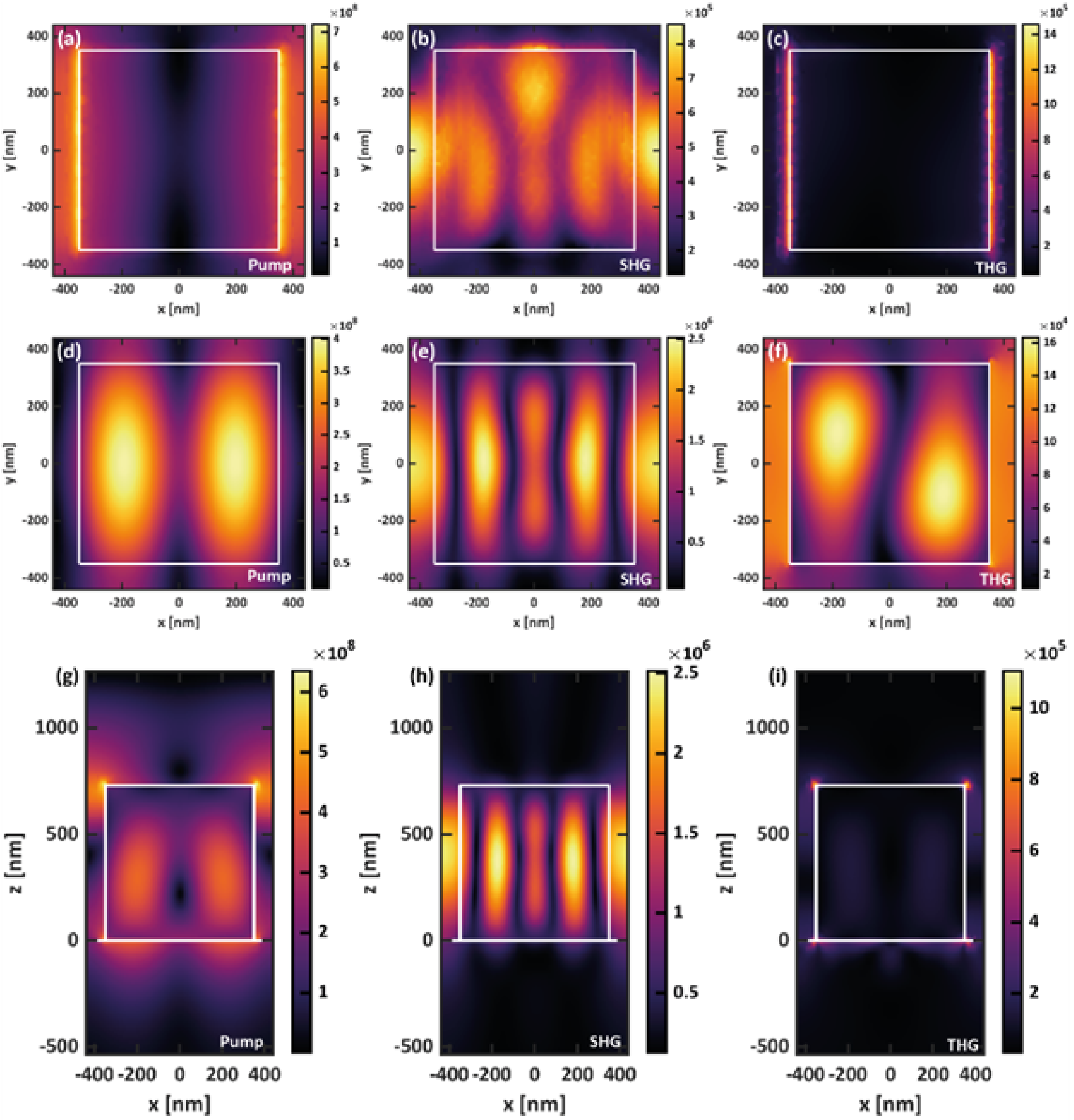

Figure 4.5: Spatial distributions of the electric field magnitude for $P = 1027\,\text{nm}$, $H = 996\,\text{nm}$, and $dc = 0.75$ at $\lambda_{\text{pump}} = 1550\,\text{nm}$. Field profiles are shown along the (a–c) $z = H$, (d–f) $z = H/2$, and (g–i) $y = 0$ planes. Panels (a, d, g) correspond to the fundamental wavelength, (b, e, h) to the second harmonic, and (c, f, i) to the third harmonic.

field maximum is distributed throughout the pillar thickness, showing efficient generation and confinement of SHG inside the $LiNbO_3$ layer, which further supports the analysis of SHG enhancement driven by a guided mode resonance.

Figure 4.5i displays the THG field distribution along the same vertical plane that exhibits a layered structure with pronounced intensity near the top graphene surface and additional lobes extended into the lithium niobate pillar. This behavior demonstrates the hybrid nature of the THG process; the nonlinear source is localized at the graphene interface, while the resulting harmonic field couples to pillar supported resonant modes that shape its vertical distribution and radiation features.

4.5.2 Effects of Fermi Level and Relaxation Time

The response of the optimized metasurface was further investigated as a function of graphene's Fermi level E_F and relaxation time τ. The linear optical response at the pump wavelength $\lambda = 1550\ nm$ is shown in Figure 4.6a, where the transmittance, reflectance, and absorptance are plotted as a function of E_F. For larger relaxation times(τ=0.1 and 0.5 ps), the linear response exhibit a threshold like behavior around $E_F = 0.4eV$. Below this threshold, the reflectance decreases slightly with increasing E_F, while the trasnmittance increases moderately and the absorptance remains nearly constant. At the threshold, the reflectance increases abruptly, the transmittance displays a pronounced feature, and the absorptance drops sharply. For higher values of E_F, the absorptance remains approximately constant, whereas the reflectance continues to increase gradually and the transmittance correspondingly decreases.

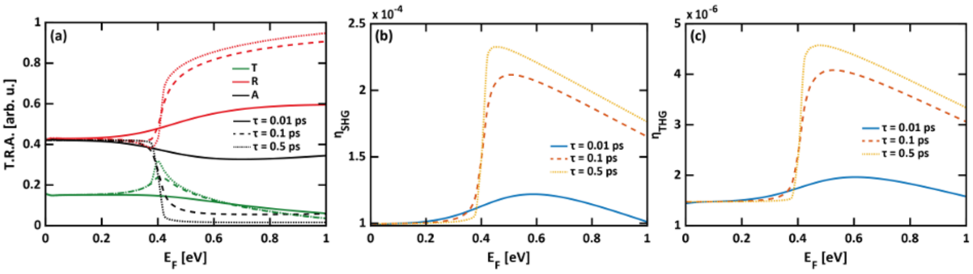

Figure 4.6: Dependence of the linear and nonlinear responses on the graphene Fermi level E_F: (a) reflectance and transmittance, (b) η_{SHG}, and (c) η_{THG}, all as functions of E_F.

In contrast, for $\tau = 0.01$ ps, the threshold behavior becomes significantly smoother. The transmittance decreases monotonically with increasing E_F, without exhibiting a distinct feature. The absorptance also decreases gradually, reaching a minimum around $E_F \approx 0.7$ eV, before slightly increasing again, while the reflectance increases smoothly. OVerall, these trends indicate that variations in E_F primarily modify the balance between reflectance and transmittance at the resonant wavelength, thereby affecting the effective coupling of the incident field into the metasurface.

The corresponding nonlinear conversion efficiencies are presented in Figure 4.6b and Figure 4.6c. Both η_{SHG} and η_{THG} exhibit a non-monotonic dependence on E_F. Beyond $E_F \approx 0.4$ eV, the efficiencies increase rapidly, reaching maximum values of

$\eta_{\text{SHG}} \approx 2.33 \times 10^{-4}$ at $E_F \approx 0.45\,\text{eV}$, and $\eta_{\text{THG}} \approx 4.57 \times 10^{-6}$ at $E_F \approx 0.474\,\text{eV}$ for $\tau = 0.5\,\text{ps}$. For larger values of E_F, both efficiencies decrease.

A similar trend is observed for lower relaxation times, although with reduced peak values and a smoother dependence on E_F. The stronger modulation observed for larger τ, consistent with reduced damping in the graphene conductivity, which enhances the influence of E_F on the resonant field amplitude. Overall, the maxima of the nonlinear efficiencies occur within an intermediate range of E_F, where the resonant field enhancement is significant but not yet limited by increases in reflectance.

The relaxation time τ characterises the scattering rate of charge carriers in graphene. The range τ = 0.1–0.5 ps was chosen based on reported values for CVD-grown graphene on SiO_2 or $LiNbO_3$ substrates at room temperature. For high-quality exfoliated graphene on h-BN, τ can exceed 1 ps, but practical devices use CVD graphene with $\tau \approx$ 0.1–0.5 ps [221, 222]. The lower bound (0.1 ps) corresponds to moderately defective graphene, while the upper bound (0.5 ps) represents state-of-the-art CVD material. The influence of τ on the nonlinear response is shown in Figure. 4.6: higher τ yields stronger modulation of conversion efficiency with E_F, but the peak values remain within the same order of magnitude.

Furthermore, the nonlinear efficiencies exhibit relatively broad maxima over finite intervals of E_F, highlighting that the enhancement of SHG and THG is not confined to a narrow operating point. Varying τ primarily affects the peak amplitudes without significantly altering the overall trends, suggesting that moderate changes in graphene quality do not substantially impact device performance within the considered parameter range.

4.5.3 Linear and Nonlinear Spectral Response

The spectral response of the optimized metasurface in the vicinity of the pump wavelength is shown in Figure 4.7. In Figure 4.7a, the linear transmittance, reflectance, and absorptance are plotted as a function of the wavelegnth λ , revealing a narrow resonance centered near 1550 nm. The linear spectra exhibit a pronounced Fano-like resonance, with transmittance and reflectance showing complementary extrema in either side of the resonance, slightly shifted in wavelength. The absorptance highlights a sharp peak of approximately 42% at teh resonance, with a full width at half maximum (FWHM) of about 1.64 nm, corresponding to a quality factor of approximately 947.

The nonlinear conversion efficiencies are illustrated in Figure 4.7b. Both SHG and THG exhibit strongly wavelength-selective response, with maxima occuring near the linear resonance. The spectral width of nonlinear responses are significantly narrower than that of the linear response, with linewidths of approximately 1.04 nm ($Q \approx 1488$) for SHG and 0.835 nm ($Q \approx 1857$) for THG.

The reduction in linewidth arises from the nonlinear dependence on the local

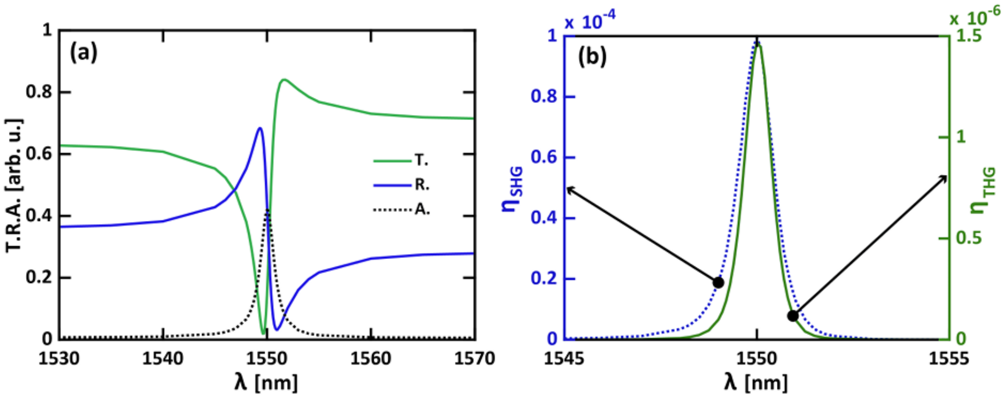

Figure 4.7: (a) Transmittance (green solid curve), reflectance (blue solid curve), and absorptance (black dotted curve) as functions of wavelength. (b) Second- and third-harmonic generation efficiencies, η_{SHG} (left axis, blue dotted curve) and η_{THG} (right axis, green solid curve), as functions of wavelength.

electric field at the pump wavelength. Since the SHG and THG efficiencies scale with the fourth and sixth powers of the field amplitude, respectively, even small detuning from resonance leads to a rapid decrease in conversion efficiency. Consequently, the THG response exhibits a slightly narrower spectral width than the SHG response.

Overall, the nonlinear spectral behavior closely follows the resonant field enhancement at the fundamental wavelength, highlighting that the wavelength selectivity of SHG and THG is governed by the same guided-mode resonance responsible for the linear response. Additional simulations performed at $E_F = 0.45\,\mathrm{eV}$ show a negligible shift in the resonance position (below 0.1 nm) compared to the case of $E_F = 0\,\mathrm{eV}$. THis confirms that the variations in E_F do not significantly affect the spectral position of the guided-mode resonance, but primarily influences its coupling strength and the balance between reflection and transmission

Table 2 presents a comparative overview of representative nonlinear structures addressed in literature for SHG and THG, including the need of pump intensities and obtained conversion efficiencies ((η_{SHG}) and (η_{THG})). While higher efficiencies were exhibited by some previously addressed designs, the emphasis of current work is mainly different. Here, we design and investigate a hybrid nonlinear metasurface based on graphene-lithium niobate, a configuration that, to the best of our knowledge, has not been reported earlier for simultaneous second harmonic generation (SHG) and third harmonic generation (THG).

The results shown in the chapter should therefore be regarded as proof of concept, highlighting that $LiNbO_3$ and graphene can be integrated effectively to support both SHG and THG under a fundamental wave excitation. Instead of pointing out to outperform existent efficiency benchmark, the main goal of this study is to

Table 4.2: Literature benchmarks for SHG/THG in metasurfaces and related platforms.

Platform/Structure	**Proc.**	**Pump λ**	**Pump Int./Field**	η	**Ref.**
Monolithic $LiNbO_3$ metasurface (corrugated NIR)	SHG	1.5 μm	1 GW/cm^2	$> 10^{-5}$	[160]
Thin-film $LiNbO_3$ heterostructure cavity	SHG	telecom–vis	cavity-enh. (mW)	10^{-1}–1.5×10^{-1}	[223]
AlGaAs nanoantenna	SHG	1550 nm	3.4 GW/cm^2	2×10^{-5}	[224]
AlGaAs nanocylinders	SHG	1554 nm	1 GW/cm^2	$> 10^{-5}$	[225]
AlGaAs metasurface quasi-BIC	SHG	NIR	10 MW/cm^2	2.5×10^{-2}	[226]
Graphene + photonic grating (THz)	THG	0.3–3 THz	$E \approx 30$ kV/cm	10^{-3}	[227]
Graphene (single layer), free-space THz	THG	∼0.7 THz	$E \approx$ tens kV/cm	$\geq 10^{-3}$	[228]
$LiNbO_3$ metasurface near-BIC (theory)	SHG	1550 nm	1.3 GW/cm^2	1.5×10^{-5}	[229]
$LiNbO_3$–Graphene metasurface	SHG/THG	1550 nm	1 GW/cm^2	SHG: 2.33×10^{-4} THG: 4.57×10^{-6}	This Ph.D. Thesis

numerically develop the viability and physical benefits of this hybrid mechanism. By further optimizing the metasurface geometry, resonant conditions and parameters of both materials, significantly higher nonlinear conversion efficiencies ((η_{SHG}) and (η_{THG})) are expected to be obtainable.

An imperative aspect of the simulation structure is that the contribution of the nonlinearity of both materials is deliberately isolated. In the proposed metasurface, the nonlinearity originates from its bulk lithium niobate, while third-order nonlinear polarization in graphene produced the third harmonic generation. The cascaded nonlinearity is suppressed in our simulation, such as SHG followed by the sum-frequency generation (SFG) that permits a direct and explicit estimation of each nonlinearity supported by the metasurface and such a clear isolation of nonlinearity approach is especially feasible for understanding and manufacturing multifunctional nonlinear systems.

From application point of view, this hybrid approach is highly relevant to integrated optics. The ability to produce dual harmonics in a single platform can significantly reduce device footprints and simplify architecture at the system level. This mechanism holds promise for uses in compact multi-wavelength laser sources, emerging concepts in optics, ultrafast spectroscopy, neuromorphic computing and nonlinear signal processing [230].

From the perspective of fabrication, the proposed hybrid metasurface is matched with recognized nanofabrication techniques. A thin layer of lithium niobate can be placed on a glass (SiO_2) substrate using pulse laser deposition and subsequently, a single layer graphene (SLG) grow through chemical vapor deposition [231], can be transferred at the top of $LiNbO_3$ using a standard wet-transfer process [232]. Electron-beam lithography is used to define the pattern of metasurface, followed by selective etching to form the periodic grating. The resulting nonlinear metasurface integrated the strong second-order nonlinear response of lithium niobate with eh electrically tunable third-order nonlinear response of graphene, enabling simultaneous generation of second and third harmonics within a single, compact system architecture.

At near-infrared fundamental pup, the optical absorption of graphene is primarily governed by electronic transitions and can be strongly reduced via electrostatic gating. When Fermi levels exceed approximately 0.4 eV, Pauli blocking suppresses interband transitions at the pump wavelength of 1550 nm [233–235]. In this regime, graphene operates in a low-loss, predominantly dispersive state, with absorption well below its universal value of 2.3%. This property is crucial for achieving efficient nonlinear conversion, as it minimizes pump depletion while enabling active electrical tuning of the metasurfacce response.

The losses in graphene increase efficiently at the harmonic wavelength. At the second harmonic wavelength ($\lambda_{\mathrm{SHG}} = 775\,\mathrm{nm}$), the photon energy exceeds twice the achievable Ferm level, and the interband transitions are no longer Pauli block, leading to the graphene absorption at the SHG wavelength and the losses even become over pronounced at the third-harmonic wavelength of 517 nm, where graphene absorption is dominated by interband transitions in the visible spectral range and is largely insensitive to electrical tuning [236–238].

Despite these increased losses at the harmonic wavelengths, efficient SHG and THG can still be achieved due to the strong enhancement electromagnetic field and subwavelength confinement delivered by the guided-mode resonances of the metasurface. Crucially, exciting graphene in a low-loss regime at the pump wavelength ensures that the nonlinear conversion process is not limited by excessive absorption of the pump field. In this context, graphene primarily functions as a tunable nonlinear boundary layer rather than as a dominant dissipative element, enabling effective harmonic generation while establishing electrical control over the system response.

For experimental realization, the optimized geometry requires P and H control within ±2 nm. This is feasible with EBL but alternative methods (nanoimprint lithography, helium-ion beam milling) may offer lower cost with slightly reduced precision. The simulations assume 1 GW/cm^2, which is typical for femtosecond pulsed lasers (e.g., 100 fs pulses, 1 kHz repetition rate). Continuous-wave operation would require much higher field enhancement to reach comparable intensities. The high Q factor ($\approx$950) makes the resonance sensitive to ambient temperature changes and inhomogeneities in the $\mathrm{LiNbO_3}$ layer. Active stabilization or the use of a slightly lower-Q design may be preferable for practical devices. Electrical contacts to the graphene layer can be deposited using metal electrodes at the edges of the metasurface, avoiding interference with the optical field in the center. A back-gate or side-gate scheme (as in Chapter 2) can be employed.

While electron-beam lithography (EBL) offers the required sub-10 nm resolution, it is slow and expensive for large-area production. For cost-effective manufacturing, nanoimprint lithography (NIL) or deep ultraviolet (DUV) lithography can be used, provided the critical dimensions ($\sim$770 nm) are within the resolution of these methods. NIL has demonstrated pattern transfer of 100 nm features over 4-inch wafers. Another alternative is focused helium-ion beam milling, which can directly define the grating in $LiNbO_3$ without resist processing, but it is also expensive. For research prototypes, EBL remains the most reliable choice.

4.6 Conclusion

This chapter presents a numerical study of a hybrid graphene-$LiNbO_3$ nonlinear metasurface operating at a pump wavelength of 1550 nm. Guided-mode resonances arising from the engineered grating geometry investigated using full-wave simulations and effective-index calculations. Distinct resonance brances corresponding to the TM_0, TE_0, and TM_1 modes were identified and confirmed via phase-matching analysis.

The nonlinear response shows enhanced second- and third-harmonic generation near these resonant branches, with simultaneous enhancement occurring close to the crossing of TE_0 and TM_1 modes. For the optimized structure, SHG and THG efficiencies on the order of 10^{-4} and 10^{-6}, respectively, are achieved under a pump intensity of 1 GW/cm^2.

Furthermore, tuning the graphene chemical potential modifies the resonance coupling strength without significantly shifting its spectral position, thereby affecting the nonlinear response through changes in the resonant field amplitude. These results demonstrate that hybrid graphene-$LiNbO_3$ metasurfaces provide an effective platform for simultaneous second- and third-harmonic generation controlled by guided-mode resonances.

Chapter 5

Future Work

Future research can further extend the capabilities of the transparent graphene-based reconfigurable antennas and nonlinear metasurfaces presented in this work. Although the proposed designs demonstrate the control of radiation patterns and nonlinear optical enhancement, several additional design strategies and tuning mechanisms can be explored to improve the level of reconfigurability, radiation performance, and nonlinear conversion efficiency.

For the transparent graphene antenna employing electrostatic biasing, future work may focus on incorporating parasitic elements in combination with the graphene radiating structure. This inclusion of carefully designed parasitic elements surrounding the main radiating dipole could enable improved beam steering and more precise control of the radiation pattern. By adjusting the electrostatic bias applied to graphene parasites, the current distribution along the radiating structure can be dynamically modified, which would allow antenna to achieve controlled scanning across the azimuthal plane. In particular, a parasitic configuration may allow beam steering with scanning angles in the range of approximately 15-30 degrees while maintaining coverage across the full 0-360 degree azimuthal plane. Such a configuration could significantly improve directional control and radiation efficiency while preserving the transparency and compact nature of the antenna.

Moreover, future work may also explore radiation pattern reconfigurability in the elevation plane. In the present study, the antenna configuration primarily enables pattern reconfigurability along the azimuthal direction. However, several antenna geometries could be investigated to achieve elevation angle control as well. One potential approach is to replace the conventional dipole structure with alternative antenna configurations such as the Alford dipole antenna, which is well known for its symmetric radiation properties and improved omnidirectional characteristics. By integrating graphene elements within an Alford dipole configuration and applying electrostatic biasing, it may be possible to achieve both azimuthal and elevation pattern control while maintaining antenna transparency and tunability. Other hybrid antenna structures combining dipole and loop-type geometries could also be explored to further enhance pattern reconfigurability.

Similarly, the graphene-patterned reconfigurable antenna operating under in-plane and out-of-plane magnetic biasing offers additional opportunities for future development. Magnetic biasing introduces anisotropic conductivity in graphene, which enables dynamic modification of the electromagnetic response of the antenna. In future studies, parasitic antenna elements could also be incorporated within the magnetically biased configuration to further improve radiation control and beam steering capabilities. By combining magnetic biasing with optimized parasitic element placement, the antenna may achieve more flexible radiation pattern tuning and enhanced scanning performance across the azimuthal plane.

Moreover, the use of both in-plane and out-of-plane magnetic fields can be further investigated to achieve more complex radiation control mechanisms. For instance, applying different magnetic field orientations to separate graphene regions could allow independent control of the current distribution along the antenna surface. Such a strategy may enable multi-directional beam steering or adaptive radiation pattern shaping. This approach could be particularly useful in terahertz communication systems, where dynamic beam control is required for adaptive links and high-capacity wireless communication.

Another potential direction for future research is the development of hybrid electrostatic-magnetic tuning mechanisms. By simultaneously applying electrostatic biasing and magnetic tuning to graphene structures, it may be possible to achieve additional degrees of freedom in antenna reconfigurability. Such hybrid tuning mechanisms could allow independent control of frequency tuning, radiation pattern shaping, and beam steering within a single antenna platform. This type of multifunctional reconfigurable antenna could play an important role in future adaptive communication systems, particularly in the terahertz and millimeter-wave regimes.

In addition to antenna designs presented in this work, the graphene-$LiNbO_3$ nonlinear metasurface studies for dual harmonic generation can also be further developed in several ways. The current study demonstrates simulatenous enhancement of second-harmonic generation (SHG) and third-harmonic generation (THG) through guided-mode resonances supported by the metasurface structure. However, future research could focus on achieving active control over the nonlinear optical response of the metasurface.

Another promising direction is the exploration of tunable phase-matching conditions within the metasurface structure. Since the nonlinear response is strongly dependent on resonance coupling and field localization, small changes in the structural parameters or graphene chemical potential may allow dynamic control of the nonlinear conversion efficiency. Implementing electrically tunable metasurface elements could therefore enable real-time control of harmonic generation processes, which would be highly valuable for applications such as tunable light sources, frequency converters, and nonlinear optical signal processing.

Overall, the results presented in this thesis demonstrate the significant potential of graphene-based reconfigurable antennas and hybrid graphene-lithium niobate nonlinear metasurfaces. Future research focusing on parasitic antenna configurations, multidimensional radiation pattern control, hybrid tuning mechanisms, and actively tunable nonlinear metasurfaces may further expand the capabilities of these devices. These advancements could contribute to the development of next-generation reconfigurable communication systems and tunable nonlinear photonic devices operating in the terahertz and optical frequency regimes.

Appendix A

CST Studio Suite

A.1 CST Simulation Parameters

Table A.1: CST simulation definitions for the graphene dipole antenna

Parameter	**Notation**
Solver	Transient (time domain)
Frequency range	187 – 214 GHz
Boundary conditions	Open (Add space = $540\,\mu$m)
Mesh	No mesh adaptation
Excitation	Discrete Port
Graphene modeling	Hansen model implemented via VBA

Discrete port defined with $180\,\mu\text{m} \times 130\,\mu\text{m}$ dimensions and electrical shielding. No add space is applied at the port boundary.

A.2 Validation and Computational Considerations

- **Convergence:** Mesh convergence was verified by monitoring S_{11} variations below 0.5 dB.
- **Reproducibility:** Selected coding patterns (e.g., V3, H37) were re-simulated to ensure consistent results.
- **Computational cost:** Approximately 10–15 minutes per simulation on a standard workstation.

Appendix B

MATLAB

B.1 MATLAB Post-Processing

MATLAB was extensively used in this research as a post-processing and data analysis platform to complement the electromagnetic simulations performed in CST Studio Suite and COMSOL Multiphysics. While CST and COMSOL provided accurate full-wave numerical solutions, MATLAB enabled advanced data processing, visualization, parametric analysis, and nonlinear curve fitting in a flexible computational environment. The integration of MATLAB into the workflow ensured systematic analysis of large datasets, automated parameter extraction, and clear graphical representation suitable for publication and thesis documentation.

The simulation tools were primarily used to generate S-parameters, electric field distributions, surface currents, gain values, radiation efficiency, and nonlinear harmonic amplitudes. These outputs were exported in ASCII or Touchstone (.s2p) formats and then imported into MATLAB for detailed analysis. MATLAB scripts were developed to automate data loading, normalization, filtering, peak detection, bandwidth calculation, and multi-parameter comparison across biasing conditions and geometric variations.

One of the main tasks performed in MATLAB was post-processing of S-parameter data. The reflection coefficient S_{11}, transmission coefficient S_{21}, and related scattering parameters were extracted from CST frequency-domain simulations. Although CST provides built-in visualization tools, MATLAB allowed deeper quantitative analysis. After importing the complex S-parameter data, the magnitude in decibels was calculated using:

$$S_{11}(\text{dB}) = 20\log_{10}|S_{11}| \tag{B.1}$$

This enabled precise determination of resonant frequencies by identifying minima in the reflection coefficient curve. A peak-search algorithm was implemented to automatically locate resonance dips and calculate their corresponding bandwidths at the −10 dB level. This was particularly useful when analyzing multiple electrostatic biasing states of the programmable graphene antenna, where resonance shifting behavior needed to be quantified accurately.

In addition to resonance extraction, MATLAB was used to compute quality factor values from the −3 dB bandwidth definition. The quality factor was estimated using:

$$Q = \frac{f_r}{\Delta f} \tag{B.2}$$

where f_r is the resonant frequency and Δf is the bandwidth. This allowed evaluation of how graphene chemical potential tuning affected antenna selectivity and confinement properties.

For radiation performance evaluation, realized gain and radiation efficiency data exported from CST were processed in MATLAB. Gain versus frequency curves were plotted for different bias voltages, enabling direct comparison of performance under various electrostatic tuning conditions. MATLAB was also used to normalize gain values, smooth numerical noise, and overlay multiple parametric cases within a single figure for clearer interpretation.

Radiation efficiency was analyzed by extracting both total efficiency and radiation efficiency values. These were plotted against frequency and bias voltage to evaluate losses introduced by graphene conductivity variation. Since graphene conductivity depends strongly on chemical potential and relaxation time, efficiency trends were examined as a function of these parameters. MATLAB scripts were written to compute percentage variation in efficiency and identify optimal biasing points.

Parametric sweeps formed a major part of the programmable antenna study. In CST, electrostatic bias voltage was varied to tune the graphene chemical potential using a VBA-based implementation of the Hanson conductivity model. For each bias state, S-parameters and gain were exported. MATLAB was then used to organize these datasets into multidimensional arrays indexed by frequency and bias voltage. Surface plots and contour plots were generated to visualize resonance shifting as a function of applied bias.

For example, resonance frequency versus chemical potential curves were obtained by mapping extracted resonant frequencies against corresponding voltage values. Curve fitting tools in MATLAB were applied to determine whether the resonance shift followed a linear, quadratic, or square-root dependence. This provided insight into the physical relationship between graphene conductivity and antenna effective electrical length.

In the nonlinear optical part of the study, MATLAB was used to process harmonic generation data exported from COMSOL. The fundamental field amplitude and harmonic field amplitude were analyzed to compute conversion efficiency. The second-harmonic generation efficiency was calculated as:

$$\eta_{SHG} = \frac{P_{2\omega}}{P_{\omega}} \tag{B.3}$$

and similarly for third-harmonic generation. MATLAB enabled logarithmic scaling of harmonic intensity and comparison across different excitation powers. Since nonlinear response typically follows a power-law dependence, curve fitting was performed using polynomial regression in log–log space to confirm quadratic behavior for SHG and cubic behavior for THG.

Another important application of MATLAB was curve fitting of graphene conductivity and nonlinear susceptibility data. Using numerical data derived from the Kubo model, fitting procedures were applied to approximate frequency-dependent conductivity with rational functions. This facilitated simplified analytical modeling and helped validate CST and COMSOL implementations.

MATLAB's optimization toolbox was also used to estimate relaxation time and effective mobility parameters by minimizing the difference between simulated and theoretical conductivity curves. This provided consistency between electromagnetic simulation and theoretical graphene models.

Visualization played a significant role in thesis preparation. MATLAB was used to generate high-resolution publication-quality figures with customized axis labels, legends, LaTeX formatting, and consistent scaling. Multi-panel plots comparing S_{11}, gain, and efficiency under different magnetization or bias conditions were created to clearly demonstrate performance trends. Automated scripts ensured reproducibility of figures whenever simulation data were updated.

Data smoothing and filtering techniques were occasionally applied to remove numerical artifacts arising from discrete frequency sampling. However, care was taken to preserve physical accuracy and avoid artificial distortion of resonance characteristics.

MATLAB was also used to calculate derived electromagnetic quantities such as effective refractive index, propagation constant, and impedance from simulation data. In metasurface analysis, phase response data were unwrapped to obtain continuous phase variation, enabling evaluation of programmable phase tuning capability.

To ensure reliability, all MATLAB scripts were modular and documented. Separate functions were written for data import, resonance detection, bandwidth calculation, harmonic efficiency computation, and plotting. This structured approach reduced human error and allowed rapid processing of large parametric datasets.

Appendix C

COMSOL Multiphysics

C.1 COMSOL Multiphysics Simulation Settings

This appendix details the simulation settings used for:

1. The graphene-based programmable dipole antenna (Chapter 2 and 3)
2. The hybrid graphene-lithium niobate nonlinear metasurface (Chapter 4)

All electromagnetic simulations were performed using COMSOL Multiphysics (version 6.3).

C.2 Graphene Dipole Antenna Simulations (Chapters 2 and 3)

C.2.1 Physics Interface

The simulations were performed using the **Electromagnetic Waves, Frequency Domain** (emw) physics interface.

Table C.1: Physics interface settings for antenna simulations

Parameter	**Setting**
Physics interface	Electromagnetic Waves, Frequency Domain
Equation form	Wave Equation, Electric
Frequency range	240-280 GHz
Resonance frequency	260 GHz

C.2.2 Boundary Conditions

- **Perfect Electric Conductor (PEC):** Applied to metal gate electrodes and ground planes.
- **Lumped Port:** Used to excite the dipole antenna with a specified impedance (50 Ω).
- **Surface Current Density:** Applied to model the graphene layer using the Drude-like intraband conductivity.
- **Scattering Boundary Condition (SBC):** Applied to outer boundaries to absorb outgoing radiation.
- **Far-Field Domain:** Defined to compute radiation patterns and far-field gains.
- **Initial Values:** Electric field components set to zero as initial conditions.

C.2.3 Mesh Settings

A physics-controlled mesh was used with the following parameters:

Table C.2: Mesh settings for antenna simulations

Parameter	**Setting**
Mesh type	Physics-controlled mesh
Element size	Finer
Maximum mesh element size control	Frequency
Maximum frequency	f_0 Hz (center frequency)
Angular tolerance	$\pi/5$ rad
Size type	Relative
Relative size to default mesh	0.02

C.2.4 Graphene Modeling

Graphene was modeled as an infinitesimally thin surface using the Surface Current Density boundary condition. The conductivity was defined using the Hansen model (Drude-like intraband conductivity) implemented via a custom VBA script:

$$\sigma_{\text{Drude}}(\omega) = \frac{ie^2\mu_c}{\pi\hbar^2(\omega + i\tau^{-1})} \tag{C.1}$$

where $e = 1.602 \times 10^{-19}$ C (electron charge), $\hbar = 1.055 \times 10^{-34}$ J·s (reduced Planck constant), $\mu_c = 0$ eV (OFF state) or 1 eV (ON state) for electrostatically biased (Chapter 2), μ_c determined by magnetic bias (Chapter 3), $\tau = 0.5$ ps (carrier relaxation time for CVD graphene)

C.3 Nonlinear Graphene-Lithium Niobate Metasurface Simulations (Chapter 4)

C.3.1 Model Overview

The nonlinear metasurface simulations involve three frequency-domain physics nodes:

- **Pump frequency (ewfd1):** Fundamental wave at $\lambda = 1550$ nm
- **SHG frequency (ewfd_shg):** Second harmonic generation at $\lambda = 775$ nm
- **THG frequency (ewfd_thg):** Third harmonic generation at $\lambda = 517$ nm

C.3.2 Pump Frequency Node (ewfd1)

Table C.3: Pump frequency node settings

Node	**Description**
Wave Equation, Electric 1	Solves Maxwell's equations for the pump field
Perfect Electric Conductor 1	PEC boundary condition
Initial Values 1	Zero initial electric field
Scattering Boundary Condition 1	Absorbs outgoing radiation
Wave Equation, metasurface	Material properties of $LiNbO_3$ pillars
Wave Equation, substrate	Material properties of SiO_2 substrate
Surface Current Density 1	Graphene layer (linear conductivity)
Port 1	Input port for pump excitation
Orthogonal Polarization 1	Defines polarization state
Port 2	Output port
Periodic Condition x	Floquet periodicity in x-direction
Periodic Condition y	Floquet periodicity in y-direction

C.3.3 Second Harmonic Generation Node (ewfd_shg)

The SHG node solves for the second harmonic field generated by the $\chi^{(2)}$ nonlinearity of $LiNbO_3$.

Table C.4: SHG frequency node settings

Node	**Description**
Wave Equation, Electric 1	Solves Maxwell's equations at SHG frequency
Perfect Electric Conductor 1	PEC boundary condition
Initial Values 1	Zero initial electric field
Scattering Boundary Condition 1	Absorbs outgoing SHG radiation
Wave Equation, metasurface	$LiNbO_3$ properties at SHG frequency
Wave Equation, substrate	SiO_2 properties at SHG frequency
External Current Density	$\mathbf{J}_{\mathrm{NL}} = -i\omega\varepsilon_0\chi^{(2)} : \mathbf{EE}$
Periodic Condition x	Floquet periodicity in x-direction
Periodic Condition y	Floquet periodicity in y-direction
Port 1	SHG output port
Port 2	SHG output port

C.3.4 Third Harmonic Generation Node (ewfd_thg)

The THG node solves for the third harmonic field generated by the $\chi^{(3)}$ nonlinearity of graphene.

Table C.5: THG frequency node settings

Node	**Description**
Wave Equation, Electric 1	Solves Maxwell's equations at THG frequency
Perfect Electric Conductor 1	PEC boundary condition
Initial Values 1	Zero initial electric field
Surface Current Density 1	Graphene third-order nonlinear conductivity
Scattering Boundary Condition 1	Absorbs outgoing THG radiation
Wave Equation, metasurface	$LiNbO_3$ properties at THG frequency
Polarization 1	$\mathbf{P}_{\mathrm{NL}} = \varepsilon_0\chi^{(3)} : \mathbf{EEE}$
Periodic Condition x	Floquet periodicity in x-direction
Periodic Condition y	Floquet periodicity in y-direction

C.3.5 Definitions and Variables

The following definitions were used in the simulations:

Table C.6: Definitions and variables

Variable	**Description**
AV Reflection, 0th order (aveop1)	Average reflection at fundamental frequency
AV Transmission, 0th order (aveop2)	Average transmission at fundamental frequency
MAX Maximum 1 (maxop1)	Maximum field enhancement
fdu Integration 1 (intop1)	Integration for SHG efficiency
fdu Integration 2 (intop2)	Integration for THG efficiency
Boundary System 1 (sys1)	Coordinate system for periodic boundaries
Artificial Domains	PML regions for wave absorption

C.3.6 Nonlinear Material Models

Lithium Niobate ($\chi^{(2)}$)

The second-order nonlinearity of $LiNbO_3$ is described by the tensor $\chi^{(2)}$ with coefficients:

$$d_{31} = -3.2 \text{ pm/V}, \tag{C.2}$$

$$d_{22} = 1.9 \text{ pm/V}, \tag{C.3}$$

$$d_{33} = -19.5 \text{ pm/V} \tag{C.4}$$

The dominant contribution to SHG comes from d_{33} under x-polarized pump.

Graphene ($\chi^{(3)}$)

The third-order surface conductivity of graphene is given by:

$$\sigma_s^{(3)}(3\omega; \omega, E_F, \tau, T) = \frac{ie^4}{48\pi\hbar^3\omega^4}\left[\tanh\left(\frac{\hbar\omega}{4k_BT}\right) + i\frac{\hbar}{\tau\omega}\right] \tag{C.5}$$

C.3.7 SiO_2 Substrate ($\chi^{(3)}$)

The substrate contributes a weak third-order nonlinearity:

$$\chi^{(3)}_{SiO_2} = 2 \times 10^{-22} \text{ m}^2/\text{V}^2 \tag{C.6}$$

C.3.8 Mesh Settings for Metasurface Simulations

C.3.9 Solver Settings

C.3.10 Conversion Efficiency Calculation

The SHG and THG conversion efficiencies were calculated using:

Table C.7: Mesh settings for nonlinear metasurface simulations

Parameter	**Setting**
Mesh type	Physics-controlled mesh
Element size	Finer
Maximum mesh element size	$\lambda_{\text{pump}}/20$ (77.5 nm)
Resolution of narrow regions	Enabled
Refine at boundaries	Enabled

Table C.8: Solver settings for nonlinear metasurface simulations

Parameter	**Setting**
Solver type	Direct (MUMPS)
Frequency sweep	Single frequency per node
Tolerance	1×10^{-6}
Maximum iterations	500
Nonlinear method	Newton (for coupled SHG/THG)

$$\eta_{\text{SHG}} = \frac{P_{\text{SHG}}}{P_{\text{pump}}}, \tag{C.7}$$

$$\eta_{\text{THG}} = \frac{P_{\text{THG}}}{P_{\text{pump}}} \tag{C.8}$$

where P_{pump}, P_{SHG}, and P_{THG} are the powers of the pump, second harmonic, and third harmonic waves, respectively, obtained via integration over the output port.

C.4 Validation and Computational Considerations

- **Convergence:** Mesh convergence was verified by monitoring S_{11} variations below 0.5 dB for antenna simulations, and FOM variations below 5% for metasurface simulations.
- **Reproducibility:** Selected coding patterns (e.g., V3, H37) and optimized geometries were re-simulated to ensure consistent results.
- **Computational cost:**
  - Antenna simulations: 10–15 minutes per simulation
  - Metasurface simulations (three coupled frequency nodes): 30–45 minutes per simulation
- **Hardware:** Intel Xeon W-2245 (8 cores, 3.9 GHz), 64 GB RAM

- **Software version:** COMSOL Multiphysics 6.3 (Build: 6.3.0.290, win64)

Bibliography

[1] M. Ahmed, A. Wahid, W. U. Khan, F. Khan, A. Ihsan, Z. Ali, K. M. Rabie, T. Shongwe, and Z. Han. A survey on ris advances in terahertz communications: Emerging paradigms and research frontiers. *IEEE Access*, 12:173867–173901, 2024.

[2] Pranali Langde, Tapan Kumar Jain, Mayur R. Parate, and Sandeep Kumar Singh. A journey of terahertz communication: An irs integration perspective. *Physical Communication*, 68:102572, 2025.

[3] J. Liu, X. Yang, Y. Wei, and F. Zhao. Integrated thz/fso communications: A review of practical constraints, applications and challenges. *Micromachines*, 16(11):1297, 2025.

[4] Y. Zhou, Y. Huang, Y. Jin, Z. Yao, C. He, and X. Xu. Terahertz properties of graphene and graphene-based terahertz devices. *Chinese Journal of Lasers*, 46(6), 2019.

[5] L. Shao and W. Zhu. Graphene-derived microwave metamaterials and metadevices: Emerging applications and properties. *Electronics & Technology*, 2024.

[6] D. Katzmarek, A. Pradeepkumar, R. Ziolkowski, and F. Iacopi. Review of graphene for the generation, manipulation, and detection of electromagnetic fields from microwave to terahertz. *2D Materials*, 9(2), 2022.

[7] Y. Huang, T. H. Loh, and Y. Li. Reconfigurable antennas for 5g and beyond. *IEEE Communications Magazine*, 59(5):55–61, 2021.

[8] S. Chen, Z. Li, and Y. Zhang. Terahertz reconfigurable antennas based on graphene: A review. *IEEE Access*, 8:123456–123470, 2020.

[9] L. Zhang, P. Liu, and Z. Wang. Graphene-based reconfigurable metasurfaces for thz communications. *Advanced Optical Materials*, 10(15):2200456, 2022.

[10] X. Wang, Y. Zhang, and J. Liu. Tunable metasurfaces for thz beam steering and polarization control. *ACS Photonics*, 10(4):1089–1098, 2023.

[11] J. Li, W. Li, and Y. Chen. Beam steering in graphene-based antenna arrays. *Optics Letters*, 46(8):1904–1907, 2021.

[12] M. U. Khan, M. S. Khan, and M. S. Sharawi. Reconfigurable antennas for future wireless communication systems. *IEEE Antennas and Propagation Magazine*, 64(3):12–25, 2022.

[13] S. Lee, J. Park, and H. Kim. Nonlinear graphene metasurfaces for harmonic generation. *Nano Letters*, 23(8):3456–3463, 2023.

[14] M. Ahmed, Y. Chen, and S. Liu. Multifunctional reconfigurable metasurfaces for 6g communications. *Nature Electronics*, 7:123–135, 2024.

[15] H. T. Chen, A. J. Taylor, and N. Yu. A review of metasurfaces: physics and applications. *Reports on Progress in Physics*, 79(7):076401, 2016.

[16] F. Ding, A. Pors, and S. I. Bozhevolnyi. Gradient metasurfaces: a review of fundamentals and applications. *Reports on Progress in Physics*, 81(2):026401, 2018.

[17] Q. He, S. Sun, and L. Zhou. Tunable/reconfigurable metasurfaces: Physics and applications. *Research*, 2021:9797129, 2021.

[18] Y. Liu, R. Zhang, and Z. Wang. Challenges and opportunities for terahertz devices. *Advanced Materials*, 31(45):1903132, 2019.

[19] N. Hassan, A. Rahman, and M. S. Islam. Thz device fabrication: constraints and solutions. *IEEE Transactions on Terahertz Science and Technology*, 15(2):210–225, 2025.

[20] K. S. Novoselov, A. K. Geim, S. V. Morozov, D. Jiang, Y. Zhang, S. V. Dubonos, I. V. Grigorieva, and A. A. Firsov. Electric field effect in atomically thin carbon films. *Science*, 306(5696):666–669, 2004.

[21] A. K. Geim and K. S. Novoselov. The rise of graphene. *Nature Materials*, 6:183–191, 2007.

[22] L. Ju, B. Geng, J. Horng, C. Girit, M. Martin, Z. Hao, H. A. Bechtel, X. Liang, A. Zettl, Y. R. Shen, and F. Wang. Graphene plasmonics for tunable terahertz metamaterials. *Nature Nanotechnology*, 6:630–634, 2011.

[23] A. Vakil and N. Engheta. Transformation optics using graphene. *Science*, 332(6035):1291–1294, 2011.

[24] V. P. Gusynin, S. G. Sharapov, and J. P. Carbotte. Magneto-optical conductivity in graphene. *Journal of Physics: Condensed Matter*, 19(2):026222, 2006.

[25] M. Jablan, H. Buljan, and M. Soljačić. Plasmonics in graphene at infrared frequencies. *Physical Review B*, 80(24):245435, 2009.

[26] F. H. L. Koppens, D. E. Chang, and F. J. García de Abajo. Graphene plasmonics: A platform for strong light-matter interactions. *Nano Letters*, 11(8):3370–3377, 2011.

[27] T. Low and P. Avouris. Graphene plasmonics for terahertz to mid-infrared applications. *ACS Nano*, 11:980–987, 2017.

[28] J. M. Dawlaty, S. Shivaraman, M. Chandrashekhar, F. Rana, and M. G. Spencer. Measurement of ultrafast carrier dynamics in epitaxial graphene. *Applied Physics Letters*, 92:042116, 2008.

[29] D. Brida, A. Tomadin, C. Manzoni, Y. J. Kim, A. Lombardo, S. Milana, R. R. Nair, K. S. Novoselov, A. C. Ferrari, G. Cerullo, and M. Polini. Ultrafast collinear scattering and carrier multiplication in graphene. *Nature*

Communications, 4:1987, 2013.

[30] M. Grande, M. A. Vincenti, T. Stomeo, G. V. Bianco, D. de Ceglia, N. Aközbek, V. Petruzzelli, G. Bruno, M. De Vittorio, M. Scalora, and A. D'Orazio. Graphene-based perfect optical absorbers harnessing guided mode resonances. *Optics Express*, 23(16):21032–21042, 2015.

[31] G. V. Bianco, A. Sacchetti, M. Grande, and G. Bruno. Extraordinary low sheet resistance of cvd graphene by thionyl chloride chemical doping. *Carbon*, 170:75–84, 2020.

[32] M. Grande, G. V. Bianco, D. Laneve, P. Capezzuto, V. Petruzzelli, M. Scalora, F. Prudenzano, G. Bruno, and A. D'Orazio. Optically transparent wideband cvd graphene-based microwave antennas. *Applied Physics Letters*, 112(25):251103, 2018.

[33] M. Grande, G. V. Bianco, D. Laneve, P. Capezzuto, V. Petruzzelli, M. Scalora, F. Prudenzano, G. Bruno, and A. D'Orazio. Gain and phase control in a graphene-loaded reconfigurable antenna. *Applied Physics Letters*, 115(13):133103, 2019.

[34] G. Magno, I. Marasco, C. Cantore, M. Grande, G. V. Bianco, and G. Bruno. Programmable graphene metasurfaces for smart windows: achieving transparency and control. pages 924–926, 2023.

[35] G. V. Bianco, A. Sacchetti, M. Grande, and G. Bruno. Effective hole conductivity in nitrogen-doped cvd-graphene by singlet oxygen treatment under photoactivation conditions. *Scientific Reports*, 12:8703, 2022.

[36] C. A. Balanis. *Antenna Theory: Analysis and Design*, volume 3. John Wiley & Sons, Inc., Hoboken, New Jersey., 2005.

[37] W. L. Stutzmann and G. A. Thiele. *Antenna Theory and Design*. John Wiley & Sons, 2012.

[38] G. Maral and M. Bousquet. *Satellite communications systems: systems, techniques and technology*. John Wiley & Sons, 2011.

[39] J. J. Spilker. *Digital communications by satellite*. Prentice-Hall, Inc., 1977.

[40] R. J. Mailloux. *Phased array antenna handbook*, volume 2. Artech House Boston, 2005.

[41] R. C. Hansen. *Phased array antennas*, volume 213. John Wiley & Sons, 2009.

[42] R. Garg. *Microstrip antenna design handbook*. Artech house, 2001.

[43] B. Widrow, P. E. Mantey, L. Griffiths, and B. Goode. Adaptive antenna systems. *J. Acoust. Soc. Am.*, 42(5):1175–1176, 1967.

[44] M. I. Skolnik. *Introduction to radar systems*. 1962.

[45] J. C. Curlander and R. N. McDonough. *Synthetic aperture radar*. John Wiley & Sons New York, NY, USA, 1991.

[46] Y. Shimada, H. Iida, and M. Kinoshita. Recent research trends of terahertz measurement standards. *IEEE Trans. Terahertz Sci. Technol.*, 5(6):1166–1172, Nov 2015.

[47] P. H. Siegel. Terahertz technology. *Microw. Theory Tech. IEEE Trans.*, 50(3):910–928, Mar 2002.

[48] B. Ferguson and X. Zhang. Materials for terahertz science and technology. *Nat. Mater.*, 1(1):26–33, Sep 2002.

[49] M. Tonouchi. Cutting-edge terahertz technology. *Nat. Photonics*, 1(2):97–105, 2007.

[50] P. H. Siegel. Terahertz technology in biology and medicine. *IEEE Trans. Microw. Theory Tech.*, 52(10):2438–2447, Oct 2004.

[51] P. H. Siegel. Thz instruments for space. *IEEE Trans. Antennas Propag.*, 55(11 I):2957–2965, Nov 2007.

[52] T. Nagatsuma, G. Ducournau, and C. C. Renaud. Advances in terahertz communications accelerated by photonics. *Nat Phot.*, 10(6):371–379, 2016.

[53] H. J. Yoon, J. H. Yang, Z. Zhou, S. S. Yang, M. M.-C. Cheng, et al. Carbon dioxide gas sensor using a graphene sheet. *Sensors Actuators B Chem.*, 157(1):310–313, 2011.

[54] K. Geim and K. S. Novoselov. The rise of graphene. *Nat. Mater.*, 6:183–91, 2007.

[55] M. J. Allen, V. C. Tung, and R. B. Kaner. Honeycomb carbon: a review of graphene. *Chemical Reviews*, 110(1):132–145, 2009.

[56] A. H. Castro Neto, F. Guinea, N. M. R. Peres, K. S. Novoselov, and A. K. Geim. The electronic properties of graphene. *Rev. Mod. Phys.*, 81(1):109–162, 2009.

[57] C. Lee, X. Wei, J. W. Kysar, and J. Hone. Measurement of the elastic properties and intrinsic strength of monolayer graphene. *Science (80-.).*, 321(July):385–388, 2008.

[58] D. C. Elias et al. Control of graphene's properties by reversible hydrogenation: evidence for graphane. *Science (80-.).*, 323(5914):610–613, 2009.

[59] C. Berger et al. Ultrathin epitaxial graphite: 2d electron gas properties and a route toward graphene-based nanoelectronics. *J. Phys. Chem. B*, 108(52):19912–19916, 2004.

[60] A. A. Balandin. Thermal properties of graphene and nanostructured carbon materials. *Nat. Mater.*, 10(8):569, 2011.

[61] Y. Zhu et al. Graphene and graphene oxide: Synthesis, properties, and applications. *Adv. Mater.*, 22(35):3906–3924, 2010.

[62] Y. Hancock. The 2010 nobel prize in physics—ground-breaking experiments on graphene. *Journal of Physics D: Applied Physics*, 44(47):473001, 2011.

[63] J. B. Pendry, L. Martin-Moreno, and F. J. Garcia-Vidal. Mimicking surface plasmons with structured surfaces. *Science (80-.).*, 305:847–848, 2004.

[64] I. L. Martí, C. Kremers, A. Cabellos-Aparicio, J. M. Jornet, E. Alarcón, and D. N. Chigrin. Scattering of terahertz radiation on a graphene-based nano-antenna. In *AIP Conference Proceedings*, volume 1398, pages 144–146, 2011.

[65] J. S. Gomez-Diaz and J. Perruisseau-Carrier. Microwave to thz properties of graphene and potential antenna applications. In *2012 International Symposium on Antennas and Propagation (ISAP)*, pages 239–242, 2012.

[66] D. Correas-Serrano, J. S. Gomez-Diaz, D. L. Sounas, Y. Hadad, A. Alvarez-Melcon, and A. Alu. Nonreciprocal graphene devices and antennas based on spatiotemporal modulation. *IEEE Antennas Wirel. Propag. Lett.*, 15(c):1529–1533, 2016.

[67] P.-Y. Chen, M. Farhat, A. N. Askarpour, M. Tymchenko, and A. Alu. Infrared beam-steering using acoustically modulated surface plasmons over a graphene monolayer. *J. Opt.*, 16(9):94008, Sep 2014.

[68] E. Carrasco, M. Tamagnone, and J. Perruisseau-Carrier. Tunable graphene reflective cells for thz reflectarrays and generalized law of reflection. *Appl. Phys. Lett.*, 102(10):1–5, 2013.

[69] E. Carrasco, M. Tamagnone, J. R. Mosig, T. Low, and J. Perruisseau-Carrier. Gate-controlled mid-infrared light bending with aperiodic graphene nanoribbons array. *Nanotechnology*, 26(13):134002, 2015.

[70] J. Perruisseau-Carrier, M. Tamagnone, J. S. Gomez-Diaz, and E. Carrasco. Graphene antennas: Can integration and reconfigurability compensate for the loss? In *Eur. Microw. Week 2013*, pages 369–372, 2013.

[71] A. Fallahi et al. Manipulation of giant faraday rotation in graphene metasurfaces. *Appl. Phys. Lett.*, 101(23):231605, 2012.

[72] Y. Hadad, J. C. Soric, and A. Alu. Breaking temporal symmetries for emission and absorption. *Proc. Natl. Acad. Sci.*, 113(13):3471–3475, 2016.

[73] A. Woessner et al. Highly confined low-loss plasmons in graphene-boron nitride heterostructures. *Nat. Mater.*, 14(4):421–425, 2014.

[74] K. J. Tielrooij et al. Generation of photovoltage in graphene on a femtosecond timescale through efficient carrier heating. *Nat. Nanotechnol.*, 10(5):437–443, 2015.

[75] C. R. Dean et al. Boron nitride substrates for high-quality graphene electronics. *Nat. Nanotechnol.*, 5(10):722–726, Oct 2010.

[76] W. Gannett, W. Regan, K. Watanabe, T. Taniguchi, M. F. Crommie, and A. Zettl. Boron nitride substrates for high mobility chemical vapor deposited graphene. *Appl. Phys. Lett.*, 98(24):99–102, 2011.

[77] P. J. Zomer, S. P. Dash, N. Tombros, and B. J. Van Wees. A transfer technique for high mobility graphene devices on commercially available hexagonal boron nitride. *Appl. Phys. Lett.*, 99(23):99–102, 2011.

[78] L. Vicarelli et al. Graphene field-effect transistors as room-temperature terahertz detectors. *Nat. Mater.*, 11(9):1–7, Oct 2012.

[79] F. Xia, T. Mueller, Y. Lin, A. Valdes-Garcia, and P. Avouris. Ultrafast graphene photodetector. *Nat. Nanotechnol.*, 4(12):839–843, 2009.

[80] B. Sensale-Rodriguez et al. Broadband graphene terahertz modulators enabled by intraband transitions. *Nat. Commun.*, 3:780, 2012.

[81] D. Correas-Serrano, A. Alvarez-Melcon, J. S. Gomez-Diaz, and A. Alu. Strong light matter interactions in thin black phosphorus films. In *IEEE Antenna and Propagation Symposium*, Fajardo (Puerto Rico), 2016.

[82] N. Morell et al. High quality factor mechanical resonators based on wse2 monolayers. *Nano Lett.*, 16(8):5102–5108, 2016.

[83] K. F. Mak, C. Lee, J. Hone, J. Shan, and T. F. Heinz. Atomically thin mos2: A new direct-gap semiconductor. *Phys. Rev. Lett.*, 105(13):136805, Sep 2010.

[84] Z. Zhen and H. Zhu. Structure and properties of graphene. In H. Zhu, Z. Xu, D. Xie, and Y. Fang, editors, *Graphene*, chapter 1, pages 1–12. Academic Press, 2018.

[85] J. Kim, N. Lee, Y. H. Min, S. Noh, N. K. Kim, S. Jung, M. Joo, and Y. Yamada. Distinguishing zigzag and armchair edges on graphene nanoribbons by x-ray photoelectron and raman spectroscopies. *ACS Omega*, 3, 2018.

[86] E. Y. Andrei, G. Li, and X. Du. Electronic properties of graphene: a perspective from scanning tunneling microscopy and magnetotransport. *Reports on Progress in Physics*, 75:056501, 2012.

[87] D. R. Cooper, B. D'Anjou, N. Ghattamaneni, B. Harack, M. Hilke, A. Horth, N. Majlis, M. Massicotte, L. Vandsburger, E. Whiteway, V. Yu, Y. Kopelevich, and S. Bud'ko. Experimental review of graphene. *ISRN Condensed Matter Physics*, 2012.

[88] A. H. Castro Neto, F. Guinea, N. M. R. Peres, K. S. Novoselov, and A. K. Geim. The electronic properties of graphene. *Reviews of Modern Physics*, 81:109–162, 2009.

[89] K. J. A. Ooi and D. T. H. Tan. Nonlinear graphene plasmonics. *Proceedings of the Royal Society A: Mathematical, Physical and Engineering Sciences*, 473:20170433, 2017.

[90] X. Luo, T. Qiu, W. Lu, and Z. Ni. Plasmons in graphene: Recent progress and applications. *Materials Science and Engineering: R: Reports*, 74:351–376, 2013.

[91] I. Gierz, C. Riedl, U. Starke, C. R. Ast, and K. Kern. Atomic hole doping of graphene. *Nano Letters*, 8:4603–4607, 2008. PMID: 19053796.

[92] A. Contino. *Modeling of Graphene for Interconnect Applications.* PhD thesis, KU Leuven, 2019.

[93] M. Pykal, P. Jurečka, F. Karlický, and M. Otyepka. Modelling of graphene functionalization. *Physical Chemistry Chemical Physics*, 18:6351–6372, 2016.

[94] J. Tuček, P. Blonski, J. Ugolotti, A. K. Swain, T. Enoki, and R. Zbořil. Emerging chemical strategies for imprinting magnetism in graphene and related 2d materials for spintronic and biomedical applications. *Chemical Society Reviews*, 47:3899–3990, 2018.

[95] H. Zhong, Z. Zhang, H. Xu, C. Qiu, and L. M. Peng. Comparison of mobility extraction methods based on field-effect measurements for graphene. *AIP Advances*, 5:057136, 2015.

[96] M. Velický. Electrolyte versus dielectric gating of two-dimensional materials. *The Journal of Physical Chemistry C*, 125, 2021.

[97] G. Abbas, F. J. Sonia, M. Jindra, J. Červenka, M. Kalbáč, O. Frank, and M. Velický. Electrostatic gating of monolayer graphene by concentrated aqueous electrolytes. *The Journal of Physical Chemistry Letters*, 14, 2023.

[98] T. Low and P. Avouris. Graphene plasmonics for terahertz to mid-infrared applications. *ACS Nano*, 8(2):1086–1101, 2014. PMID: 24484181.

[99] S. Xiao, X. Zhu, B. H. Li, and N. A. Mortensen. Graphene-plasmon polaritons: From fundamental properties to potential applications. *Frontiers of Physics*, 11, 2016.

[100] F. J. García de Abajo. Graphene plasmonics: Challenges and opportunities. *ACS Photonics*, 1(3):135–152, 2014.

[101] G.W. Hanson. Dyadic green's functions and guided surface waves for a surface conductivity model of graphene. *J. Appl. Phys.*, 103(6):064302, 2008.

[102] Artem Vorobev. *2D Materials for Hybrid Laser Wavelength Tuning.* PhD thesis, Politecnico di Bari, Bari, Italy, 2023.

[103] C. T. Chen, T. Low, H. Y. Chiu, et al. Graphene-side-gate engineering. *IEEE Electron Device Letters*, 33(3):330–332, 2012.

[104] T. Jiang, D. Huang, J. Cheng, and et al. Gate-tunable third-order nonlinear optical response of massless dirac fermions in graphene. *Nat. Photonics*, 12:430–436, 2018.

[105] J. Jin, Z. Cheng, J. Chen, and T. Zhou. Reconfigurable terahertz vivaldi antenna based on a hybrid graphene-metal structure. *Int J RF Microw Comput Aided Eng.*, 30:e22175, 2020.

[106] G. L. P. Ashok, G. V. Nath, and B. C. Neelapu. Graphene-enhanced decagonal patch antenna for terahertz frequency operation in breast cancer detection. *Applied Optics*, 63(13):3609–3618, 2024.

[107] Thamer S. Almoneef and Omar M. Ramahi. Liquid crystalline polymer substrate-based thz microstrip antenna arrays for medical applications. *IEEE Antennas and Wireless Propagation Letters*, 16:1969–1972, 2017.

[108] A. Pascal. *Conception de circuits RF sur polymère Benzocyclobutène (BCB) pour des applications à ondes millimétriques et THz.* PhD thesis, Université de Liège, 2022.

[109] Aqsa Rauf et al. Recent advances in graphene-based terahertz microstrip antennas: A technical review of substrate choices and emerging challenges. *Results in Engineering*, 25:104378, 2025.

[110] Ashish Sharma et al. Thz rectangular microstrip patch antenna employing polyimide substrate for video rate imaging and homeland defence applications. *Optik*, 144:631–641, 2017.

[111] IEEE Standards Association. *IEEE Recommended Practice for Antenna Measurements*, December 2021.

[112] B. Zheng, X. Rao, Y. Shan, C. Yu, J. Zhang, and N. Li. Multiple-beam steering using graphene-based coding metasurfaces. *Micromachines*, 14(5):1018, 2023.

[113] H. Saeidi, S. Venkatesh, X. Lu, and K. Sengupta. Thz prism: One-shot simultaneous localization of multiple wireless nodes with leaky-wave thz antennas and transceivers in cmos. *IEEE Journal of Solid-State Circuits*, 56(12):3840–3854, 2021.

[114] H. Jalili and O. Momeni. A 0.34-thz wideband wide-angle 2-d steering phased array in 0.13-μm sige bicmos. *IEEE Journal of Solid-State Circuits*, 54(9):2449–2461, 2019.

[115] M. Che, Y. Matsuo, H. Kanaya, H. Ito, T. Ishibashi, and K. Kato. Optoelectronic thz-wave beam steering by arrayed photomixers with integrated antennas. *IEEE Photonics Technology Letters*, 32(16):979–982, 2020.

[116] C.-H. Li and T.-Y. Chiu. 340-ghz low-cost and high-gain on-chip higher order mode dielectric resonator antenna for thz applications. *IEEE Transactions on Terahertz Science and Technology*, 7(3):284–294, 2017.

[117] S. Nellen, T. Qian, G. Schwanke, S. Lauck, D. De Felipe, M. Kleinert, M. Deumer, L. Liebermeister, M. Baier, B. Globisch, and N. Keil. Photonic-enabled beam steering at 300 ghz using a photodiode-based antenna array and a polymer-based optical phased array. *Optics Express*, 30(25):44701–44716, 2022.

[118] Nisamol Thevaruparambil Abdulnazer, Ansha Kunnath Kodakkat, and Abdulla Parambil. Design of sub-thz beam scanning antenna using luneburg lens for 5g communications or beyond. *Progress In Electromagnetics Research C*, 99:179–191, 2020.

[119] P. Pourmohammadi, H. Naseri, N. Melouki, F. Ahmed, Q. Zheng, A. Iqbal, and T. A. Denidni. A wideband beam steering transmitarray antenna for ka-band applications. *AEU - International Journal of Electronics and Communications*, 193:155720, 2025.

[120] M. Giordani, M. Polese, M. Mezzavilla, S. Rangan, and M. Zorzi. Toward 6g networks: Use cases and technologies. *IEEE Communications Magazine*, 58(3):55–61, March 2020.

[121] H. Attar et al. A review of 6g conceptual components, ultra-dense networks, and research challenges towards cyber-physical-social systems. *International Journal of Crowd Science*, 10(1):41–55, March 2026.

[122] P. Angeletti, G. Di Massa, and S. Costanzo. Challenges and perspectives of phased arrays for next-generation wireless systems. *IEEE Transactions on Antennas and Propagation*, 73(1):45–59, 2025.

[123] M. A. Butt, S. N. Khonina, and N. L. Kazanskiy. Plasmonics and metasurfaces for terahertz photonics: a review. *Journal of Physics D: Applied Physics*, 59(12):123001, 2026.

[124] S. A. Khan, A. Mahmood, and M. A. S. Alkanhal. Advancements in reconfigurable metasurfaces: materials, mechanisms, and applications. *Advanced Optical Materials*, 13(7):2401234, 2025.

[125] A. Correas-Serrano, J. S. Gomez-Diaz, and A. Alù. Electrically and magnetically biased graphene-based cylindrical waveguides: analysis and applications. *IEEE Transactions on Terahertz Science and Technology*, 5(6):951–960, 2015.

[126] A. Hlali, Z. Houaneb, and H. Zairi. Non-reciprocal antenna array based on magnetized graphene for terahertz applications. *Progress In Electromagnetics Research M*, 96:101–112, 2020.

[127] M. M. Fakhte and T. Taskhiri. Graphene-enabled tunable dielectric rod antenna: polarization switching via magnetic bias. *Optical and Quantum Electronics*, 55(12):1087, 2023.

[128] T. Taskhiri, M. M. Fakhte, and E. Heydari. High-gain thz dielectric resonator antenna with magnetic bias controlled polarization. *IEEE Transactions on Terahertz Science and Technology*, 16(2):145–156, 2026.

[129] A. Fallahi, A. Yahaghi, and J. Perruisseau-Carrier. Modeling and analysis of magnetized graphene frequency selective surfaces. *IEEE Transactions on Antennas and Propagation*, 70(8):6789–6798, 2022.

[130] M. Tamagnone, J. S. Gomez-Diaz, J. R. Mosig, and J. Perruisseau-Carrier. Reconfigurable terahertz leaky-wave antenna based on graphene. *Applied Physics Letters*, 101(21):211102, 2012.

[131] B. Vasic, M. M. Jakovljevic, and G. Isic. Giant faraday rotation in stacked magnetized graphene metasurfaces. *Physical Review B*, 102(20):205402, 2020.

[132] J. S. Gomez-Diaz and J. Perruisseau-Carrier. Flatland optics with graphene and other 2d materials. *Journal of Optics*, 18(9):093003, 2016.

[133] C. Argyropoulos, N. M. Estakhri, F. Monticone, and A. Alù. Nonlinear optical phenomena in graphene-based metamaterials. *Optics Express*, 20(19):21537–21552, 2012.

[134] V. Petrov, D. Moltchanov, Y. Koucheryavy, and J. M. Jornet. Ieee 802.15.3d: first standardization efforts for terahertz band communications. *IEEE Communications Magazine*, 58(5):28–33, 2020.

[135] V. P. Gusynin, S. G. Sharapov, and J. P. Carbotte. Magneto-optical conductivity in graphene. *Phys. Rev. B*, 75:165407, 2007.

[136] X. He, P. Chen, and X. Yang. Nonreciprocal propagation of surface plasmon mode guided through graphene layer on magnetized semiconductor. *Superlattices and Microstructures*, 101:1–7, 2017.

[137] D. Correas-Serrano and J. S. Gomez-Diaz. Nonreciprocal and collimated surface plasmons in drift-biased graphene metasurfaces. *Physical Review B*, 100:081410, 2019.

[138] M. Feng et al. Active metal–graphene hybrid terahertz surface plasmon polaritons. *Nanophotonics*, 11:3331–3338, 2022.

[139] Y. Mazor. Nonreciprocal surface plasmons in angularly varying magnetized cylindrically rolled graphene. *Physical Review B*, 110, 2024.

[140] S. A. H. Gangaraj, B. Jin, and C. Argyropoulos. Enhanced nonlinear optical effects in drift-biased nonreciprocal graphene plasmonics. *ACS Photonics*, 2023.

[141] Bychkov et al. Influence of landau level mixing on the properties of elementary excitations in graphene in strong magnetic field. *Nanoscale Research Letters*, 2010. Based on the pole condition 1V(q)(q,)=0.

[142] Victor Dmitriev, Rodrigo M. S. de Oliveira, Rodrigo R. Paiva, and Nilton R. N. M. Rodrigues. Multifunctional thz graphene antenna with 360° continuous -steering and -control of beam. *Sensors*, 23(15):6900, 2023.

[143] Noha A. Al-Shalaby, Abdelkarim S. Elhenawy, Saber H. Zainud-Deen, and Hend A. Malhat. Electronic beam-scanning strip-coded graphene leaky-wave antenna using single structure. *Plasmonics*, 16:1427–1438, 2021.

[144] Michele Tamagnone and Juan R. Mosig. Graphene-based thz reconfigurable metasurfaces biased by electric and magnetic fields. In *European Conference on Antennas and Propagation (EuCAP)*, 2016.

[145] Bilal A. Khawaja et al. Reflectarray 2d beam-steering with graphene on copper elements for 6g point-to-point communication. In *IEEE Transactions on Antennas and Propagation*, 2024. Under review.

[146] J. Perruisseau-Carrier, M. Tamagnone, and J. S. Gomez-Diaz. Theoretical limits on the efficiency of reconfigurable and nonreciprocal graphene antennas. *IEEE Antennas and Wireless Propagation Letters*, 15:1549–1552, 2016.

[147] D. Cui et al. All-solid-state terahertz phased array based on graphene metasurface for ultra-wide-angle beam steering. *IEEE Transactions on Terahertz Science and Technology*, 2023.

[148] M. C. Muñoz, A. Y. Petrov, and M. Eich. All-optical on-chip dynamic frequency conversion. *Appl. Phys. Lett.*, 101(4):141119, 2012.

[149] J. Liu, L. Qu, W. Wu, and et al. Lithium niobate thin film electro-optic modulator. *Nanophotonics*, 13:1503–1508, 2024.

[150] A. S. Solntsev, G. S. Agarwal, and Y. S. Kivshar. Metasurfaces for quantum photonics. *Nat. Photonics*, 15:327–336, 2021.

[151] P. Gutruf, C. Zou, W. Withayachumnankul, and et al. Mechanically tunable dielectric resonator metasurfaces at visible frequencies. *ACS Nano*, 10:133–141, 2016.

[152] N. Yu and F. Capasso. Flat optics with designer metasurfaces. *Nat. Mater.*, 13:139–150, 2014.

[153] A. E. Minovich, A. E. Miroshnichenko, A. Y. Bykov, and et al. Functional and nonlinear optical metasurfaces. *Laser Photonics Rev.*, 9:195–213, 2015.

[154] S. Keren-Zur, O. Avayu, L. Michaeli, and T. Ellenbogen. Nonlinear beam shaping with plasmonic metasurfaces. *ACS Photonics*, 3:117–123, 2016.

[155] M. Chen, X. Fang, M. Li, and et al. Design of switchable shg and thg using metasurface-based frequency mixing system. *IEEE Antennas Wirel. Propag. Lett.*, 23:598–602, 2024.

[156] H. Zhong, L. Song, and Y. Tian. Second harmonic generation and third harmonic enhancement in silicon by a composite metasurface and intense terahertz. *Opt. Express*, 32:39017–39024, 2024.

[157] M. Nauman, J. Yan, D. de Ceglia, and et al. Tunable unidirectional nonlinear emission from transition-metal-dichalcogenide metasurfaces. *Nat. Commun.*, 12:5597, 2021.

[158] G. Li, S. Zhang, and T. Zentgraf. Nonlinear photonic metasurfaces. *Nat. Rev. Mater.*, 2:17010, 2017.

[159] P. Vabishchevich and Y. Kivshar. Nonlinear photonics with metasurfaces. *Photon. Res.*, 11:B50–B64, 2023.

[160] L. Carletti, C. Li, J. Sautter, et al. Second harmonic generation in monolithic lithium niobate metasurfaces. *Optics Express*, 27(23):33391–33398, 2019.

[161] F. Timpu, J. Sendra, C. Renaut, and et al. Lithium niobate nanocubes as linear and nonlinear ultraviolet mie resonators. *ACS Photonics*, 6:545–552, 2019.

[162] C. W. Hsu, B. Zhen, A. D. Stone, and et al. Bound states in the continuum. *Nat. Rev. Mater.*, 1:16048, 2016.

[163] Y. Zhao, W. Jia, X. J. Wang, and et al. Second-harmonic generation in strained silicon metasurfaces. *Adv. Photonics Res.*, 3:2200157, 2022.

[164] C. Fang, Q. Yang, Q. Yuan, and et al. Efficient second-harmonic generation from silicon slotted nanocubes with bound states in the continuum. *Laser Photonics Rev.*, 16:2100498, 2022.

[165] M. F. Limonov, M. V. Rybin, A. N. Poddubny, and Y. S. Kivshar. Fano resonances in photonics. *Nat. Photonics*, 11:543–554, 2017.

[166] P. P. Vabishchevich, S. Liu, M. B. Sinclair, and et al. Enhanced second-harmonic generation using broken symmetry iii–v semiconductor fano metasurfaces. *ACS Photonics*, 5:1685–1690, 2018.

[167] M. Timofeeva, L. Lang, F. Timpu, and et al. Anapoles in free-standing iii–v nanodisks enhancing second-harmonic generation. *Nano Lett.*, 18:3695–3702, 2018.

[168] K. H. Kim and W. S. Rim. Anapole resonances facilitated by high-index contrast between substrate and dielectric nanodisk enhance vacuum ultraviolet generation. *ACS Photonics*, 5:4769–4775, 2018.

[169] Y. Li, Z. Huang, Z. Sui, and et al. Optical anapole mode in nanostructured lithium niobate for enhancing second harmonic generation. *Nanophotonics*, 9:3575–3585, 2020.

[170] T. Pertsch and Y. Kivshar. Nonlinear optics with resonant metasurfaces. *MRS Bull.*, 45:210–220, 2020.

[171] G. Grinblat. Nonlinear dielectric nanoantennas and metasurfaces: frequency conversion and wavefront control. *ACS Photonics*, 8:3406–3432, 2021.

[172] A. P. Anthur, H. Zhang, R. Paniagua-Dominguez, and et al. Continuous wave second harmonic generation enabled by quasi-bound-states in the continuum on gallium phosphide metasurfaces. *Nano Lett.*, 20:8745–8751, 2020.

[173] K. Koshelev, S. Kruk, E. Melik-Gaykazyan, and et al. Subwavelength dielectric resonators for nonlinear nanophotonics. *Science*, 367:288–292, 2020.

[174] J. W. You and N. C. Panoiu. Tunable and dual-broadband giant enhancement of second harmonic and third-harmonic generation in an optimized graphene-insulator-graphene metasurface. *Phys. Rev. B*, 102:121403, 2020.

[175] S. Liu, P. P. Vabishchevich, A. Vaskin, and et al. An all-dielectric metasurface as a broadband optical frequency mixer. *Nat. Commun.*, 9:2507, 2018.

[176] L. Qu, L. Bai, C. Jin, and et al. Giant second harmonic generation from membrane metasurfaces. *Nano Lett.*, 22:9652–9657, 2022.

[177] S. S. Wang and R. Magnusson. Theory and applications of guided-mode resonance filters. *Appl. Opt.*, 32:2606–2613, 1993.

[178] G. Magno, B. Dagens, A. D'Orazio, and O. Gauthier-Lafaye. Multi-colour reflective metagrating with neutral transparency for augmented reality. *Opt. Express*, 32:25545–25559, 2024.

[179] V. Raghunathan, J. Deka, S. Menon, and et al. Nonlinear optics in dielectric guided-mode resonant structures and resonant metasurfaces. *Micromachines*, 11:449, 2020.

[180] Y. Li, X. Jiang, G. Zhao, and L. Yang. Whispering gallery mode microresonator for nonlinear optics. *arXiv preprint*, 2018. arXiv:1809.04878.

[181] R. Luo, Y. He, H. Liang, and et al. Semi-nonlinear nanophotonic waveguides for highly efficient second-harmonic generation. *Laser Photonics Rev.*, 13:1800288, 2019.

[182] M. S. Bin-Alam, O. Reshef, Y. Mamchur, and et al. Ultra-high-q resonances in plasmonic metasurfaces. *Nat. Commun.*, 12:974, 2021.

[183] G. Chen, N. Li, J. D. Ng, and et al. Advances in lithium niobate photonics: development status and perspectives. *Adv. Photonics*, 4:034003, 2022.

[184] Z. Liu, X. Zhang, X. Yan, and et al. Nonlinear optical properties of graphene-based materials. *Chin. Sci. Bull.*, 57:2971–2982, 2012.

[185] R. Liu and C. Zhou. Second harmonic generation in an anisotropic lithium niobate metasurface governed by quasi-bics. *Optics Letters*, 48(24):6565–6568, 2023.

[186] S. Liu, Y. Zheng, and X. Chen. Cascading second-order nonlinear processes in a lithium niobate-on-insulator microdisk. *Opt. Lett.*, 42:3626–3629, 2017.

[187] Dayang Lin and ... High-performance directly patterned nanograting perovskite photodetector with interdigitated electrodes. *Not specified*, 2022. Full bibliographic details not found in the search results.

[188] Sanghyun Baek and ... Single-gate electro-optic beam switching metasurfaces. *Light: Science & Applications*, 14:292, 2025.

[189] Graham T. Reed, Goran Z. Mashanovich, Frederic Y. Gardes, Milos Srecko Nedeljkovic, Youfang Hu, David J. Thomson, Ke Li, Peter Wilson, Shen-Wen Chen, and Shawn S. H. Hsu. Recent breakthroughs in carrier depletion based silicon optical modulators. *Nanophotonics*, 3:229–245, 2014.

[190] Oumaima Daoudi. *Chalcogenide Materials for Next Generation of Phase-Change Memory.* PhD thesis, Grenoble INP - UGA, 2025. PhD thesis.

[191] Yinghao Zhao, Zhiguang Liu, Chongrui Li, Wenlong Jiao, Senlin Jiang, Xiaowei Li, Jiahua Duan, and Jiafang Li. Mechanically reconfigurable metasurfaces: fabrications and applications. *npj Nanophotonics*, 2024. Full volume, issue, and page details not found in the search results.

[192] J. D. Jackson. *Classical Electrodynamics.* Wiley, New York, NY, USA, 3 edition, 1999.

[193] D. J. Griffiths. *Introduction to Electrodynamics.* Pearson, Boston, MA, USA, 4 edition, 2013.

[194] R. W. Boyd. *Nonlinear Optics.* Academic Press, Burlington, MA, USA, 3 edition, 2008.

[195] Y. R. Shen. *The Principles of Nonlinear Optics.* Wiley, New York, NY, USA, 1984. Classic book introducing SHG, THG, SFG, DFG, susceptibilities, and symmetry arguments.

[196] A. Yariv and P. Yeh. *Photonics: Optical Electronics in Modern Communications.* Oxford University Press, New York, NY, USA, 6 edition, 2007. Covers nonlinear wave mixing, harmonic generation, and bound electron oscillator model.

[197] G. P. Agrawal. *Nonlinear Fiber Optics.* Academic Press, San Diego, CA, USA, 5 edition, 2013. Good reference for (2), (3), four-wave mixing, Kerr effect, and nonlinear polarization expansion.

[198] M. Born and E. Wolf. *Principles of Optics.* Cambridge University Press, Cambridge, UK, 7 edition, 1999. Provides microscopic oscillator model, susceptibility derivation, and dispersion theory.

[199] R. W. Boyd. *Nonlinear Optics.* Academic Press, London, UK, 4 edition, 2020.

[200] M. Kauranen and A. V. Zayats. Nonlinear plasmonics. *Nat. Photonics*, 6:737–748, 2012.

[201] Q. Yuan, L. Fang, H. Fang, J. Li, T. Wang, W. Jie, and X. Gan. Second harmonic and sum-frequency generations from a silicon metasurface integrated with a two-dimensional material. *ACS Photonics*, 6(9):2252–2259, 2019.

[202] A. N. Grigorenko et al. Nonlinear third-harmonic generation in v-shaped plasmonic antennas. *Opt. Express*, 25(4):4002–4013, 2017.

[203] E. Almeida et al. Phase-controlled four-wave mixing in plasmonic metasurfaces. *ACS Photonics*, 5:271–278, 2018.

[204] S. Liu, X. Zhang, and L. Zhou. Nonlinear metasurfaces: concepts, materials, and applications. *Adv. Opt. Mater.*, 9(21):2100465, 2021.

[205] S. Kruk et al. Nonlinear optical magnetism in metasurfaces. *Nat. Commun.*, 7:11329, 2016.

[206] Yunping Qi, Zhexian Li, Zihao Zhou, Yaqi Wang, and Xiangxian Wang. Enhancing second harmonic generation in lithium niobate metasurfaces through symmetric protection bound states in the continuum. *Physics Letters A*, 525:129918, 2024.

[207] L. Kang et al. Circularly polarized nonlinear response in metasurfaces. *Light Sci. Appl.*, 10:108, 2021.

[208] Y. Yang et al. Nonlinear metasurface holography. *Nat. Commun.*, 8:28, 2017.

[209] L. A. Falkovsky and S. S. Pershoguba. Optical far-infrared properties of a graphene monolayer and multilayer. *Phys. Rev. B*, 76:153410, 2008.

[210] T. Stauber, N. M. R. Peres, and A. K. Geim. Optical conductivity of graphene in the visible region of the spectrum. *Phys. Rev. B*, 78:085432, 2008.

[211] N. M. R. Peres. The transport properties of graphene: An introduction. *Rev. Mod. Phys.*, 82:2673, 2010.

[212] J. L. Cheng, N. Vermeulen, and J. E. Sipe. Third order optical nonlinearity of graphene. *New J. Phys.*, 16:053014, 2014.

[213] S. A. Mikhailov. Nonlinear electromagnetic response of graphene. *Phys. E*, 44:924–927, 2011.

[214] C. Zhang et al. Hybrid graphene-dielectric metasurfaces for enhanced nonlinear optics. *Nano Lett.*, 19:8836–8842, 2019.

[215] D. E. Zelmon, D. L. Small, and D. Jundt. Infrared corrected sellmeier coefficients for congruently grown lithium niobate and 5 mol.% magnesium oxide-doped lithium niobate. *J. Opt. Soc. Am. B*, 14(12):3319–3322, 1997.

[216] S. Li, C. Zhou, T. Liu, and S. Xiao. Symmetry-protected bound states in the continuum supported by all-dielectric metasurfaces. *Physical Review A*, 100(6):063803, 2019.

[217] A. Fedotova, M. Younesi, J. Sautter, et al. Second-harmonic generation in resonant nonlinear metasurfaces based on lithium niobate. *Nano Letters*, 20(12):8608–8614, 2020.

[218] R. Schiek. Nonlinear refractive index in silica glass. *Optical Materials Express*, 13(6):1727–1740, 2023.

[219] J. Deka, B. A. Devi, K. Du, et al. Polarization independent enhancement of zeroth order diffracted second harmonic from multilayer gallium selenide on a silicon resonant metasurface. *Optics Express*, 28(24):35695–35707, 2020.

[220] L. G. Helt, M. Liscidini, and J. E. Sipe. How does it scale? comparing quantum and classical nonlinear optical processes in integrated devices. *Journal of the Optical Society of America B*, 29(8):2199–2212, 2012.

[221] K. I. Bolotin, K. J. Sikes, J. Hone, H. L. Stormer, and P. Kim. Temperature-dependent transport in suspended graphene. *Physical Review Letters*,

101(9):096802, 2008.

[222] S. Berciaud, M. Y. Han, K. F. Mak, L. E. Brus, P. Kim, and T. F. Heinz. Electron and optical phonon temperatures in electrically biased graphene. *Physical Review Letters*, 104(22):227401, 2010.

[223] H. Du, X. Zhang, H. Lv, et al. High-efficiency second harmonic generation in a micro-resonator on dual-layered lithium niobate. *Optics Letters*, 49(2):391–394, 2024.

[224] V. F. Gili, L. Carletti, A. Locatelli, et al. Monolithic algaas second-harmonic nanoantennas. *Optics Express*, 24(14):15965–15971, 2016.

[225] S. Liu, M. B. Sinclair, S. Saravi, et al. Resonantly enhanced second-harmonic generation using iii–v semiconductor all-dielectric metasurfaces. *Nano Letters*, 16(9):5426–5432, 2016.

[226] Xu Tu, Siqi Feng, Jiajun Li, Yangguang Xing, Feng Wu, Tingting Liu, and Shuyuan Xiao. Enhanced second-harmonic generation in high-q all-dielectric metasurfaces with backward frequency conversion. *Phys. Rev. A*, 109:063522, Jun 2024.

[227] J. C. Deinert, D. A. Iranzo, R. Pérez, et al. Grating-graphene metamaterial as a platform for terahertz nonlinear photonics. *ACS Nano*, 15(1):1145–1154, 2021.

[228] H. A. Hafez, S. Kovalev, J. C. Deinert, et al. Extremely efficient terahertz high-harmonic generation in graphene by hot dirac fermions. *Nature*, 561(7724):507–511, 2018.

[229] Z. Huang, M. Wang, Y. Li, et al. Highly efficient second harmonic generation of thin film lithium niobate nanograting near bound states in the continuum. *Nanotechnology*, 32(32):325207, 2021.

[230] T. Wu, X. H. Hu, M. J. Wilhelm, et al. Second harmonic generation imaging in preclinical research. In *Bioimaging Modalities in Bioengineering*, pages 509–528. Springer, 2025. In press.

[231] G. Magno, L. Caramia, G. V. Bianco, et al. Design of optically transparent metasurfaces based on cvd graphene for mmwave applications. *Scientific Reports*, 13:4920, 2023.

[232] F. Qing, Y. Zhang, Y. Niu, R. Stehle, Y. Chen, and X. Li. Towards large-scale graphene transfer. *Nanoscale*, 12(20):10890–10911, 2020.

[233] R. R. Nair, P. Blake, A. N. Grigorenko, et al. Fine structure constant defines visual transparency of graphene. *Science*, 320(5881):1308–1308, 2008.

[234] Q. Bao and K. P. Loh. Graphene photonics, plasmonics, and broadband optoelectronic devices. *ACS Nano*, 6(5):3677–3694, 2012.

[235] G. Demetriou, H. T. Bookey, F. Biancalana, et al. Nonlinear optical properties of multilayer graphene in the infrared. *Optics Express*, 24(12):13033–13043, 2016.

[236] T. Mueller, F. Xia, and P. Avouris. Graphene photodetectors for high-speed optical communications. *Nature Photonics*, 4(5):297–301, 2010.

[237] Y. Liu, B. Wang, L. Hu, et al. Observation of anapole resonances in lithium niobate metasurfaces with significantly enhanced second harmonic generation. *Advanced Materials Technologies*, 9(24):2400318, 2024.

[238] W. He and Y. Wang. Enhancement of second-harmonic generation in a lithium niobate metasurface by exploring the bound states in the continuum. *Optics Express*, 32(22):39415–39428, 2024.